Testing General Relativity with Gravitational Waves from Compact Binaries

Nan Jiang
Changchun, Jilin, China
B.S. Physics, Jilin University, 2017

A Dissertation presented to the Graduate Faculty
of the University of Virginia in Candidacy for the degree of
Doctor of Philosophy

Department of Physics
University of Virginia
April 2023

Professor Kent Yagi
Research Advisor

Professor David Nichols

Professor Gia-Wei Chern

Professor Phil Arras
GSAS Representative

Abstract

Since the first detection of the gravitational wave (GW) event GW150914 by the LIGO and Virgo Collaborations in 2015, over 90 transients have been observed. In addition to the typical binary black hole (BBH) events demonstrated by GW150914, there are other types of events, namely binary neutron star mergers (e.g., GW170817) and neutron star-black hole binary events (e.g., GW200105, GW200115), which provide additional perspectives for the examination of gravitational theories. Furthermore, using X-rays, the Neutron Star Interior Composition Explorer (NICER) has enabled the measurement of the mass and radius of an isolated neutron star, which means that testing gravity in the strong field regime could now be applied to not only black hole dynamics but also to neutron stars and black hole-neutron star interactions. This thesis focuses on analyzing the profiles of neutron stars analytically and studying tests of gravity using GW events associated with neutron stars and black holes.

Before employing neutron stars to test General Relativity (GR), we study analytical properties of these astrophysical objects. Universal relations have been discovered that are insensitive to the equation of state (EoS) of neutron stars, and they have important applications for probing fundamental physics, such as nuclear and gravitational physics. However, there is a lack of analytic works on universal relations for realistic neutron stars, which hinders a better understanding of universality. In this thesis, we focus on the universal relations between the compactness (C), the moment of inertia (I), and the tidal deformability (related to the Love number), and derive analytic, approximate I-Love-C relations. In order to construct slowly-rotating/tidally-deformed neutron star solutions, we first derive an analytic model of the static and isolated neutron star interior. We introduce an improved analytic model based on the Tolman VII solution that includes an additional parameter to have a better match with density profiles obtained numerically. The improvement is by a factor of 2∼5 and this additional parameter can also be fitted in an EoS-insensitive way in terms of the stellar mass, radius, and central density. Using this improved analytic profile, we solve for the slowly-rotating and tidally deformed neutron star profile through perturbation theory. Our results mathematically demonstrate the $\mathcal{O}(10\%)$ EoS variation in the I-C and Love-C relations and the $\mathcal{O}(1\%)$ variation in the I-Love relation that have previously been found numerically.

Next, we explore the prospects of probing potential non-GR effects in the propagation of GWs emitted by binary neutron star (BNS) mergers. Previous tests of this kind relied on an electromagnetic (EM) counterpart to compare with the GW signals. However, we propose an alternative approach that uses BNS mergers without EM counterparts to investigate modified GW propagation through the tidal effects. This method measures the redshift with the tidal Love number, which is linked to the intrinsic masses of the neutron stars. By combining the redshifted mass measurement with the tidal information, we can break the degeneracy between the redshift and the intrinsic mass to extract the former. We consider multi-band observations using both ground-based and space-based interferometers over a 3-year observation period. Our results show that such multi-band observations with tidal information can more stringently constrain a parametric non-Einsteinian deviation in the luminosity distance (arising from modified friction in the GW evolution) compared to

relying solely on EM counterparts, by a factor of a few. We also map the constraint on the GW propagation parameter to bounds on parameters in various beyond-GR gravity theories.

In our next project, we investigate how neutron star-black hole (NSBH) GW events set a more stringent bound on a particular modified theory of gravity, Einstein-dilaton-Gauss-Bonnet (EdGB) gravity. We show that the leading order correction to the evolution of the GW phase, originating from the scalar dipole radiation, is inversely proportional to the fourth power of the total mass of the system. As a result, smaller total mass systems would give a more significant contribution to this correction. Moreover, the scalar dipole radiation scales with the square of the difference in the scalar charges for two bodies in a binary. Thus, (stellar-mass) NSBH binary systems are well-suited to impose further constraints on EdGB gravity. Our analysis yields a stronger bound on the EdGB parameter α_{GB} than that obtained by combining selected BBH systems from the GWTC-1 and GWTC-2 catalogs. Furthermore, we improve upon this analysis by including higher order corrections up to the second post-Newtonian order in phase evolution, and we find that there is roughly a 10% improvement on the bounds.

In the final chapter, we present our ongoing work on speeding up the parameter estimation for beyond-GR parameter inference for BBH signals using neural networks. Standard methods used to estimate their source parameters employ computationally expensive Bayesian inference approaches (e.g. the Bayesian inference performed in the project mentioned in the previous paragraph takes $\sim$ a day to finish). Here, we intend to use conditional variational autoencoder to perform the task, and we have succeeded in four-parameter estimation for BBH GW signals. The addition of

non-GR modification to the training samples remains in progress.

Acknowledgments

子路宿于石门。晨门曰：“奚自？”子路曰：“自孔氏。”曰:“是知其不可而为之者与？”

——《论语·宪问》

I took a handful of sand,

I dropped silently

a little further

and said quietly:

I am modifying the Sahara.

—— Jorge Luis Borges, the book "Atlas"

Fifteen years ago, my dad showed me a documentary called 《宇宙与人》(The Universe and Man). This documentary appeared obsolete even at that time, but it made an ever-lasting impact on me, as a kid from a small town. This was my first exposure to awe-inspiring phenomena like supernovae, white dwarfs, neutron stars and black holes. From that moment, a desire to pursue knowledge in physics and the universe took root and sprouted. Despite struggling with physics in high school, I still chose to study physics as my major in college. Luckily, I did not do too bad, and I gained the confidence to continue on this path of exploring the mysteries of physics. Reflecting on the past 10 years, I realize it has been a journey filled with determination and challenges, one that could not have been navigated without the help and support of others. Many people, like mentors, teachers, friends, and family, have contributed to my progress on this arduous path. My words fall short of truly encapsulating my appreciation, allow me to first extend a heartfelt "thank you" to all who have guided and supported me throughout this decade-long journey.

First and most foremost, I want to express my deepest gratitude to my research advisor at UVA, Prof. Kent Yagi, for his guidance, insights, and continuous support, without which I could not possibly have completed this thesis. There is an ancient Chinese saying that goes like, “经师易求，人师难得” , which means finding an instructor to teach you knowledge is easy, but having a mentor who could show you how to be a better person is rare. I am truly fortunate to have an advisor whom I can genuinely call a mentor.

I am deeply grateful to my esteemed collaborators, Dr. Zhenwei Lyu, Professor Leo Stein, Dr. Maria Okounkova, and Sheng Zhang, for generously sharing their valuable knowledge and insights, which have significantly contributed to the progression of my research. I would also like to extend my most sincere appreciation to the entire UVA gravity group for all those engaging group meetings and journal clubs. Specifically, I would like to acknowledge Professor David Nichols and Dr. Alex Grant for their vast theoretical knowledge and insights across almost all academic subjects mentioned in the research meetings, Professor Phil Arras for sharing his rich astronomical expertise and offering diverse perspectives, and Dr. Alex Saffer for his consistently exceptional presentations. I am also grateful to Zack, a truly kind and inspiring role model for any PhD student, to Shammi, Vincent, Sid, Brian, Arwa, and Ben for sharing their passion for research and enlightening discussions concerning both their own research and my work.

I would also like to thank the members of my defense committee, Prof. David Nichols, Prof. Phil Arras, and Prof. Gia-Wei Chern (in particular for his support in my machine learning project), for their support and provide suggestions on how to improve my research. I would also like to thank all of the physics department support staff for their for his kind and supporting help, especially Peter Cline, for his always being there for us graduate students.

I am grateful for the company of my friends and fellow graduate students in Charlottesville, and for their invaluable support in both my academic and personal life. Those time spent on different basketball courts across Charlottesville is a precious memory to cherish. I also want to give special thanks to Jingchen Zhang, a friend from my undergraduate years, who currently works on condensed matter theories at UMD. I might not be able to come to US for graduate education without his encouragement. I am also fortunate to encounter FromSoftware's Souls-borne games, Atlus' *Persona 5 Royal* and Rockstar's *Red Dead Redemption II*, which were more than mere forms of entertainment and accompanied me through a pretty tough time.

Furthermore, I appreciate the time I spent in Professor Allan Megill's and Professor Victor Luftig's history (origin of contemporary thoughts, and Marx) and literature (more specifically, *Ulysses* by James Joyce) classes at UVA, which greatly broadened my perspective beyond the scopes of scientific training.

Lastly, I must thank my parents, whose understanding and emotional support over the past ten years made it possible for me to pursue my "unrealistic" fervor for delving into the realm of physics and complete my Ph.D. study. They refrained from pushing me towards lucrative careers and, instead, wholeheartedly backed my idealistic decision to study physics. I am eternally grateful to them.

List of Abbreviations

GR	General relativity
LVC	LIGO and Virgo Collaboration
LIGO	Laser Interferometer Gravitational-Wave Observatory
KAGRA	Kamioka Gravitational Wave Detector
GW	Gravitational wave
BH	Black hole
NS	Neutron star
BBH	Binary black hole
BNS	Binary Neutron Star
NSBH	Neutron Star Black Hole
LMXB	Low-mass X-ray binary
GWTC	Gravitational wave transient catalog
EoS	Equation of State
RMSE	Root-mean-square error
PN	Post-Newtonian
EM	Electromagnetic
PPE	Parameterized post-Einsteinian
EdGB	Einstein-dilaton-Gauss-Bonnet
sGB	scalar Gauss-Bonnet
ET	Einstein Telescope
DECIGO	Deci-hertz Interferometer Gravitational wave Observatory
NICER	Neutron Star Interior Composition Explorer
IMR	Inspiral-merger-ringdown
SNR	Signal-to-noise-ratio
ISCO	Innermost circular orbit
CMB	Cosmic microwave background
BAO	Baryon acoustic oscillation
MCMC	Markov chain Monte Carlo
FIM	Fisher information matrix
CVAE	Conditional variational autoencoder

VAE	Variational autoencoder
ELBO	Evidence lower bound
KL	Kullback-Leibler
KAGRA	Kamioka Gravitational Wave Detector

List of Symbols

$M_\odot$	Solar mass
M	Total mass for binary systems; stellar mass for single NS study
r	Radial coordinate
R	Radius
ρ_c	Central density of neutron star
ρ	Matter energy density
$T_{\mu\nu}$	Stress-energy tensor
u^μ	Four-velocity of fluid
$\nu(r)$	Function of r in metric Eq. (2.1)
$\lambda(r)$	Function of r in metric Eq. (2.1)
p	Pressure profile
ξ	r/R in Eq. (2.7)
α	Additional parameter in improved density profile Eq. (2.7)
I	Moment of inertia
Q	Quadrupole moment
$\mathcal{C}$	Compactness M/R
Ω	Angular velocity in Eq. (3.11)
λ	Tidal deformability in Eq. (3.21) (4.18)
k_2	Tidal Love number
Y_{lm}	Spherical harmonics
h_2, K_2	Quadrupolar tidal perturbations in Eq. (3.22)
y	Variable representing $\frac{\xi}{h_2}\frac{dh_2}{d\xi}$ in Eq. (3.23)
d_L	Luminosity distance, subscript of "em" or "gw" means measured through EM waves or GWs, "gw" subscript by default
z	Redshift
$\tilde{h}_A$	Metric perturbation in Fourier domain in Eq. (4.1)
$\mathcal{H}$	Scale factor a'/a in Eq. (4.1)
α_M	Friction term in Eq. (4.1)
α_{M0}	Value of α_M at present time
(Ξ_0, n)	Modified GW propagation parametrization in Eq. (4.3)
$M_{\rm eff}$	Effective Plack mass
Ω_M	Matter energy density parameter in Tab. 4.1

Ω_Λ	Dark energy density parameter
$\bar{n}$	Positive integer constant in Tab. 4.1
$\psi_{\rm T}$	Tidal contribution to GW phase
M_z	Redshifted mass
x	$(\pi M_z f)^{1/3}$ in Eq. (4.13)
$\tilde{h}(f)$	GW waveform in frequency domain
$\tilde{A}$	IMRPhenomD amplitude in Eq. (4.16)
$\psi_{\rm pp}$	(non-spinning) point-particle term in Eq. (4.17)
Γ_{ij}	Fisher matrix
S_n	Noise spectral density
$T_{\rm obs}$	Observation time in Eq. (4.26)
η	Symmetric mass ratio $m_1 m_2/M^2$
t_c	Time of coalescence
ϕ_c	Coalescence phase
H_0	Hubble constant
ω_0	Equation of state parameter of dark energy
$F_{ij}^{(\rm A)}$	Fisher matrix defined in Eq. (4.31)
$\mathcal{R}(z)$	Distribution of BNS mergers in Eq. (4.35).
$s(z)$	Redshift evolution of BNS merger rate in Eq. (4.35)
ϕ	Scalar field in action Eq. (5.1)
$\mathcal{R}_{\rm GB}$	Gauss-Bonnet invariant
$\alpha_{\rm em}$	Fraction of BNSs with EM counterparts in Eq. (4.37)
$\mathcal{R}$	Ricci scalar
$\alpha_{\rm GB}$	EdGB coupling constant
S_m	Matter action in Eq. (5.1)
$f(\phi)$	Function of scalar field in Eq. (5.1)
ζ	Dimensionless coupling constant $(16\pi\alpha_{\rm GB}^2)/L^4$
c_i	Coefficients in PN expansion for EdGB phase correction in Eq. (5.7)
v	Relative velocity of the binary, $(\pi M f)^{1/3}$, in Eq. (5.7)
$\mathcal{M}$	Chirp mass $(m_1 m_2)^{3/5}/M^{1/5}$
q	Mass ratio $m_2/m_1 (< 1)$
a_A	Dimensionless spin magnitudes in Eq. (5.11)
(θ_A, ϕ_A)	Polar and azimuthal angles of the spin angular momentum of Ath body
(α, δ)	Right ascension and declination of the binary in Eq. (5.11)

ψ	Polarization angle of GWs with respect to the earth-centered coordinates in Eq. (5.11)
ι	Inclination angle of the binary's orbital angular momentum relative to the detector's line of sight in Eq. (5.11)
$\phi_{\rm ref}$	Reference phase at the reference frequency
(θ_A, ϕ_A)	Polar and azimuthal angles of the spin angular momentum of the Ath body
s_A	Spin dependent factor in Eq. (E.5)
$(f_3^{\rm GB},\, f_4^{\rm GB})$	Correction to the tensor non-dipole emission in EdGB gravity at 1.5PN and 2PN orders in Eq. (5.7)
$\beta_i^{\rm PPE}$	Coefficients of EdGB corrections to phase in PPE framework in Eq. (E.14)

Table of Contents

List of Figures

List of Tables

Chapter 1

Introduction

For over a century, Einstein's theory of GR has been a resounding success in accurately predicting various astrophysical phenomena that continue to be observed to date. Despite its success, the theory has been subjected to numerous attempts to disprove it or consider it only part of a more comprehensive theory of nature. However, none of these attempts have been able to provide statistically significant evidence of deviations from GR. Nevertheless, many open questions remain that arise from observations and theories. These questions encompass topics such as the unification of GR and quantum mechanics [2–7], the origin of the accelerated expansion of the universe [3, 6–8], the origin of the missing mass in galaxies found through e.g. galactic rotation curves [2–5, 9] and the matter-antimatter asymmetry in the present universe [2, 4]. A standard solution for explaining the accelerated expansion of the universe and the missing mass in galaxies is to introduce the unknown matter, namely dark energy and dark matter. Another solution is to modify the gravity sector by going beyond GR. Various theories of gravity have been proposed to address these open questions, ranging from modifications to GR to entirely new theories. These proposed theories have the potential to explain the unresolved issues in astrophysics and cosmology. Many of these theories reduce to GR in the weak-field environment like our solar system, while may become active in the extreme-gravity regime where the gravitational fields are strong, nonlinear, and highly dynamical, precisely where GW observations can probe.

GW is a propagating disturbance in the fabric of spacetime, resulting from the acceleration of massive objects in the universe, such as colliding BBH or binary neutron star (BNS) mergers. A historic detection of GWs was made on September 14, 2015, by the Laser Interferometer Gravitational-wave Observatory (LIGO) in Hanford and Livingston. The GW event is known as GW150914 [10] and consists of a merger of a BBH. Another milestone observation was made in 2017 when LIGO and Virgo Collaboration (LVC, Virgo came online in 2017) detected GW signals from a coalescing BNS, known as GW170817 [11]. This event marked the dawn of multi-messenger astronomy as not only GW signals but also their associated EM counterparts were detected [12]. Recent updates of the GW catalog (GWTC-3) [13–16] reports, in total, 90 GW events from BBH, BNS, and NSBH mergers (see [17–19] for the previous catalogs). These events have been used to obtain implications on astrophysics, cosmology, nature of black holes (BHs), and nuclear physics (see studies on e.g. population properties of compact objects [20], Hubble tension [21], stochastic GW background [22], black hole spectroscopy [23], EoS of neutron stars (NSs) [24,25], and possible mode instabilities driven by NS tidal effects [26–28]). Recently, the worldwide network of GW detectors has expanded to include the Kamioka Gravitational Wave Detector (KAGRA) detector [29], and it is currently preparing for its upcoming fourth observing run (O4).

Although current tests of GR under extreme gravity conditions have not found any evidence beyond GR, the field of GW astronomy shows great promise, especially as it is still in its early stages. While the engineering design and sensitivity of the current observing runs by the LVC are remarkable, they are still hampered by the noise. Nevertheless, due to the overwhelming successes on the GW front, several funded and proposed GW detectors are being developed/planned. Besides upgrades to existing detectors, the "third generation" interferometers, such as the Cosmic Explorer (CE) [30] and the Einstein Telescope (ET) [31], are planned to be built at sites that are different from the LVC ones and are expected to have sensitivities up to ∼100 times greater than current detectors. Furthermore, space-based laboratories, such as the Laser Interferometer Space Antenna (LISA) [32], TianQin [33, 34], the Deci-Hertz Interferometer Gravitational wave Observatory (DECIGO) [35], and B-DECIGO [36], are in progress and will have sensitivities to GWs in sub-Hz frequency bands. Ground-based detectors, sensitive to high GW frequencies, can largely probe non-GR effects for stellar-mass BBHs, as they become more active at high relative velocities. Conversely, space-based detectors that operate at low frequencies are better suited to probing low-velocity effects. With such a promising future in observational GW astrophysics, the chance of discovering deviations from GR is increasing.

This thesis mainly focuses on testing GR with GWs from compact binaries involving NSs and BHs. The thesis consists of five main projects: (1) construction of improved analytic modeling of the NS interior [37], (2) proposing analytic I-Love-C relations for realistic NSs [38], (3) probing modified GW propagation through tidal measurements of BNS mergers [39], (4) constraining EdGB gravity from NSBH GW events [40], (5) performing Bayesian inference on beyond-GR parameters in BBH GW signals with the use of machine learning techniques. We will first provide motivations for each of the above projects and will then summarize the key findings in 1.1.

Before using NSs to test GR, we need to understand properties of NSs within GR. Let us first introduce the motivations for the construction of the improved analytic modeling of NS interiors. NSs are unique astrophysical objects for studying fundamental physics, in particular strongly-interacting many-body systems in nuclear physics [41]. NSs consist of matter with densities that can reach up to several times the nuclear saturation density in their inner cores, which are difficult to access with terrestrial nuclear experiments. Thus, they offer natural laboratories to probe nuclear matter EoS (the relation between pressure and energy density) that is difficult to access with ground-based nuclear experiments [42–44]. One way to extract the internal structure information is to measure the NS mass and radius independently [45–47], though current measurements may contain large systematic errors. For example, the X-ray payload NICER at the International Space Station recently measured the mass and radius of a pulsar to $\sim 10\%$ accuracy [48–53], which has been used to constrain the EoS and measure nuclear matter parameters [53–58]. Mass measurements of heavy NSs also help to constrain the EoS [59–61]. Another way to probe the internal structure is to measure the tidal deformabilities of NSs via GWs. The first BNS event detected, GW170817, favors softer EoSs [11, 62, 63] that tend to produce NSs with smaller radii and maximum masses. GW170817 can also be used to infer nuclear parameters around the saturation density [64, 65]. NSs are also useful to probe GR, as evidenced by binary pulsar [66, 67] and GW [12, 68] observations.

In order to connect NS observables (masses, radii, tidal deformabilities, etc.) to the internal structure, one needs to construct NS solutions by solving the Einstein equations with a given EoS. Most of such solutions are constructed numerically due to the complex nature of the field equations. Having said this, analytic solutions to the Einstein equations exist that can mimic realistic NS solutions. One simplest example is a solution with a constant density (Schwarzschild interior solution) [69]. Analytic solutions for modeling more realistic stars include Buchdahl [42, 69, 70] and Tolman VII [42, 71, 72] solutions. The latter is stable for a large range of compactness [73] and its geometric structures were studied in [74, 75].

Analytic NS solutions are useful to have a better understanding of NS physics. NS quasinormal modes and associated universal relations have been investigated in detail with the Tolman VII solution [76–78]. An analytic constant density solution with anisotropic pressure [79] was used to study how universal relations between moment of inertia (I), tidal Love number, and quadrupole moment (Q), and hence

I-Love-Q relations, approach the BH limit [80]. These analytic solutions for NSs can also be useful to examine non-GR theories. For example, constant density and Tolman VII solutions were used to investigate how stellar scalar charges vanish in string-inspired theories of gravity [81].

Next, we consider constructing analytic I-Love-C relations for realistic NSs. There are several other important global observables of NSs besides mass and radius (and their ratio gives the stellar compactness C) that are useful for probing nuclear physics. Moment of inertia I is expected to be measured from future observations of the double pulsar system [82]. A useful constraint on the EoS can be made if I can be determined up to about 10% [83]. Tidal deformability (related to the tidal Love number), which is a linear response of an object's quadrupole moment to the external tidal field, is encoded in GWs from BNS mergers [84,85]. GW170817 provides a first measurement of the tidal deformability [86], which has been used to constrain the EoS and nuclear matter parameters [63,87–98].

Unlike the mass-radius relation, which depends strongly on the underlying EoS, there exist universal relations among certain NS observables that do not depend sensitively on the stellar internal structure (see e.g. [99,100] for recent reviews). One example is among the moment of inertia I, the tidal Love number (or the tidal deformability), and the quadrupole moment Q, which are commonly known as the I-Love-Q relations [101,102]. The relations are universal, with an EoS-variation of $\sim 1\%$. Similar relations were discovered among tidal parameters in gravitational waveforms from BNSs, known as the binary Love relations [103, 104]. These relations can be used to break degeneracies among parameters in GW signals, enhancing the measurability of the tidal effects directly related to the EoS [86]. The relations have many other interesting applications, including astrophysics, gravitational physics, and cosmology [101–106]. Reference [107] proposed emergent, approximate symmetry related to isodensity contours inside NSs as a possible origin of the universality. Reference [108] proposed that the universality is due to the realistic EoSs being "close" to the incompressible, constant density one, which agrees with the picture of [107] since the approximate symmetry becomes exact in the incompressible limit.

Most of the works on NS universal relations focused on numerical calculations, though there is a limited number of works within the analytic framework. The amount of universality in the I-Love relation was analytically explained in the Newtonian limit by comparing the $n = 0$ and $n = 1$ polytropes [101, 102]. Reference [1] derived the analytic, I-Love relation for constant density stars that is applicable to both the Newtonian and relativistic regimes. The authors studied the relation between the moment of inertia and compactness (the I-C relation) and that between the tidal deformability and compactness (the Love-C relation) in terms of a series expansion in compactness. The authors then eliminated the compactness to find the analytic I-Love relation. Since constant density stars are more appropriate for describing quark stars, what is still missing is the analytic, I-Love-C relations for *realistic* NSs and study analytically the amount of the EoS-variation in these relations.

After completion of works on NSs and their properties, we next explore a novel approach to probe modified GW propagation through tidal measurements of BNS mergers. The first BNS GW event LVC detected, GW170817, serves as a standard siren to probe cosmology, in particular measuring the Hubble constant [109–111]. This constant is inferred from the independent measurement of the luminosity distance and the redshift of the source. The former is measured from the GW amplitude, while the latter is obtained by identifying the host galaxy through EM counterpart observations. Another important application of GW170817 is to test GR. GW170817 has been used to probe the modified dispersion relation of GWs. For example, the comparison of the arrival time difference between GW and EM wave signals placed a bound on the fractional difference in the propagation speed of GWs with respect to the speed of light to be one part in 10^{-15} [12].

Standard sirens like GW170817 can also probe other aspects of the modified GW propagation, in particular the modified friction term in the GW evolution. This in turn modifies the GW amplitude from its GR counterpart, and thus the luminosity distance measured with GWs may differ from that measured through EM observations. Alternatively, one can use the luminosity distance and redshift measurement of standard sirens to probe both cosmology and modified GW propagation. This has been demonstrated for future GW observations with advanced LIGO with its design sensitivity, ET, and LISA [112–115], assuming that the luminosity distance is measured through GWs while the redshift is obtained from that of the host galaxy that is identified through EM counterparts. If there are no associated EM counterparts, one can still use such GW sources as "dark sirens" to probe cosmology and gravity by taking their correlation with galaxy catalogs [116, 117]. One example of "dark sirens" is the second BNS event, GW190425 [118], found in the third observing run by LVC, but no EM counterpart is confirmed yet. In our research, we examined a distinctive method of utilizing this "dark sirens" as a means of investigating the modified propagation of GWs through tidal effects in BNS system.

Next, we switch gears and explore tightening constraints on a specific beyond-GR theory of gravity, EdGB gravity, using NSBH mergers. As already mentioned, GW events are also ideal sources to probe strong/dynamical fields of gravity [68, 119–122] that are difficult to access through other experiments/observations, including table-top and solar system experiments, or binary pulsar and cosmological observations. For example, they have been used to probe the mass of the graviton [119–121], scalar-tensor theories (Brans-Dicke theory, those with scalarization phenomena proposed by Damour and Esposito-Farèse, screened modified gravity, and the time dependence of the scalar field) [120, 123, 124], light axion fields sourced by NSs [125], and dynamical Chern-Simons gravity [120, 126–129])

Scalar Gauss-Bonnet (sGB) gravity [130–133] is another theory beyond GR that has been studied extensively. In the action, a dynamical scalar field is coupled to a Gauss-Bonnet (GB) invariant (consisting of a certain combination of curvature-squared scalars) with a coupling constant $\alpha_{\rm GB}$ that has a dimension of length squared.

Depending on what kind of coupling one considers, one recovers a shift-symmetric theory (linear coupling) [134, 135], EdGB gravity [136–139] (exponential coupling) motivated by string theory and inflation [140, 141], and a theory admitting spontaneous scalarization of BHs and NSs (quadratic coupling is an example) [142–145].

EdGB gravity has been constrained by GWs from BBHs, together with other astrophysical constraints from a BH low-mass x-ray binary (LMXB) and NS observations. The current upper bound on the coupling constant $\sqrt{\alpha_{\rm GB}}$ is $\sim$ 1km. For example, Perkins et al. [127] combined bounds on $\sqrt{\alpha_{\rm GB}}$ from 6 selected BBH events from the GW catalogs GWTC-1 and GWTC-2 and found the bound $\sqrt{\alpha_{\rm GB}} \lesssim 1.7\,\mathrm{km}$. These GW bounds are obtained by taking into account the leading correction to the gravitational waveform phase that enters at -1 post-Newtonian (PN) order relative to GR due to the scalar dipole radiation [120, 134]. In our work, we not only further constrain the upper bound on $\sqrt{\alpha_{\rm GB}}$ with newly detected NSBH events, but also investigate how inclusion of higher PN order (beyond -1 PN) corrections to the phase influence the bound.

In our most recent project, we started training a neural network to perform a GW data analysis in theories beyond GR. As introduced in the previous project, gaining insight into fundamental physics from GW data requires intensive computational modeling and data analysis to reduce the data and extract relevant model parameters. Performing these analyses, and in particular, testing the predictions of GR with GWs, requires computationally expensive and time-consuming Bayesian statistics [146,147] and stochastic sampling techniques (such as MCMC [148,149] or nested sampling [150, 151]) to infer a posterior probability distribution that encodes all the properties of the source. In this process, an involved likelihood function must be evaluated $O(10^7)$–$O(10^8)$ times. As the number of parameters used to describe the source increases, the larger parameter space requires the likelihood to be evaluated more frequently, further slowing down the process. This is particularly problematic for testing GR with GWs, because many additional parameters beyond those in GR must be introduced to parametrize the deviations from GR that can appear in the GWs. For the large number of parameters that appear in some extensions of GR, the standard random sampling techniques of the likelihood function become computationally prohibitive. For instance, in our last project on constraining EdGB gravity, each Bayesian inference (with one more EdGB parameter to infer) performed on the strain data takes approximately a day to finish. Thus, there is a strong need to speed up the inference procedures for beyond-GR theories.

Over the course of recent years, machine learning has emerged as a prominent tool in GW research. The employment of these machine learning models has demonstrated considerable potential in the domains of signal identification [152–154], the categorization of anomalous transients [155], the enhancement of Bayesian sampling methodologies [156], and in particular, the speed-up of parameter estimation for GW data analysis [157–160]. In [158], one type of neural network has been shown to decrease the analysis time by a factor of 10^6 for simulated GW data from BBH in GR.

Our main goal in this project then is to build off these initial successes in GR and to train a neural network to perform a GW data analysis in theories beyond GR. With these machine-learning techniques, we aim to study a wider range of theories than in previous research. This will give a more accurate representation of how well beyond-GR theories can be constrained with GWs. It will also provide a more efficient framework for searching for deviations from GR that may begin appearing in the data once current (and future) detectors begin operating with a sufficiently improved sensitivity that some of the subtle effects currently hidden in the noise begin to emerge from these instrumental backgrounds.

1.1 Executive Summary

We now move on to explaining the primary outcomes of this thesis briefly. A more in-depth summary of each project can be found in the concluding section of each chapter on the project.

1.1.1 Improved analytic modeling of neutron star interiors

We summarize the improved analytic modeling of NS interiors in this section. To establish a connection between measurable observables, it is essential to develop an accurate analytic model of the NS interior. Although the Tolman VII solution, which depends solely on two parameters such as mass and radius, provides a solution for static and isolated NSs, it does not perfectly correspond with numerical solutions. In this work, we present an enhanced analytic model based on the Tolman VII solution. Our proposed model incorporates an additional parameter to improve the agreement between the analytic density profile and numerically obtained results. This new parameter can be accurately determined based on the central density, radius, and NS mass in an EoS-insensitive manner. Our investigations reveal that the new model provides a more precise representation of realistic profiles compared to the original Tolman VII solution, with a factor of improvement ranging from 2 to 5. The original Tolman solution and the improved model are summarized in Table 1.1. Detailed descriptions of how to obtain those expressions are presented in Chap. 2.

1.1.2 Analytic I-Love-C relations for realistic neutron stars

In this section, we summarize the construction of the analytic I-Love-C relation in this thesis. We first constructed the analytic I-C and Love-C relations by perturbing the original Tolman VII solution to introduce slow spin and weak tidal deformation. We then solve the perturbed Einstein equations in terms of a series expansion in compactness order by order. After resumming the series via Padé method as done in [108] for constant density stars, we found the normalized moment of inertia $\bar{I} \equiv I/M^3$ and tidal deformability $\bar{\lambda} \equiv \lambda/M^5$ as

$$\bar{I}_{\rm Tol} = \frac{\sum_{j=0}^{3} c_j^{(\bar{I})} \mathcal{C}^j}{2\mathcal{C}^3 \sum_{i=0}^{3} d_i^{(\bar{I})} \mathcal{C}^i}, \tag{1.1}$$

$$\begin{aligned} \bar{\lambda} = {} & \frac{16}{15}(1-2\mathcal{C})^2[2+2\mathcal{C}(y_R-1)-y_R] \\ & /\{2\mathcal{C}[6-3y_R+3\mathcal{C}(5y_R-8)] \\ & +4\mathcal{C}^3[13-11y_R+\mathcal{C}(3y_R-2)+2\mathcal{C}^2(1+y_R)] \\ & +3(1-2\mathcal{C})^2[2-y_R+2\mathcal{C}(y_R-1)]\ln(1-2\mathcal{C})\}, \end{aligned} \tag{1.2}$$

with,

$$y_{R,\rm Tol} = \frac{\sum_{j=0}^{2} c_j^{(\bar{\lambda})} \mathcal{C}^j}{\sum_{i=0}^{2} d_i^{(\bar{\lambda})} \mathcal{C}^i}, \tag{1.3}$$

where the coefficients c_i and d_i are given in Table 1.2. We also present these analytic relations in a supplemental Mathematica notebook [161]. Here, the subscript “Tol” stands for the original Tolman VII solution.

Figure 1.1 compares these analytic relations with numerical ones for NSs with realistic EoSs and the analytic one for constant density stars. Observe that the analytic relations for the Tolman VII model can accurately describe the realistic relations. We can see the analytic curves are very close to the numerical fit in [99], with fractional differences $\sim 1\%$ for the I-C curve and several percents for the Love-C curve. Observe also that the former is much more accurate than the one for constant-density stars which, again, is more appropriate for quark stars. We next constructed the I-Love relation semi-analytically for the original Tolman VII solution by eliminating the compactness from the I-C and Love-C relations, which accurately models the numerical results.

Original Tolman	$\rho_{\text{Tol}} = \frac{15\mathcal{C}}{8\pi R^2}(1-\xi^2)$ $m_{\text{Tol}} = R\,\mathcal{C}\left(\frac{5}{2}\xi^3 - \frac{3}{2}\xi^5\right)$ $e^{\nu_{\text{Tol}}} = C_1^{\text{Tol}}\cos^2\phi_{\text{Tol}}$ $p_{\text{Tol}} = \frac{1}{4\pi R^2}\left[\sqrt{3\mathcal{C}e^{-\lambda_{\text{Tol}}}}\tan\phi_{\text{Tol}} - \frac{\mathcal{C}}{2}(5-3\xi^2)\right]$ $\phi_{\text{Tol}} = C_2^{\text{Tol}} - \frac{1}{2}\log\left(\xi^2 - \frac{5}{6} + \sqrt{\frac{e^{-\lambda_{\text{Tol}}}}{3\mathcal{C}}}\right)$ $C_1^{\text{Tol}} = 1 - \frac{5\mathcal{C}}{3}$ $C_2^{\text{Tol}} = \arctan\sqrt{\frac{\mathcal{C}}{3(1-2\mathcal{C})}} + \frac{1}{2}\log\left(\frac{1}{6} + \sqrt{\frac{1-2\mathcal{C}}{3\mathcal{C}}}\right)$
Improved Tolman	$\rho_{\text{imp}} = \rho_c\left[1-\alpha\xi^2+(\alpha-1)\xi^4\right]$ $m_{\text{imp}} = 4\pi\rho_c R^3\left(\frac{\xi^3}{3} - \frac{\alpha\xi^5}{5} + \frac{\alpha-1}{7}\xi^7\right)$ $e^{\nu_{\text{imp}}} = C_1^{\text{imp}}\cos^2\phi_{\text{imp}}$ $p_{\text{imp}} = \sqrt{\frac{e^{-\lambda_{\text{Tol}}}\rho_c}{10\pi}}\frac{\tan\phi_{\text{imp}}}{R} + \frac{1}{15}\left(3\xi^2-5\right)\rho_c$ $+\frac{6(1-\alpha)\rho_c}{16\pi(10-3\alpha)\rho_c R^2-105}$ $\phi_{\text{imp}} = C_2^{\text{imp}} - \frac{1}{2}\log\left(\xi^2 - \frac{5}{6} + \sqrt{\frac{5e^{-\lambda_{\text{Tol}}}}{8\pi R^2\rho_c}}\right)$ $C_1^{\text{imp}} = (1-2\mathcal{C})\left\{1 + \frac{8\pi R^2\rho_c(10-3\alpha)^2(15-16\pi R^2\rho_c)}{3[105+16\pi R^2\rho_c(3\alpha-10)]^2}\right\}$ $C_2^{\text{imp}} = \arctan\left[-\frac{2(10-3\alpha)R\sqrt{6\pi\rho_c(15-16\pi\rho_c R^2)}}{48\pi(10-3\alpha)\rho_c R^2-315}\right]$ $+\frac{1}{2}\log\left(\frac{1}{6} + \sqrt{\frac{5}{8\pi\rho_c R^2} - \frac{2}{3}}\right)$ $\alpha = a_0 + a_1\left(\frac{\mathcal{C}^n}{\rho_c R^2}\right) + a_2\left(\frac{\mathcal{C}^n}{\rho_c R^2}\right)^2$

Table 1.1: Summary of the original Tolman solution (top) and the improved model (bottom), with $\xi = r/R$ where R is the stellar radius. We present the energy density ρ, the interior mass function m, the (t,t) component of the metric $e^{\nu}(= -g_{tt})$, and the pressure p. The (r,r) component of the metric is related to m as $g_{rr} = e^{\lambda} = (1-2m/r)^{-1}$. Fitting coefficients a_0, a_1, a_2 and n in α are summarized in Table 2.2. The (R,ρ_c) parameterization of the original Tolman solution (with ρ_c representing the energy density at the stellar center) is obtained by setting the stellar compactness as $\mathcal{C} = (8\pi/15)R^2\rho_c$, while the (R,M) parameterization of the original Tolman solution (where M is the stellar mass) and the improved Tolman model uses $\mathcal{C} = M/R$. We stress that $\lambda \equiv -\ln(1-2m/r)$ entering in p_{imp} and ϕ_{imp} is λ_{Tol} and not λ_{imp}.

Coefficient	Value
$c_0^{(\bar{I})}$	0
$c_1^{(\bar{I})}$	$\frac{4}{7}$
$c_2^{(\bar{I})}$	$-\frac{4475212734657724923440}{3819744665891770040271}$
$c_3^{(\bar{I})}$	$\frac{52512054644310254173804264}{119920883785672120414308045}$
$d_0^{(\bar{I})}$	1
$d_1^{(\bar{I})}$	$-\frac{52610171361202024028}{16535691194336666841}$
$d_2^{(\bar{I})}$	$\frac{7315710780062174885366}{2662246282288203361401}$
$d_3^{(\bar{I})}$	$-\frac{24682764601232290703083888}{47294805204849932715288765}$
$c_0^{(\bar{\lambda})}$	$\frac{75974923394}{756262478125}$
$c_1^{(\bar{\lambda})}$	$\frac{37520415660320803457514031332847380947962712}{4113772401871789717923024281035002577115625}$
$c_2^{(\bar{\lambda})}$	$\frac{959692101525501001392591086078567807004592397}{9214850180192808968147574389518405772739000}$
$d_0^{(\bar{\lambda})}$	1
$d_1^{(\bar{\lambda})}$	$\frac{125977972708997462470931885904739}{1673725935459728881079142766212}$
$d_2^{(\bar{\lambda})}$	$-\frac{11560237280939583134679473198513569}{70296489289308613005323996180904}$

Table 1.2: Coefficients $c_i^{(\bar{I})}$, $d_i^{(\bar{I})}$ in Eq. (1.1) and $c_i^{(\bar{\lambda})}$, $d_i^{(\bar{\lambda})}$ in Eq. (1.3).

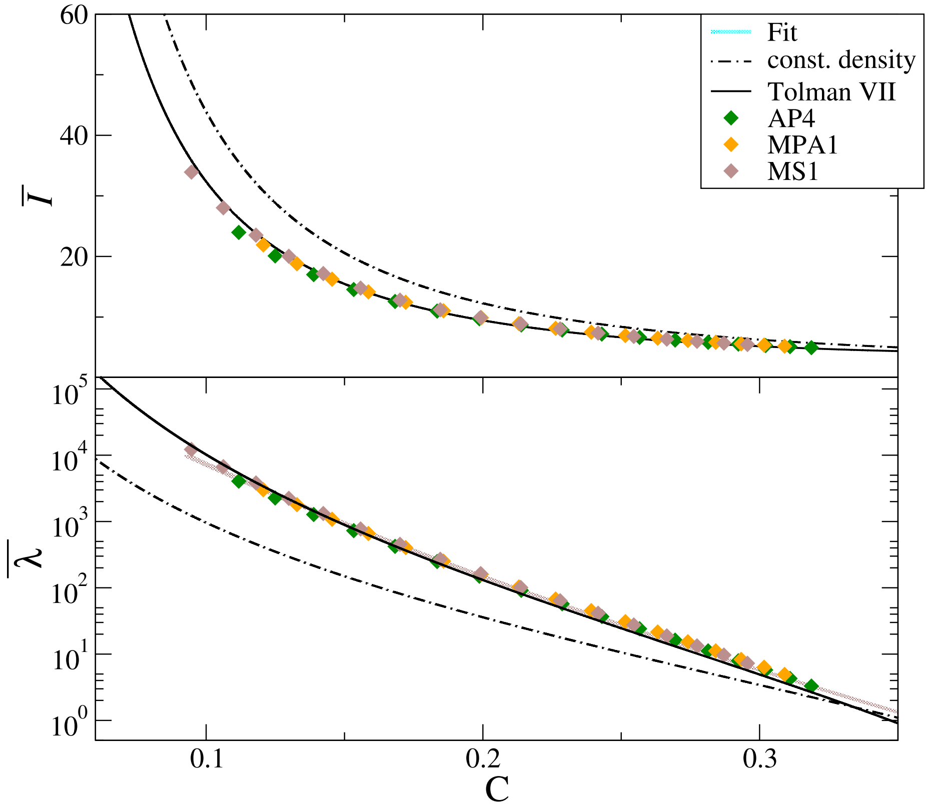

Figure 1.1: Approximate, analytic I-C relation (top) and Love-C relation (bottom) for the original Tolman VII model (solid) and constant-density-star model [1] (dotted-dashed), both in Padé resummed form. We also present those for realistic EoSs representing soft (AP4), intermediate (MPA1), and stiff (MS1) EoS classes. We can see a clear improvement in the accuracy of the Tolman-VII curves over the constant-density ones in both panels. For comparison, the numerical fits in [99] are plotted in cyan.

We also derived the analytic I-C/Love-C and semi-analytic I-Love relations for the modified Tolman VII model [162]. By varying the density profile parameter α that corresponds to varying the EoS, we successfully obtained the 10% EoS-variation in the I-C and Love-C relations while 1% EoS-variation in the I-Love relations, which agree with previous numerical findings [99, 101, 102, 163, 164]. This suggests that the origin of the universality in the I-C and Love-C relations for realistic NSs (that are quite different from those for constant-density and quark stars) can be attributed to the fact that the energy density profiles inside realistic NSs can be approximated by the Tolman VII one (a simple quadratic function).

1.1.3 Probing modified GW propagation through tidal effects in binary neutron star mergers

We here present a brief summary of our findings in probing modified GW propagation through tidal effects in BNS mergers. We first compute the measurability of the BNS redshift with GW observations alone, and find that multi-band observations between ground-based (ET) and space-based (DECIGO) GW detectors improve the accuracy by $\sim$ 50% compared to the case with ET only. Next, we show the bound on Ξ_0 that controls the amount of friction in the modified GW propagation in a model-independent way. Figure 1.2 presents such a bound against the fraction $\alpha_{\rm em}$ of BNS events within the redshift range of $z = [0.1, 2]$ whose redshift is identified through EM counterparts. We choose a representative case of $n = 2.5$ (the parameter n determines the redshift dependence of the modified GW propagation) and SLy EoS. Observe that the addition of BNSs without EM counterparts improves the bound by a factor of a few in the case of ET alone, and the bound further improves if one uses multi-band observations. Although the figure is only for $n = 2.5$, we find that the bound on Ξ_0 is insensitive to the choice of n. Lastly, we map the bound on Ξ_0 to parameters in specific non-GR theories. In the case of a scalar-tensor theory, for example, the relevant parameter can be constrained to a level of $\sim 10^{-2}$.

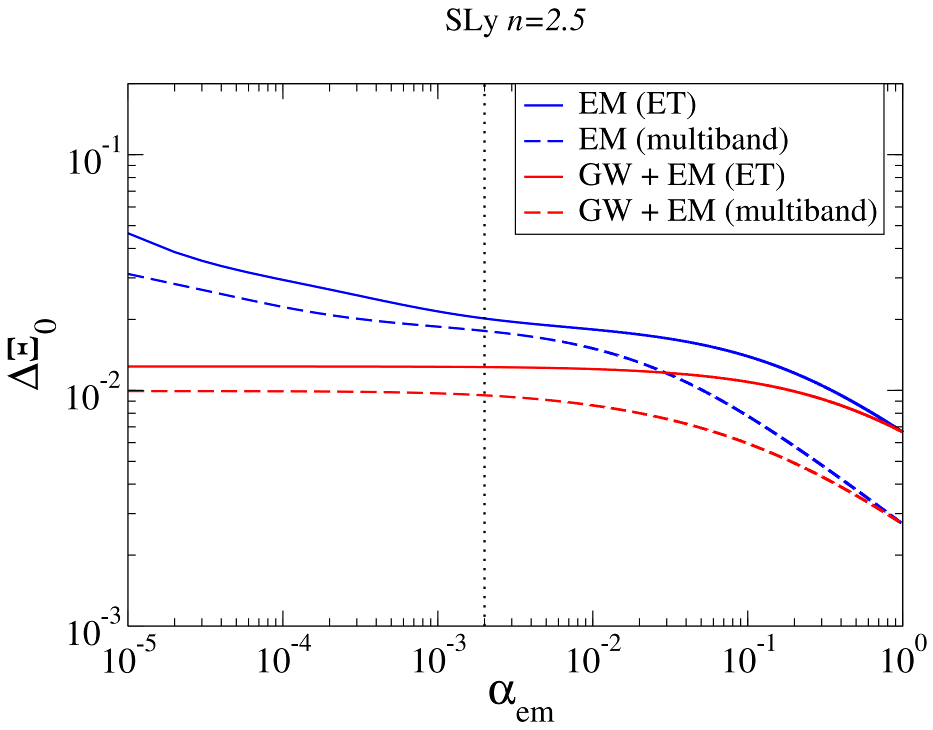

Figure 1.2: Measurability of the modified GW propagation parameter Ξ_0 as a function of the fraction α_{em} of the events with redshift identification through EM counterparts. We show results for (i) using only BNS events with EM counterparts ("EM" as in Eq. (4.37), as done in previous literature) and (ii) combining BNS events with and without EM counterparts ("GW+EM" in Eq. (4.38)). We consider observations with ET alone and multi-band observations (with an observation time of 3 yrs for the latter). We use SLy EOS and set $n = 2.5$ in Eq. (4.3). The vertical dashed line at $\alpha_{\mathrm{em}} = 2 \times 10^{-3}$ corresponds to the typical fraction of BNSs with EM counterparts [165]. Observe that the addition of BNSs without EM counterparts improves the measurability from those with EM counterpart by a factor of a few.

1.1.4 Constraints on EdGB gravity from Black Hole Neutron Star binary GW event

In this section, we summarize our works on constraining EdGB gravity from GW events. In particular, we use two new NSBH binaries (GW200105 and GW200115).

	LMXB	NS	GW (BBH)		**GW (NSBH) (this work)**	
			O1–O2	O1–O3	**GW200115**	**combined**
$\sqrt{\alpha_{\rm GB}}$ [km]	1.9 [131]	1.29 [166]	5.6 [126] 1.85 [167] 4.3 [169]	1.7 [127] 4.5 [168] (0.4) [168]	1.33	1.18

Table 1.3: Astrophysical bounds on EdGB gravity. We show bounds from a LMXB, NSs ($\sim 2M_\odot$ NSs), GWs from BBHs, and NSBHs (this work). The one in brackets comes from GW190814 assuming that it is a BBH, which has some uncertainty. For NSBH, we present the bound from GW200115 and that by combining NSBHs (GW200115, GW200105, and GW190814; assuming the last one as a NSBH is a conservative choice) and BBHs from [127].

We also consider GW190814, which is consistent with both a BBH and a NSBH binary. Adopting the leading PN correction and carrying out a Bayesian Markov-chain Monte Carlo (MCMC) analyses, we derive the 90% credible upper bound on the coupling constant of the theory as $\sqrt{\alpha_{\rm GB}} \lesssim 1.33\,\text{km}$ for GW200115, whose consistency is checked with an independent Fisher analysis. This bound is stronger than the bound obtained in previous literature by combining selected BBH events in GWTC-1 and GWTC-2 catalogs. We also derive a combined bound of $\sqrt{\alpha_{\rm GB}} \lesssim 1.18\,\text{km}$ by stacking GW200105, GW200115, GW190814, and selected BBH events. In order to check the validity of the effect of higher PN terms, we derive corrections to the waveform phase up to second PN order by mapping results in scalar-tensor theories to EdGB gravity. We find that such higher-order terms improve the bounds by 14.5% for GW200105 and 6.9% for GW200115, respectively. Such a finding is consistent with the analysis in [127]. The constraints on EdGB gravity obtained from our work and previous papers by others are summarized in Table 1.3.

1.1.5 Machine learning enabled test of beyond-GR gravity

In this section, we summarize our recent progress in using neural networks to perform tests of GR with GWs. Currently, we are still in the stage of reproducing the training results shown in previous literature [158] within the framework of GR. We tested our model on 4-parameter (the primary mass m_1, the secondary mass m_2, the coalescence time t_c and the luminosity distance d_L) BBH signal parameter estimation. We achieved approximately 100 times speedup compared to the traditional Dynesty sampler. The posterior distributions we obtained from the neural network model are more centered around the injected values of the simulated strain data. However, the neural network still has trouble mimicking the shape of the posterior distribution given by traditional sampling methods. As our next step, we will combine additional components, normalizing flows, to the current network to increase the flexibility of the network, as suggested in [160].

1.2 Organization and conventions

Let us present a brief outline of this thesis. Chapter 2 and 3 focus on the analytic description of NSs. Specifically, chapter 2 presents an improved analytic modeling of the NS interior, which serves as a prerequisite of the next chapter. In chapter 3, we derived analytic, approximate I-Love-C relations for NSs with various EoSs. Chapter 4 discusses the measurement of beyond GR effect in the propagation of GWs through tidal effects in BNS mergers. In chapter 5, we derive bounds on EdGB gravity with NSBH GW events and check whether including higher order PN corrections affect the inference results. Chapter 6 presents our recent progress on training neural networks to perform Bayesian inference on BBH signals and some improvements we plan to implement. At the end of each chapter, there is a concluding section that emphasizes the significant findings of the respective chapter. Certain intricate technical aspects are presented in the Appendices for the sake of clarity and concision. We use the convention $G = c = 1$ throughout the thesis.

Part A

Properties of neutron stars and Testing general relativity with binary neutron stars

Chapter 2

Improved Analytic Modeling of Neutron Star Interiors

2.1 Introduction

In this chapter, we construct an improved analytic modeling of NS interiors. We begin by comparing the Tolman VII solution with numerical solutions. The density profile among these solutions were investigated in [42]. Here, we also study the profiles for the interior mass, gravitational potential and pressure. For a $1.4M_\odot$ NS with the AP4 EoS (a soft EoS consistent with the LVC tidal measurement [11, 62, 63]), the density and mass profiles for the Tolman solution match with the numerical ones with a typical error of $\sim 10\%$.

The main goal of this project is to find an analytic model of the NS interior that can more accurately describe the realistic solution obtained numerically than the original Tolman VII solution. The latter models the density to be a quadratic function of the radial coordinate r. We here introduce an additional parameter α to allow the density to be a quartic function of r. We find an approximate universal relation among this additional parameter and the stellar mass M, radius R and central density ρ_c that is insensitive to the underlying EoS. The final expression is a three-parameter solution in terms of M, R and ρ_c. The price one has to pay by introducing the additional parameter is that the density profile is slightly more complicated than the original model, and we could not find an *exact* analytic solution to the Einstein equations.

Having said this, we managed to find an approximate, three-parameter solution that can more accurately model realistic profiles than the original Tolman VII solution in most cases. For example, the density and mass profiles of a $1.4M_\odot$ NS with the AP4 EoS now agree with the numerical ones within an error of $\sim 1\%$. Regarding other masses and EoSs, the new model can more accurately model numerical results compared to the original Tolman solution by a factor of 2–5. The new model outperforms the original one, especially for softer EoSs with a relatively large mass ($> 1.5M_\odot$). The accuracy of the new model can be improved further if we use a fit for α that is specific to each EoS, though the improvement from the case with the universal-α fit is not so significant.

The remaining of this chapter is organized as follows. In Sec. 2.2, we review the original Tolman VII solution, while in Sec. 2.3, we present our new model. In Sec. 2.4, we compare the two models and show that the new model has better agreement with numerical solutions than the original model in most cases, especially for softer EoS. We conclude in Sec. 2.5 and give possible directions for future work.

2.2 Tolman VII solution

We begin by reviewing the original Tolman VII solution [71] that can mimic static and spherically symmetric NSs [42]. We use the metric ansatz given by

$$ds^2 = -e^{\nu} dt^2 + e^{\lambda} dr^2 + r^2 (d\theta^2 + \sin^2\theta d\phi^2). \tag{2.1}$$

Here, ν and λ are functions of r only. We assume matter inside a NS can be modeled by a perfect fluid whose stress-energy tensor is given by

$$T_{\mu\nu} = (\rho + p) u_{\mu} u_{\nu} + p g_{\mu\nu}, \tag{2.2}$$

where u^{μ} is the four-velocity of the fluid while ρ and p represent the matter energy density and pressure respectively.

Substituting Eqs. (2.1) and (2.2) into the Einstein equations, one finds independent equations as [71]

$$\frac{d}{dr}\left(\frac{e^{-\lambda} - 1}{r^2}\right) + \frac{d}{dr}\left(\frac{e^{-\lambda}\nu'}{2r}\right) + e^{-\lambda-\nu}\frac{d}{dr}\left(\frac{e^{\nu}\nu'}{2r}\right) = 0, \tag{2.3}$$

$$e^{-\lambda}\left(\frac{\nu'}{r} + \frac{1}{r^2}\right) - \frac{1}{r^2} = 8\pi p, \tag{2.4}$$

$$\frac{dm}{dr} = 4\pi r^2 \rho, \tag{2.5}$$

where a prime denotes a derivative with respect to r and

$$e^{-\lambda} \equiv 1 - \frac{2m}{r}\,. \tag{2.6}$$

To close the system of equations, one normally chooses an EoS that relates p as a function of ρ.

Instead of choosing an EoS, Tolman specified $e^{-\lambda}$ to be a quartic function of r. This leads to the energy density profile of

$$\rho_{\text{Tol}}(r) = \rho_c(1-\xi^2), \tag{2.7}$$

where $\xi = r/R$ with R representing the stellar radius and ρ_c being the central energy density. The subscript "Tol" refers to the quantity in the original Tolman solution. Substituting this into Eq. (2.5) and integrating over r with the boundary condition $m(0) = 0$, one finds

$$m_{\text{Tol}}(r) = 4\pi\rho_c\left(\frac{r^3}{3} - \frac{r^5}{5R^2}\right). \tag{2.8}$$

ρ_c can be expressed in terms of the stellar mass $M \equiv m(R)$ as

$$\rho_c = \frac{15M}{8\pi R^3}. \tag{2.9}$$

Substituting this back into Eqs. (2.7) and (2.8), one finds

$$\begin{aligned} \rho_{\text{Tol}}(r) &= \frac{15M}{8\pi R^3}(1-\xi^2), && (2.10)\\ m_{\text{Tol}}(r) &= M\left(\frac{5}{2}\xi^3 - \frac{3}{2}\xi^5\right). && (2.11) \end{aligned}$$

$e^{-\lambda}$ is given by a quartic polynomial in terms of ξ as

$$e^{-\lambda_{\text{Tol}}(r)} = 1 - \mathcal{C}\xi^2\left(5-3\xi^2\right) \tag{2.12}$$

$$= \quad 1 - \frac{8\pi}{15} R^2 \rho_c \xi^2 \left(5 - 3\xi^2\right), \tag{2.13}$$

where

$$\mathcal{C} \equiv \frac{M}{R} = \frac{8\pi}{15} R^2 \rho_c \tag{2.14}$$

is the stellar compactness.

With these expressions at hand, Tolman [71] analytically solved for ν and p. First, Eq. (2.3) can be integrated to yield

$$e^{\nu_{\text{Tol}}(r)} = C_1^{\text{Tol}} \cos^2 \phi_{\text{Tol}}, \tag{2.15}$$

with

$$\begin{aligned} \phi_{\text{Tol}} &= C_2^{\text{Tol}} - \frac{1}{2} \log \left(\xi^2 - \frac{5}{6} + \sqrt{\frac{e^{-\lambda_{\text{Tol}}}}{3\mathcal{C}}} \right) \\ &= C_2^{\text{Tol}} - \frac{1}{2} \log \left(\xi^2 - \frac{5}{6} + \sqrt{\frac{3e^{-\lambda_{\text{Tol}}}}{8\pi R^2 \rho_c}} \right). \end{aligned} \tag{2.16}$$

The integration constants C_1^{Tol} and C_2^{Tol} are determined from the boundary conditions

$$e^{\nu_{\text{Tol}}(R)} = 1 - \frac{2M}{R}, \qquad p_{\text{Tol}}(R) = 0, \tag{2.17}$$

with p_{Tol} given by Eq. (2.4). One finds

$$C_1^{\text{Tol}} = 1 - \frac{5\mathcal{C}}{3}, \tag{2.18}$$

$$C_2^{\text{Tol}} = \arctan \sqrt{\frac{\mathcal{C}}{3(1-2\mathcal{C})}} + \frac{1}{2} \log \left(\frac{1}{6} + \sqrt{\frac{1-2\mathcal{C}}{3\mathcal{C}}} \right), \tag{2.19}$$

and

$$p_{\rm Tol} = \frac{1}{4\pi R^2}\left[\sqrt{3\mathcal{C}e^{-\lambda}}\tan\phi_{\rm Tol} - \frac{\mathcal{C}}{2}(5-3\xi^2)\right]. \tag{2.20}$$

The above solution is the so-called Tolman VII solution.

Figure 2.1 presents the normalized energy density and pressure profiles of a $1.4M_\odot$ NS with the AP4 EoS for two different parameterizations of the original Tolman solution. For reference, we also show realistic profiles obtained numerically. Regarding the energy density profile, observe that the (R, ρ_c) parameterization more accurately models the realistic profile near the stellar center. This is because the central density is a free parameter that we can choose to be the value that matches the one with the numerical calculation. On the other hand, the (R, M) parameterization works better in the intermediate regime of the star. We found a similar feature for the m profile, as it is obtained simply by integrating ρ over a volume, as in Eq. (2.5).

Regarding the pressure profile, the (R, M) parametrization works better throughout, and we found a similar feature for the ν profile. This is because p is obtained from ν (see Eq. (2.4)), which is determined from the boundary condition at the stellar surface in terms of R and M (Eq. (2.17)). Thus, the (R, M) parameterization allows one to match ν at the surface perfectly with the numerical value. This suggests that perhaps the (R, M) parameterization has more advantage than the (R, ρ_c) one, except near the center of the ρ and m profiles.

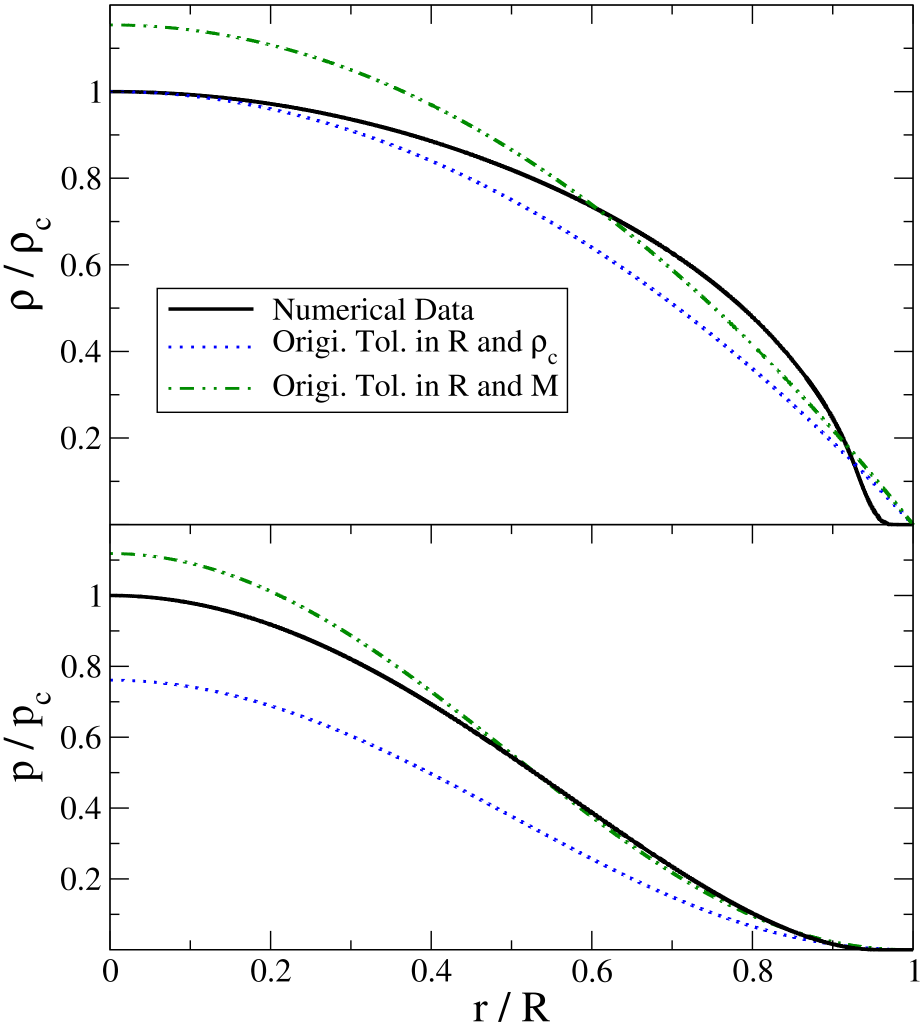

Figure 2.1: Energy density (top) and pressure (bottom) profiles for the original Tolman solution with two different parameterization. We choose $R = 11.4$km and either $\rho_c = 9.9 \times 10^{14}$g/cm^3 or $M = 1.4 M_\odot$. We also present the numerical solution with the AP4 EoS and $\rho_c = 9.9 \times 10^{14}$g/cm^3 that corresponds to $M = 1.4 M_\odot$ and $R = 11.4$km.

2.3 Improved Tolman VII modelling

We here propose an improved model which has three free parameters (M, R, ρ_c). We begin by introducing an additional term to Eq. (2.7):

$$\rho_{\rm imp}(r) = \rho_c \left[1 - \alpha\xi^2 + (\alpha - 1)\xi^4\right], \tag{2.21}$$

with a constant α. The coefficients are chosen such that $\rho_{\rm imp}(R) = 0$. The original Tolman solution is recovered in the limit $\alpha \to 1$. m and λ now become

$$\begin{aligned} m_{\rm imp} &= 4\pi\rho_c R^3\xi^3 \left(\frac{1}{3} - \frac{\alpha}{5}\xi^2 + \frac{\alpha-1}{7}\xi^4\right), & (2.22)\\ e^{-\lambda_{\rm imp}} &= 1 - 8\pi R^2\xi^2\rho_c \left(\frac{1}{3} - \frac{\alpha}{5}\xi^2 + \frac{\alpha-1}{7}\xi^4\right). & (2.23) \end{aligned}$$

2.3.1 Choice of α

Before deriving the improved expression for ν and p, let us see how we can express α in terms of M, R and ρ_c. One way to determine this is to use $M = m_{\rm imp}(R)$, which yields

$$\alpha = \frac{5(-21M + 16\pi R^3\rho_c)}{24\pi R^3\rho_c}. \tag{2.24}$$

However, we find that a more accurate modeling is obtained by fitting Eq. (2.21) to the true density profile obtained numerically for various EoSs and ρ_c. We adopt eleven realistic EoSs with different stiffness, as summarized in Table 2.1. These EoSs all support a $2M_\odot$ NS [60]. We consider fits for α in terms of M, R and ρ_c given by

$$\alpha = a_0 + a_1\left(\frac{\mathcal{C}^n}{\rho_c R^2}\right) + a_2\left(\frac{\mathcal{C}^n}{\rho_c R^2}\right)^2, \tag{2.25}$$

where $\mathcal{C} = M/R$ and the fitted coefficients a_0, a_1, a_2 and n for each EoS are summarized in Table 2.2.

Such EoS-specific fits for α are useful only if one wishes to model the NS interior solution accurately for the EoSs presented in Table 2.2, and perhaps it would be more useful if we have a single, universal fit for α that is valid for any EoSs. The top panel of Fig. 2.2 shows α against $\mathcal{C}^n/\rho_c R^2$ with $n = 0.903$ for various EoSs. Indeed, the relation seems to be universal in the sense that it is insensitive to the choice of EoS. Based on this finding, we created a single fit, again using Eq. (2.25), that is valid for all 11 EoSs considered here. The fitting coefficients are summarized in Table 2.2.

The bottom panel of Fig. 2.2 presents the fractional difference between each data point and the universal fit. Observe that the fit is valid to 10% accuracy for any EoSs. Note that as one increases the central density, each sequence reaches a maximum value for $\mathcal{C}^n/\rho_c R^2$ and starts to turn around. This leads to the fact that the fractional difference from the fit being larger for larger $\mathcal{C}^n/\rho_c R^2$. In such a region, there can be two different values for α for a fixed $\mathcal{C}^n/\rho_c R^2$ (again due to the turn-over), and thus it becomes more difficult to fit the relation.

2.3.2 Improved Analytic Expressions for ν and p

Next, we look for the expressions for ν and p. The price we have to pay for adding the additional term in Eq. (2.21) is that we are no longer able to solve Eq. (2.3) analytically. Thus, we find an approximate solution instead.

Let us first derive the improved expression for ν. We begin by approximating λ in

EoS class	Members
soft	AP4 [170], SLy [171], WFF1 [172], WFF2 [172]
intermediate	ENG [173], MPA1 [174], AP3 [170], LS [175]
stiff	Shen [176], MS1 [177], MS1b [177]

Table 2.1: Eleven realistic EoSs considered in this work. They are categorized into three different stiffness classes [178].

Eq. (2.3) with the original Tolman VII expression λ_{Tol} and not the improved version λ_{imp}. The solution for ν to this equation then has the same form as Eqs. (2.15) and (2.16):

$$e^{\nu_{\text{imp}}(r)} = C_1^{\text{imp}} \cos^2 \phi_{\text{imp}}, \tag{2.26}$$

with

$$\phi_{\text{imp}} = C_2^{\text{imp}} - \frac{1}{2} \log \left(\xi^2 - \frac{5}{6} + \sqrt{\frac{5e^{-\lambda_{\text{Tol}}}}{8\pi R^2 \rho_c}} \right). \tag{2.27}$$

Though the integration constants C_1^{imp} and C_2^{imp} are different from the original ones C_1^{Tol} and C_2^{Tol} as we improve the boundary conditions:

$$e^{\nu_{\text{imp}}(R)} = 1 - \frac{2M}{R}, \qquad \bar{p}_{\text{imp}}(R) = 0\,. \tag{2.28}$$

These yield

$$C_1^{\text{imp}} = (1 - 2\mathcal{C}) \left\{ 1 + \frac{8\pi R^2 \rho_c (10 - 3\alpha)^2 (15 - 16\pi R^2 \rho_c)}{3[105 + 16\pi R^2 \rho_c (3\alpha - 10)]^2} \right\} \tag{2.29}$$

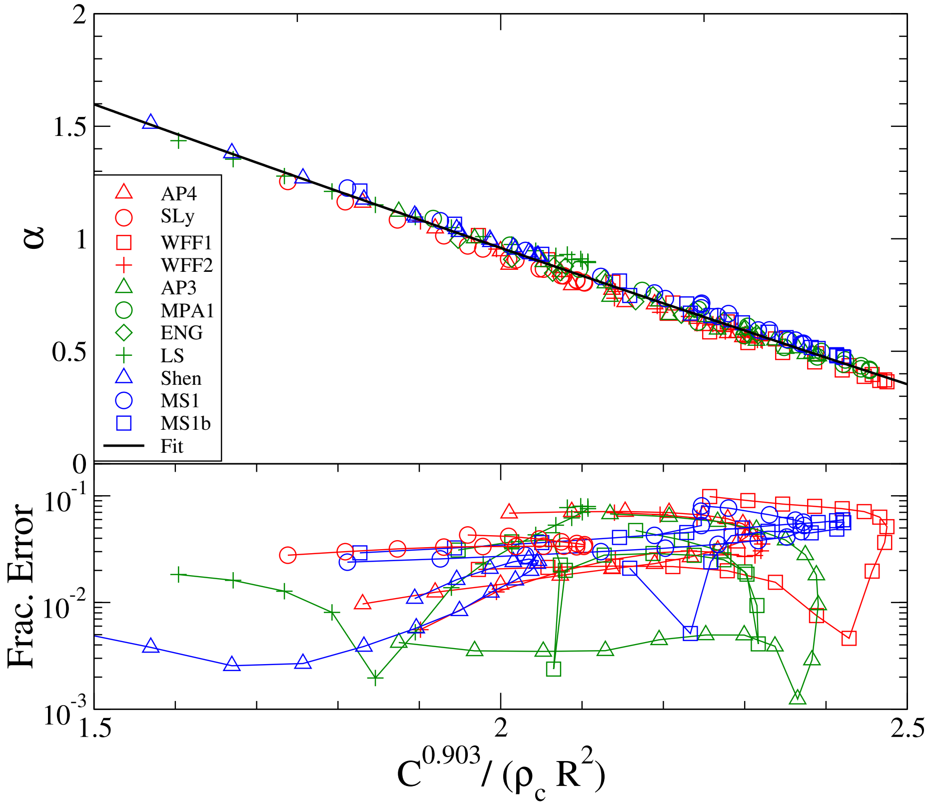

Figure 2.2: (Top) α (characterizing the density profile in the improved Tolman model in Eq. (2.21)) as a function of $C^n/\rho_c R^2$ with $n = 0.903$ for 11 realistic EoSs. Different colors correspond to different classes of EoSs in Table 2.1 (soft in red, intermediate in green and stiff in blue). We also present the fit in a black solid curve given by Eq. (2.25) with the coefficients given in the last row of Table 2.2. (Bottom) Relative fractional errors between numerical results and the fit. Notice that the relations are nearly EoS independent, with an EoS-variation of 10% at most.

$$\begin{aligned} C_2^{\rm imp} &= \arctan\left[-\frac{2(10-3\alpha)R\sqrt{6\pi\rho_c\,(15-16\pi\rho_c R^2)}}{48\pi(10-3\alpha)\rho_c R^2-315}\right], \\ &\quad +\frac{1}{2}\log\left(\frac{1}{6}+\sqrt{\frac{5}{8\pi\rho_c R^2}-\frac{2}{3}}\right). \end{aligned} \tag{2.30}$$

Next, we derive the improved expression for p. Using Eq. (2.4), the pressure for the improved model is given by

$$\bar{p}_{\rm imp} = \frac{1}{8\pi}\left[e^{-\lambda_{\rm imp}}\left(\frac{\nu'_{\rm imp}}{r}+\frac{1}{r^2}\right)-\frac{1}{r^2}\right]. \tag{2.31}$$

EoS	a_0	a_1	a_2	n	R-squared
AP4	3.90061	-1.67716	0.112974	0.884655	1.000000
SLy	4.08125	-1.94944	0.190047	0.898685	1.000000
WFF1	3.49902	-1.24206	0.01264	0.871133	0.999996
WFF2	5.00228	-2.70395	0.347978	0.88916	0.999998
AP3	3.99892	-1.75538	0.133497	0.881961	1.000000
MPA1	3.84739	-1.58061	0.0919565	0.879148	0.999999
ENG	0.438372	1.28922	-0.506597	0.874422	0.999733
LS	4.18945	-2.20875	0.288819	0.920735	1.000000
Shen	4.05847	-1.92481	0.187936	0.906579	0.999998
MS1	3.74656	-1.51608	0.0612786	0.911464	0.999909
MS1b	3.95158	-1.69133	0.114453	0.891669	0.999914
universal	3.70625	-1.50266	0.0643875	0.903	0.998772

Table 2.2: Fitted coefficients of α in Eq. (2.25) for each realistic EoS. We also present a universal fit for α that is valid for all the realistic EoSs considered here, within an error of 10%. The last column shows the R-squared value that gives a statistical measure of how good the fit is. It is the coefficient of determination defined by $\mathrm{R}^2 \equiv 1 - \frac{\sum_i (\alpha_i - \bar{\alpha})^2}{\sum_i (\alpha_i - f_i)^2}$, in which α_i represents the numerical data, f_i is the predicted value from the model and $\bar{\alpha}$ is the mean of the numerical data.

However, we found that Eq. (2.31) gives the central pressure that is $\sim 20\%$ off from numerical results. Moreover, the pressure becomes negative near the surface, which is unphysical. These points can be remedied by changing λ_{imp} to λ_{Tol} in Eq. (2.31) and shifting the overall profile by a constant such that the pressure reduces to 0 at the surface:

$$\begin{aligned} p_{\mathrm{imp}} &= \frac{1}{8\pi}\left[e^{-\lambda_{\mathrm{Tol}}(r)}\left(\frac{\nu'_{\mathrm{imp}}(r)}{r} + \frac{1}{r^2}\right) - \frac{1}{r^2}\right] \\ &\quad - \frac{1}{8\pi}\left[e^{-\lambda_{\mathrm{Tol}}(R)}\left(\frac{\nu'_{\mathrm{imp}}(R)}{R} + \frac{1}{R^2}\right) - \frac{1}{R^2}\right] \end{aligned}$$

$$\begin{aligned} = & \sqrt{\frac{e^{-\lambda_{\text{Tol}}}\rho_c}{10\pi}}\frac{\tan\phi_{\text{imp}}}{R} + \frac{1}{15}\left(3\xi^2 - 5\right)\rho_c \\ & + \frac{6(1-\alpha)\rho_c}{16\pi(10-3\alpha)\rho_c R^2 - 105}. \end{aligned} \tag{2.32}$$

We note that the set $(\rho_{\text{imp}}, m_{\text{imp}}, \nu_{\text{imp}}, p_{\text{imp}})$ is only an approximate solution to the Einstein equations. Having said this, $(\rho_{\text{Tol}}, m_{\text{Tol}}, \nu_{\text{imp}}, p_{\text{imp}})$ forms an exact solution to the Einstein equations, just like $(\rho_{\text{Tol}}, m_{\text{Tol}}, \nu_{\text{Tol}}, p_{\text{Tol}})$. The difference between these two sets of exact solutions originates simply from different boundary conditions. The former uses Eq. (2.28) while the latter adopts Eq. (2.17).

2.4 Comparison between the original and improved Tolman models

Let us next compare the original and improved Tolman models against numerical results. We first study the radial profiles of various quantities for a fixed mass and EoS. We then consider root-mean-square errors (RMSEs) for various masses and EoSs.

2.4.1 Radial Profiles

We begin by considering radial profiles similar to Fig. 2.1. Top panels of Fig. 2.3 present the ρ, m, ν and p profiles of a $1.4M_\odot$ NS with the AP4 EoS for two different Tolman solutions and the improved model, together with the numerical results. Here, we use the universal fit for α. The bottom panels show the fractional error of each analytic model from the numerical profiles.

Observe how the new model generally improves the original solution. For example, the ρ and m profiles of the improved model more accurately describe the numerical results over the original Tolman solution. Indeed, the former can fit the realistic profiles within an error of $\sim 5\%$ in most regions of the star. On the other hand, the ν and p profiles of the improved model are comparable to the original one, though the former is still better than the latter near the stellar center. Both the original and new solutions can model the realistic profiles within an error of $\sim 1\%$ ($\sim 10\%$) for the ν (p) profiles.

2.4.2 Root Mean Square Errors

The results presented in the previous subsection were specific to one example NS. How do they change with different masses and EoSs? To address this question, we introduce a relative RMSE, which is a measure of the error of the analytic model from the numerical results throughout the star:

$$(\text{relative RMSE}) = \sqrt{\frac{\int_0^R \left[y_{\text{num}}(r) - y_{\text{model}}(r)\right]^2 \mathrm{d}r}{\int_0^R y_{\text{num}}^2(r)\mathrm{d}r}}\,, \tag{2.33}$$

with $y = (\rho, m, \nu, p)$.

Figure 2.4 presents the relative RMSE for ρ, m, ν and p against the NS mass. We show the relative RMSEs for the 11 EoSs in terms of three models (the original Tolman solution parameterized by (R, M), the improved Tolman models with the universal α and with the EoS-specific α). Observe that in most cases, the improved models have a clear improvement over the original one in terms of accurately describing realistic profiles. This is more significant for soft EoSs (that are more preferred from

GW170817), as in the case of the AP4 EoS, where the accuracy improves up to a factor of ~ 5 for ρ and m.

To compare the new models against the original one more directly, we show in Fig. 2.5 the ratio between the difference and sum of the relative RMSEs for the improved (with the universal α) and original Tolman models. The new model more accurately describes numerical profiles than the original one if the ratio is *negative*. Notice first that the energy density profile can be better modeled by the new approximate solution for all EoSs and masses considered here. The situation is similar for the interior mass profile, except for the LS and Shen EoSs. Regarding the gravitational potential (ν) and pressure profiles, the new model performs better, especially for soft EoSs with NS masses larger than $1.5M_\odot$.

The accuracy of the new model can be improved further by adopting the EoS-specific fit for α, as can be seen from Fig. 2.6. In this case, the m and ν profiles for the new model are always better than the original ones, with exception only for high-mass (above $\sim 1.8M_\odot$) NSs with a few EoSs. The p profile has been improved also, though there are some mass ranges (very low mass around 1–$1.2M_\odot$ and very high mass above $1.8M_\odot$) where the original Tolman model performs better. Having said this, the accuracy of the new model is higher than the original one, even for the pressure profile in most of the EoSs and the mass range.

2.5 Conclusion

In this work, we explore a method to improve the accuracy of the original Tolman VII solution in modeling numerical solutions. We modified the original expressions by introducing a higher-order term in the density profile. We also succeeded in representing the additionally introduced parameter α in terms of M, R, and ρ_c in an EoS-insensitive way. The accuracy can be further improved if one uses an EoS-specific fit for α. We summarize the expressions for the new model in Table 1.1.

By comparing our results with the numerically solved solutions for 11 different EoSs, we showed that our improved model agrees better with the numerical results than the original Tolman solution. The relative RMSEs for the improved (original) Tolman solution are roughly 10% (20%) for energy density, 4% (10%) for the interior mass, 2% (10%) for the gravitational potential and 10% (40%) for pressure. The improvement is significant, especially for softer EoSs that are more preferred from GW170817.

Future work includes improving the proposed model further. For example, one may come up with a more appropriate density profile that can correctly capture its behavior close to the stellar surface. One can also try to find different ways of finding approximate solutions to the Einstein equations that will improve the modeling. The model presented here does not apply to stellar solutions whose density does not vanish at the surface, such as quark stars and self-bound stars [179]. It would be interesting to construct analytic interior models appropriate for these kinds of stars. One could also try to improve other analytic solutions, such as the one found by Buchdahl [69,70] which was compared against realistic NS solutions in [42].

Yet, another possible avenue is to extend the analysis presented here to more realistic NSs with rotation or tidal deformation. The first thing one can try is to assume these effects are small and treat them as perturbations to the solution presented here. If one can construct such solutions analytically, one can extract global quantities like the stellar moment of inertia, tidal Love number, and quadrupole moment, among which universal I-Love-Q relations are known to exist [100, 180–182]. Such analytic study may help understand the origin of the universality. The next chapter will be devoted to exploring the universality between I, Love, and compactness with the analytic tool developed in this chapter.

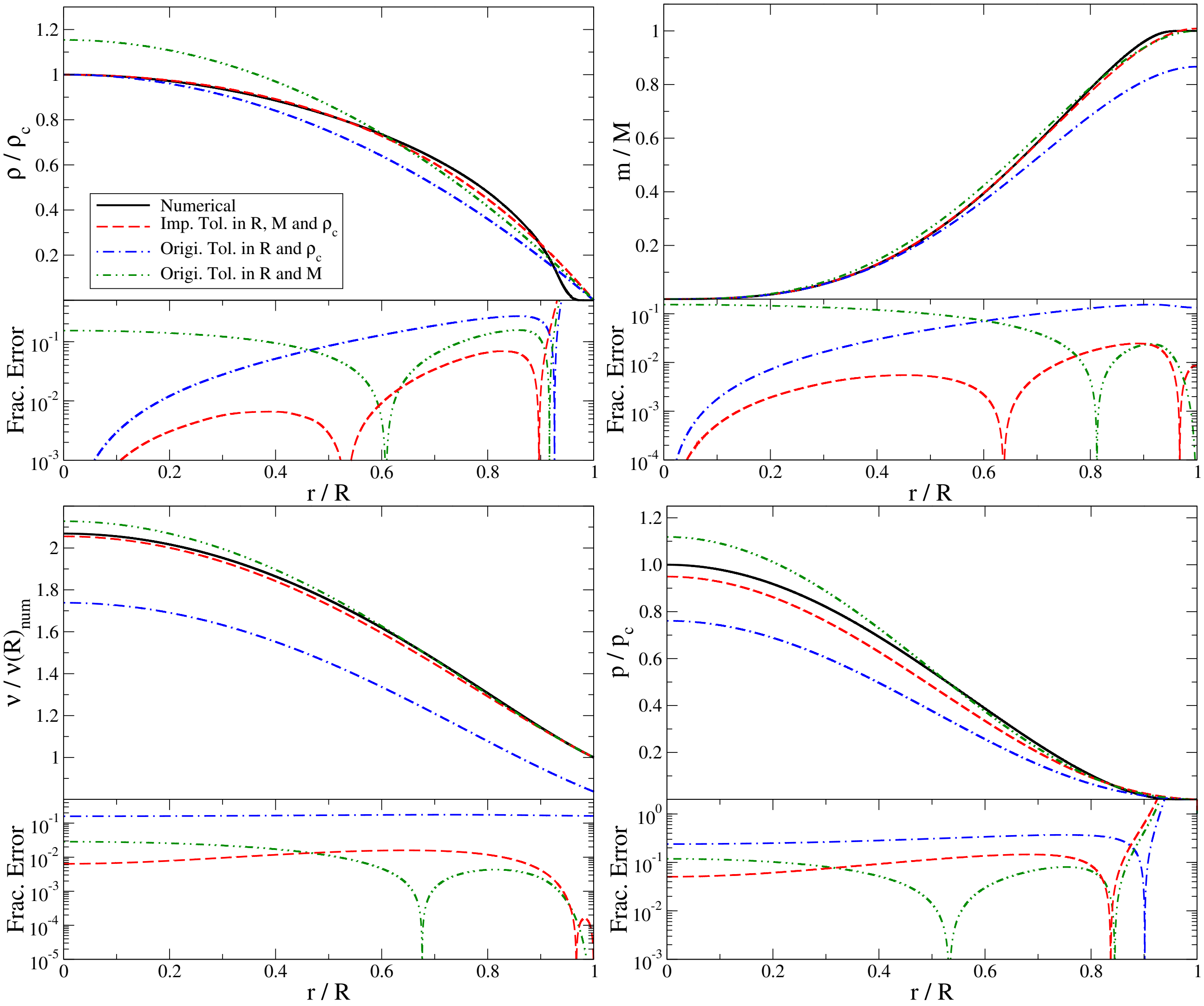

Figure 2.3: (Top) Profiles for energy density ρ using the universal fit for α (top left), interior mass m (top right), ν (related to the gravitational potential) (bottom left) and pressure p (bottom right) for the original Tolman VII solution in terms of (R, ρ_c) or (R, M) and the improved Tolman VII solution. The values of ρ_c, M and R are the same as those in Fig. 2.1. We also present the numerical result with the AP4 EoS and $M = 1.4 M_\odot$. (Bottom) Fractional errors from the profile obtained numerically. Observe that the new model works better than the original Tolman solution, especially for the ρ and m profiles.

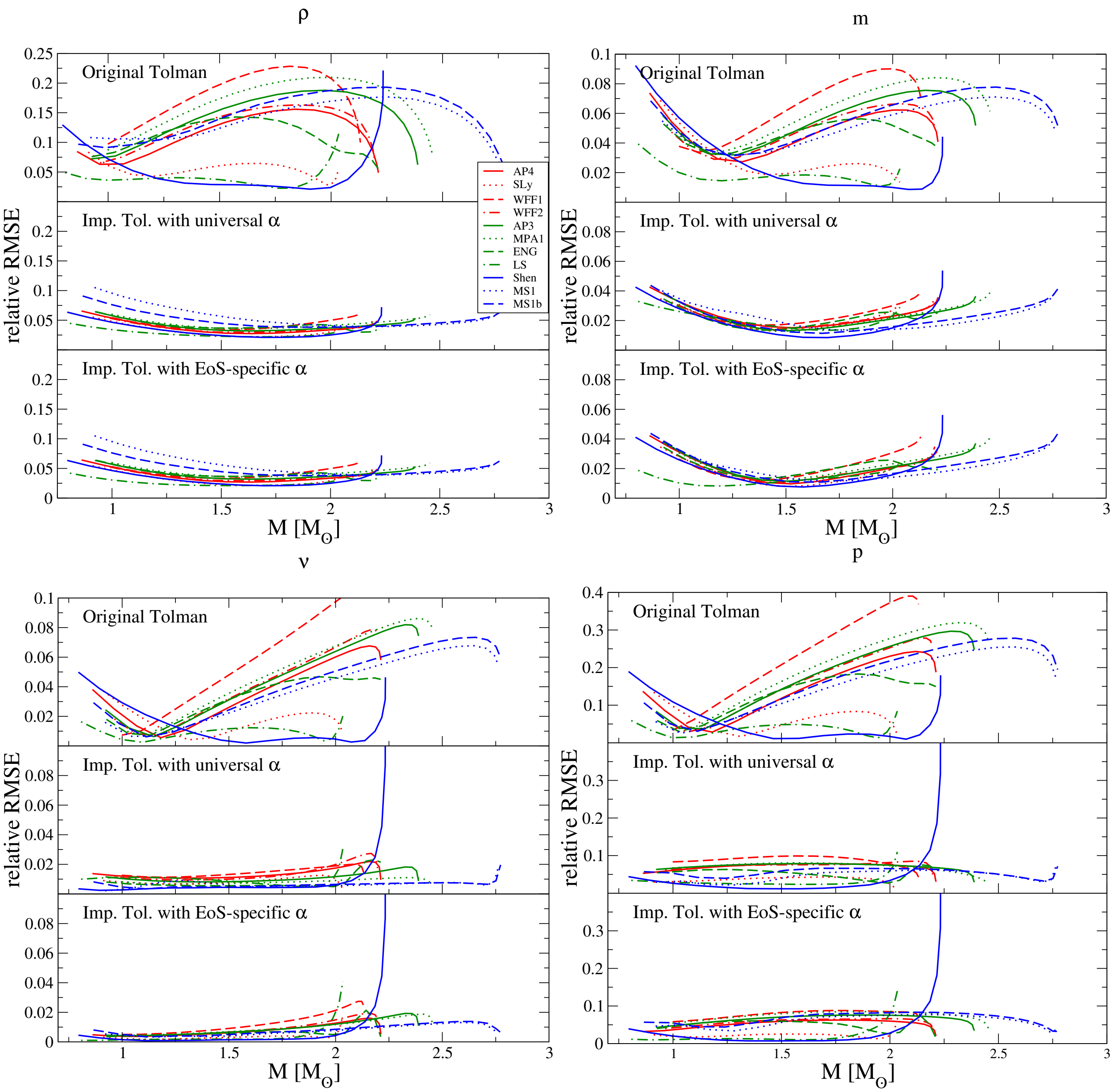

Figure 2.4: The relative RMSE (defined in Eq. (2.33)) of ρ (top left), m (top right), ν (bottom left) and p (bottom right) for the original Tolman solution with the (R, M) parameterization (top panel), the improved model with the universal α (middle panel) and the improved model with the EoS-specific α (bottom panel) as a function of the NS mass, using 11 EoSs with different stiffness in different colors as in Fig. 2.2. Observe how the improved models more accurately describe the realistic profiles (by having smaller relative RMSEs), especially for soft EoSs.

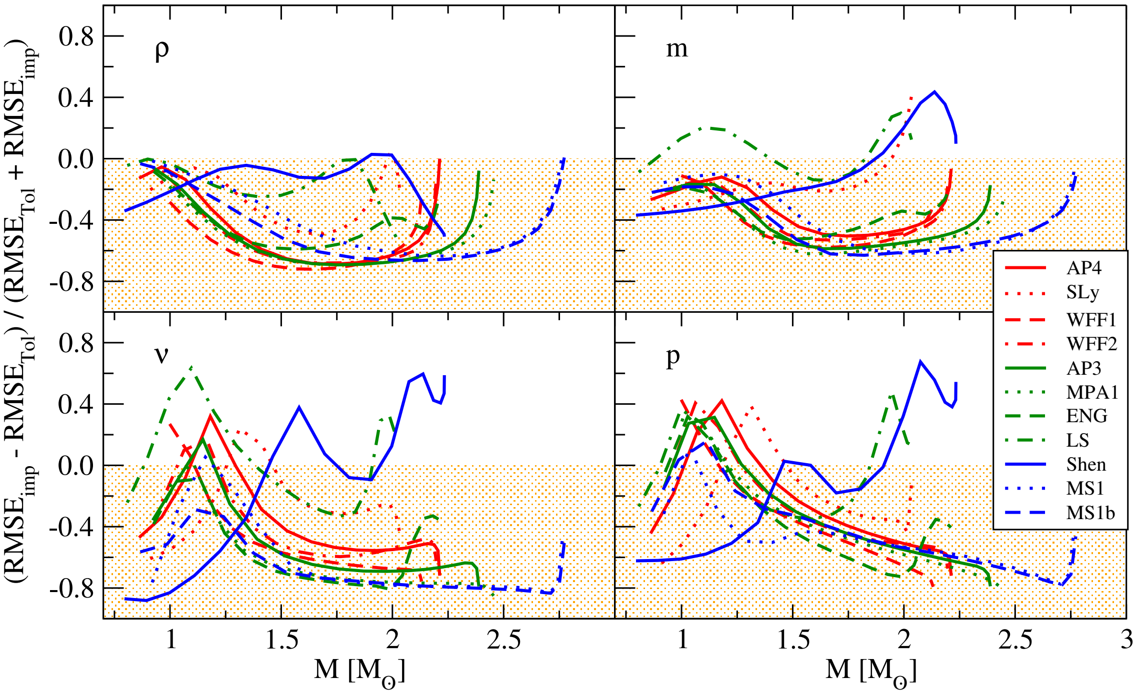

Figure 2.5: The normalized relative RMSE difference between the original Tolman solution and the improved model with the universal α. We show the results for ρ (top left), m (top right), ν (bottom left), and p (bottom right) using the 11 EoSs with different stiffness. The new model has an improvement over the original one if the normalized relative RMSE difference is *negative* (orange shaded region). Observe how the improved model more accurately describes the realistic profiles than the original Tolman solution in most cases.

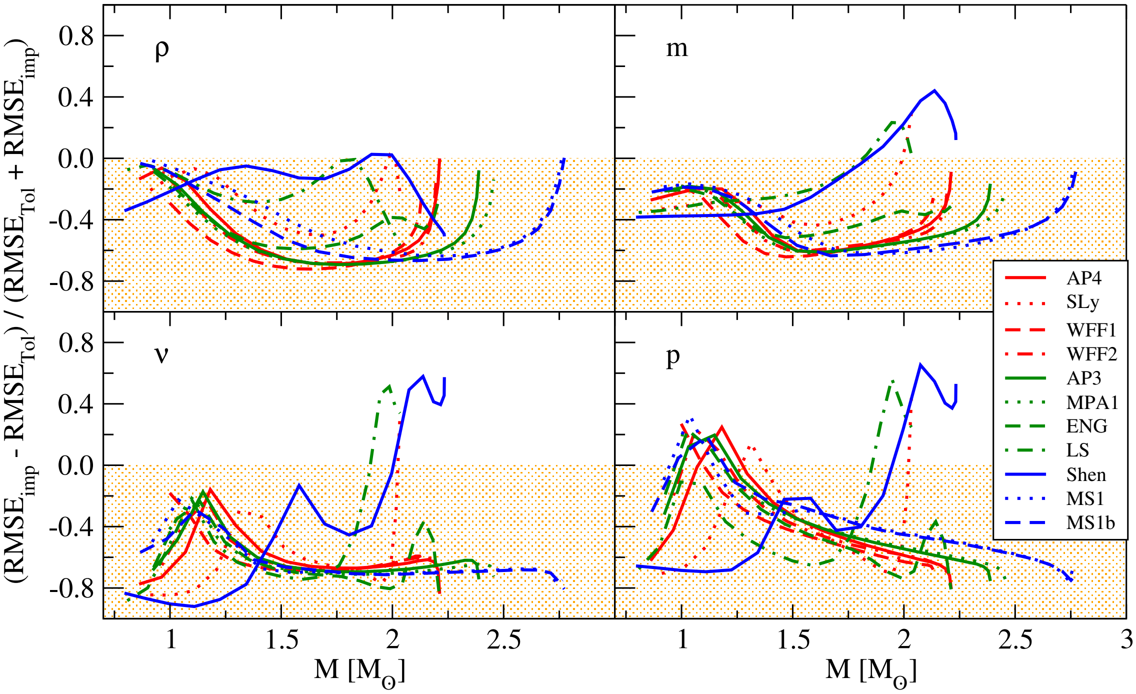

Figure 2.6: Similar to Fig. 2.5 but with the EoS-specific fit for α. Observe how the new model further improved from Fig. 2.5 by using such EoS-specific fit over the universal one.

Chapter 3

Analytic I-Love-C relations for realistic neutron stars

3.1 Introduction

Tolman VII solution [41, 71] is a useful, analytic model of non-rotating realistic NSs. This is a two-parameter (mass and radius) solution to the Einstein equations, in which the energy density profile inside a star is approximated by a quadratic function in a radial coordinate. In [162], we improved this model further by extending the energy density profile to a quartic function. We introduced a phenomenological parameter α to more accurately capture the realistic energy density profiles. We found that this modified Tolman VII model has improved accuracy for describing the metric and pressure or energy density functions over the original Tolman VII solution by a factor of 2–5.

In this chapter, we construct analytic, I-Love-C relations for realistic NSs by extending non-rotating solutions for the modified Tolman VII model to slowly rotating or tidally-deformed configurations, which allows us to extract the moment of inertia and tidal deformability. We treat the rotation or tidal deformation to be a small perturbation and keep only to leading order in such a perturbation. This is a good approximation since e.g. the rotation of the primary pulsar in the double pulsar binary is much smaller than the break-up rotation. Following [1], we find a series-expanded solution for the moment of inertia and the tidal deformability in terms of compactness. We then eliminate the compactness to find the I-Love relation for the modified Tolman VII model applicable to realistic NSs. Varying the phenomenological parameter α within a reasonable range for realistic NSs allows us to analytically estimate the amount of the universality in the I-Love-C relations.

The organization of the rest of the chapter is as follows. In Sec. 3.2, we briefly introduce what original and modified Tolman VII solutions are. In Secs. 3.3 and 3.4, we describe how we construct the analytic I-C and Love-C relations, respectively, and compare them against numerical relations for realistic NSs and analytic relations for constant-density stars. We also analytically estimate the amount of universality in these relations. In Sec. 3.5, we present the results of the semi-analytic I-Love relation. In Sec. 3.6, we use our analytic findings to present a possible origin of the universality for the I-C and Love-C relations. In Sec. 3.7, we conclude and give possible directions for future work.

3.2 Modified Tolman VII solution

Here, we briefly review the original Tolman VII [71] and modified Tolman VII [162] solution of a static, isolated, and spherically symmetric NS in the interior region. The related expressions given in Chap. 2 are repeatedly presented in this chapter for a more consistent and smooth flow of delivery of derivation.

In the original Tolman VII solution [71], the energy density profile is given by

$$\rho_{\mathrm{Tol}}(\xi) = \rho_c(1-\xi^2). \tag{3.1}$$

Modified Tolman VII model [162] introduces an additional term to Eq. (3.1) with a free parameter α in order to capture the variation in the energy density profile among different EoSs:

$$\rho_{\mathrm{mod}}(\xi) = \rho_c\left[1-\alpha\xi^2+(\alpha-1)\xi^4\right]. \tag{3.2}$$

Figure 3.1 presents α obtained by fitting a numerical energy density profile with Eq. (3.2) for various EoSs[1] and compactness. Observe that α ranges in $\alpha \in$[0.4,1.4] when $\mathcal{C} \in$[0.05,0.35]. We will vary α within this range in later calculations.

The remaining equations modified from the original Tolman VII one are as follows.

$$m_{\mathrm{mod}}(\xi) = 4\pi\rho_c R^3\xi^3\left(\frac{1}{3}-\frac{\alpha}{5}\xi^2+\frac{\alpha-1}{7}\xi^4\right), \tag{3.3}$$

$$e^{-\lambda_{\mathrm{mod}}(\xi)} = 1-8\pi R^2\xi^2\rho_c\left(\frac{1}{3}-\frac{\alpha}{5}\xi^2+\frac{\alpha-1}{7}\xi^4\right), \tag{3.4}$$

with the subscript "mod" representing the quantities in the modified Tolman solution. The expressions for ν and p are then adjusted to be

---

[1] The 11 EoSs considered here are the same as those in [162], which all support NSs with their mass above $2M_\odot$.

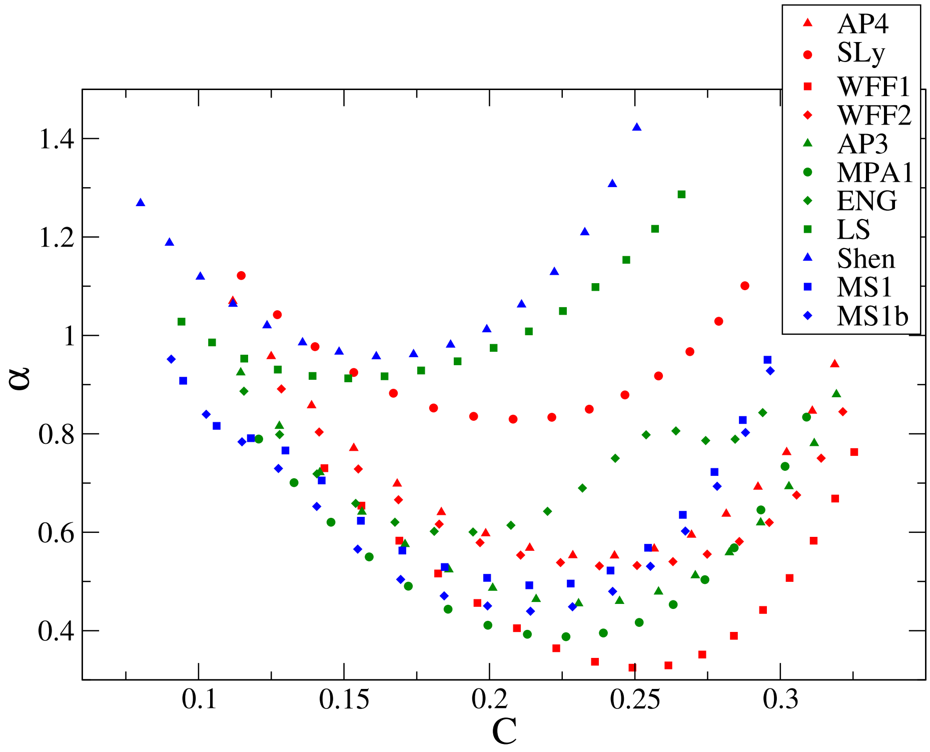

Figure 3.1: The parameter α introduced in the density profile of the modified Tolman VII model (Eq. (3.2)) against the compactness $\mathcal{C}$ for 11 realistic EoSs. The red, green, and blue dots represent soft, intermediate, and stiff EoSs respectively.

$$\begin{aligned} e^{\nu_{\rm mod}(\xi)} &= C_1^{\rm mod} \cos^2 \phi_{\rm mod}, \qquad (3.5) \\ p_{\rm mod}(\xi) &= \sqrt{\frac{e^{-\lambda_{\rm Tol}}\rho_c}{10\pi}} \frac{\tan \phi_{\rm mod}}{R} + \frac{1}{15}\left(3\xi^2 - 5\right)\rho_c + \frac{6(1-\alpha)\rho_c}{16\pi(10-3\alpha)\rho_c R^2 - 105}, \qquad (3.6) \end{aligned}$$

with

$$\begin{aligned} \phi_{\rm mod}(\xi) &= C_2^{\rm mod} - \frac{1}{2}\log\left(\xi^2 - \frac{5}{6} + \sqrt{\frac{5e^{-\lambda_{\rm Tol}}}{8\pi R^2 \rho_c}}\right), \qquad (3.7) \\ C_1^{\rm mod} &= (1-2\mathcal{C})\left\{1 + \frac{8\pi R^2 \rho_c (10-3\alpha)^2 (15 - 16\pi R^2 \rho_c)}{3[105 + 16\pi R^2 \rho_c (3\alpha - 10)]^2}\right\}, \qquad (3.8) \\ C_2^{\rm mod} &= \arctan\left[-\frac{2(10-3\alpha)R\sqrt{6\pi\rho_c}\,(15 - 16\pi\rho_c R^2)}{48\pi(10-3\alpha)\rho_c R^2 - 315}\right] + \frac{1}{2}\log\left(\frac{1}{6} + \sqrt{\frac{5}{8\pi\rho_c R^2} - \frac{2}{3}}\right) \\ &. \qquad (3.9) \end{aligned}$$

Notice that the above solution is parameterized by ($\mathcal{C}, R, \rho_c$ and α). We can further eliminate ρ_c from the condition $M = m_{\rm imp}(1)$, which yields

$$\rho_c = \frac{105\mathcal{C}}{8\pi R^2 (10 - 3\alpha)}. \qquad (3.10)$$

Using this in the modified Tolman VII expressions, we obtain a three-parameter $(\mathcal{C}, R, \alpha)$ (or equivalently (M, R, α)) model which will be used in the following calculations.

3.3 Moment of inertia

3.3.1 Formulation

One can extract the moment of inertia I from the asymptotic behavior of the time-spatial component of the metric at infinity for a slowly rotating NS. For simplicity, we consider uniform rotation. The metric ansatz is given by

$$ds^2 = ds_0^2 - 2\Omega(1-\omega)r^2 \sin^2\theta dt d\phi, \tag{3.11}$$

where ds_0^2 is the non-rotating part of the line element in Eq. (2.1), Ω is the constant stellar angular velocity and ω is a function of r (or ξ). Substituting this ansatz into the Einstein equations, one finds an equation for ω as [183]

$$\frac{d}{d\xi}\left(\xi^4 j \frac{d\omega}{d\xi}\right) + 4\xi^3 \frac{dj}{d\xi}\omega = 0, \tag{3.12}$$

with the boundary condition

$$\omega \mid_{\xi\to 0} = 1, \quad \left.\frac{d\omega}{d\xi}\right|_{\xi\to 0} = 0, \tag{3.13}$$

and $j(\xi) = e^{(-\lambda+\nu)/2}$.

Let us next look at the exterior solution. Integrating the equation in the exterior region (with $j(\xi) = 1$), one finds

$$\omega_{\mathrm{ext}}(r) = 1 - \frac{2I}{r^3}. \tag{3.14}$$

The closed form of I can be obtained easily from the differential equations and its boundary conditions above, which is [183]

$$I = \frac{8\pi R^5}{3} \int_0^1 \frac{\xi^5 (p+\rho) e^{-(\nu+\lambda)/2} \omega}{\xi - \frac{2m}{R}} d\xi. \tag{3.15}$$

3.3.2 Analytic Solutions

We now find an analytic solution to Eq. (3.12) for the modified Tolman VII solution. Unfortunately, we were not able to find an exact solution. Instead, we apply a post-Minkowskian recursive perturbation method adopted in Chan *et al.* [1] for incompressible stars to derive an approximate, analytic solution for ω and I.

We begin by defining

$$\tilde{\omega}(\xi) \equiv 1 - \omega(\xi), \tag{3.16}$$

and expanding $\tilde{\omega}(\xi)$ and $j(\xi)$ in power series of $\mathcal{C}$:

$$\tilde{\omega}(\xi, \mathcal{C}) \approx \sum_{n=0}^{N} \tilde{\omega}_n(\xi) \mathcal{C}^n, \quad j(\xi, \mathcal{C}) \approx \sum_{n=0}^{N} j_n(\xi) \mathcal{C}^n. \tag{3.17}$$

Here $\tilde{\omega}_n(\xi)$ and $j_n(\xi)$ are functions of ξ only while N corresponds to the order of the expansion that we keep. In the Newtonian limit ($\mathcal{C} \to 0$), one finds

$$j_0(\xi) = 1, \quad \tilde{\omega}_0(\xi) = 0. \tag{3.18}$$

Having the above series expansion at hand, we can solve the differential equation. Namely, we substitute Eq. (3.17) into Eq. (3.12) and solve the latter for $\tilde{\omega}_n$ order by order in powers of $\mathcal{C}$. We can then derive the series expansion of the dimensionless moment of inertia from Eq. (3.15) as

$$\bar{I} \equiv \frac{I}{M^3} \approx \sum_{n=0}^{N} \bar{I}_n \mathcal{C}^{n-2}. \tag{3.19}$$

The series starts with $\mathcal{C}^{-2}$ since $I \propto MR^2$ in the Newtonian limit. $\bar{I}$ is given in terms of $\tilde{\omega}$ as

$$\bar{I} = \frac{\tilde{\omega}_R}{2\mathcal{C}^3}, \quad \tilde{\omega}_R \equiv \tilde{\omega}(\xi = 1). \tag{3.20}$$

Figure 3.2 shows how the I-C series converges as one increases the order of expansion. Observe that the expansion to sixth order in compactness can accurately describe the numerical relation. Since the expressions for $\bar{I}_n$ are lengthy and not illuminating, we show them in a supplemental Mathematica notebook [161].

We present in the top panel of Fig. 3.3 the approximate, analytic I-C relation for the modified Tolman VII solution. For comparison, we also show the approximate, analytic relation for incompressible stars [1] and the relations for some representative realistic EoSs. Observe that the new analytic relation can beautifully approximate the numerical relation for the realistic EoSs. Observe also that the relation for incompressible stars found in [1] does not provide an accurate description for realistic NSs[2]. The new relation found in this chapter gives us the first analytic expression for the I-C relation for realistic NSs other than the fits in e.g. [99, 184, 185].

The bottom panel shows the fractional difference of the modified Tolman VII relation from the original one. Notice that when we vary α within the range for

---

[2] The relation for incompressible stars can accurately describe the relation for quark stars [99].

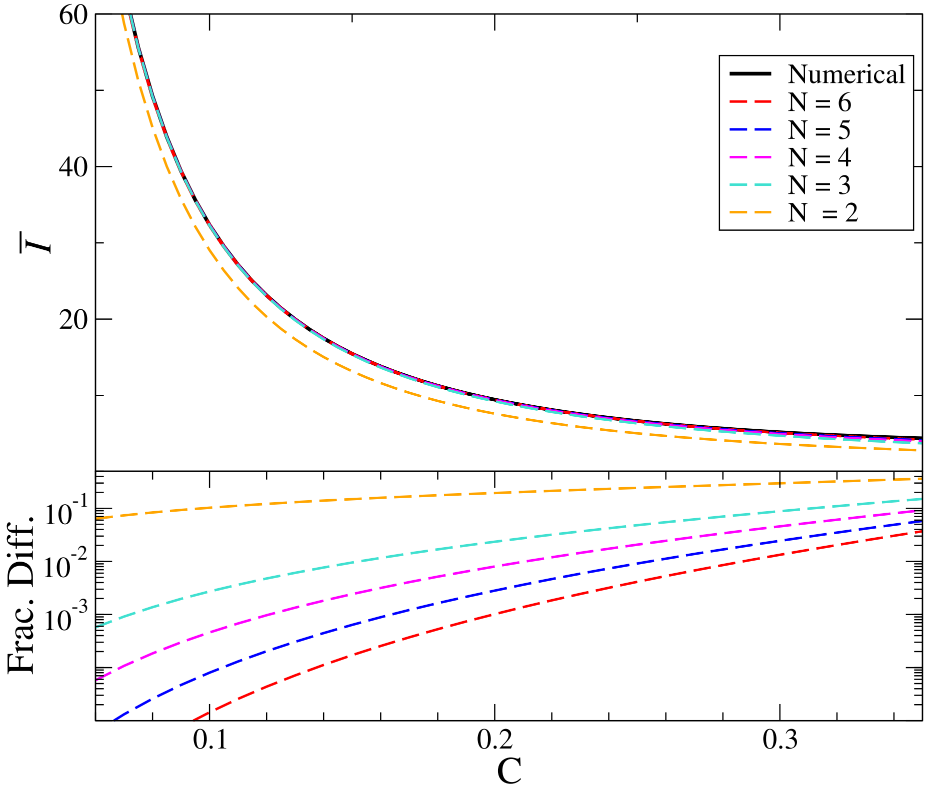

Figure 3.2: (Top) I-C relation for the original Tolman VII solution with different orders of series expansion in $\mathcal{C}$. (Bottom) Fractional differences between the curve obtained numerically and the analytic one at each expansion order. Observe that the analytic relation converges as we increase the order.

realistic EoSs, the analytic relation varies by $\sim 10\%$. This amount agrees with that of the EoS-variation in the relation for realistic NSs in the middle panel (see also [99]). Thus, the new relation provides us with an analytic explanation for the amount of universality in the I-C relation.

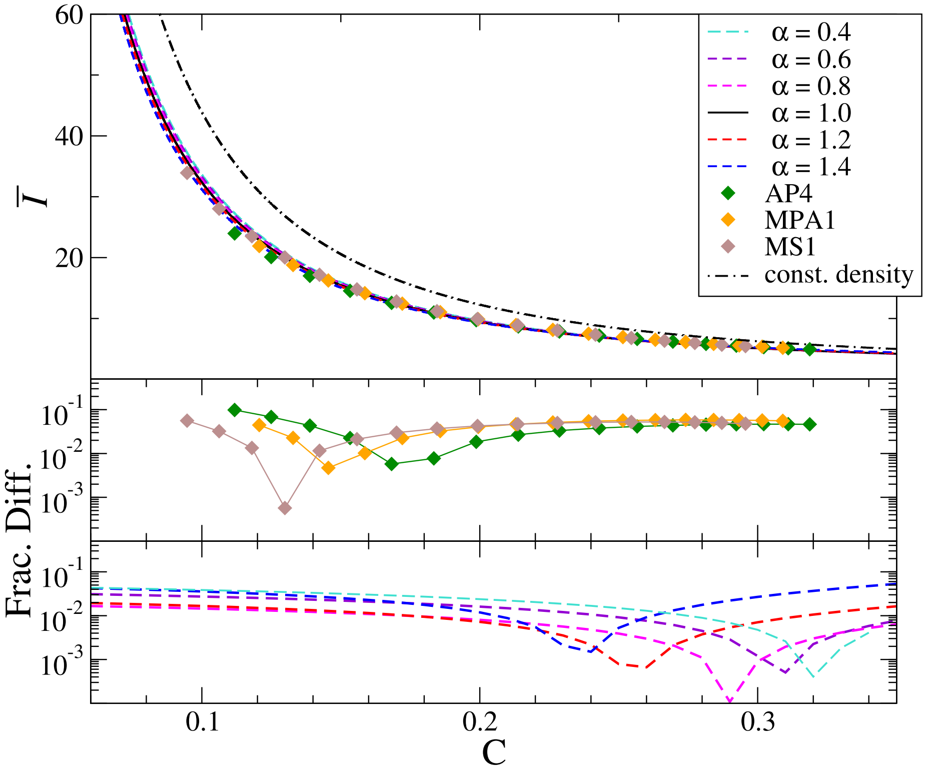

Figure 3.3: (Top) Approximate, analytic I-C relation (up to sixth order in the series expansion in $\mathcal{C}$) for the modified Tolman VII solution with five representative values of α. For comparison, we also show the numerical relation for three representative realistic EoSs, namely AP4 (soft), MPA1 (intermediate), and MS1 (stiff). The dotted-dashed line represents the relation for incompressible constant density stars in [1]. (Middle) Relative fractional difference of the I-C relation for the realistic EoSs from that for the original Tolman solution. (Bottom) Relative fractional difference for the modified Tolman VII relation from the original one. Observe that the EoS-variation is kept under 10% for both realistic EoSs and modified Tolman VII relations, in agreement with that for realistic EoSs in Fig. 15 of [99].

Let us investigate further the EoS-variation in the I-C relation using the new analytic I-C relation. Expanding $\bar{I}_n$ about $\alpha = 1$ (the original Tolman solution), we find

$$\begin{aligned}
\bar{I}_0 &= 0.286[1 - 0.105(\alpha - 1) + \mathcal{O}(\alpha - 1)^2] \\
\bar{I}_1 &= 0.323[1 - 0.100(\alpha - 1) + \mathcal{O}(\alpha - 1)^2] \\
\bar{I}_2 &= 0.462[1 + 0.258(\alpha - 1) + \mathcal{O}(\alpha - 1)^2] \\
\bar{I}_3 &= 0.732[1 + 0.403(\alpha - 1) + \mathcal{O}(\alpha - 1)^2] \\
\bar{I}_4 &= 1.226[1 + 0.545(\alpha - 1) + \mathcal{O}(\alpha - 1)^2] \\
\bar{I}_5 &= 2.132[1 + 0.688(\alpha - 1) + \mathcal{O}(\alpha - 1)^2].
\end{aligned}$$

This shows that the α dependence on the leading contribution to $\bar{I}$ ($\bar{I}_0$) is $\sim 10\%$ (because the relative coefficient is 0.105), and similar for $\bar{I}_1$. This analytically explains the origin of the $\mathcal{O}(10\%)$ EoS-variation in the relation. On the other hand, the α dependence becomes larger as we increase n in $\bar{I}_n$, though such contributions are higher order and do not affect the relation much.

3.4 Tidal Love number

3.4.1 Formulation

In this section, we present the calculation of the tidal deformability or the tidal Love number due to tidal deformation. For example, a primary NS in a binary acquires tidal deformation due to the tidal field created by a companion star. Such an effect is characterized by the dimensionless tidal deformability, which is defined as

$$\bar{\lambda} \equiv \frac{\lambda}{M^5} \equiv -\frac{Q}{M^5}\mathcal{E} = \frac{2}{3}k_2\mathcal{C}^{-5}. \tag{3.21}$$

Here Q and $\mathcal{E}$ are the tidally-induced quadruple moment and the external tidal field and k_2 is the tidal Love number defined by $k_2 \equiv (3/2)(\lambda/R^5)$. To calculate Q and $\mathcal{E}$, we follow the formulations and conventions established in [84]. We begin with the metric ansatz,

$$\begin{aligned} ds^2 &= ds_0^2 - [h_2(e^{\nu}dt^2 + e^{\lambda}dr^2) \\ &\quad -r^2 K_2(d\theta^2 + \sin^2\theta\ d\phi^2)]Y_{2m}(\theta,\phi), \end{aligned} \tag{3.22}$$

where $h_2(r)$ and $K_2(r)$ are quadrupolar tidal perturbations while $Y_{\ell m}$ are spherical harmonics. Substituting this into the Einstein equations, one can derive a second-order differential equation for h_2 as [84]

$$\begin{aligned} &\xi y' + y^2 + y e^{\lambda}[1 + 4\pi\xi^2 R^2(p-\rho)] \\ &-\left\{\frac{6e^{\lambda}}{\xi^2} - 4\pi e^{\lambda}R^2\left[5\rho + 9p + (\rho+p)\frac{d\rho}{dp}\right] + \nu'^2\right\}\xi^2 = 0, \end{aligned} \tag{3.23}$$

where

$$y \equiv \frac{\xi}{h_2}\frac{dh_2}{d\xi}, \tag{3.24}$$

and the prime represents a derivative with respect to ξ. The initial condition is given by $y(\xi=0)=2$. Solving the above equation, one can find $\bar{\lambda}$ using Eq. (3.21) as in

Eq. (1.2) with $y_R \equiv y(\xi = 1)$ [84, 186].

3.4.2 Analytic Solution

We now study analytic expressions for h_2 (or y) and the tidal deformability. Similar to the case of the moment of inertia, we were not able to solve Eq. (3.23) exactly for the modified Tolman VII model. Thus, we follow the same procedure as before and consider series expansion in $\mathcal{C}$.

We begin by expanding y as [1]

$$y(\xi, \mathcal{C}) \approx \sum_{n=0}^{N} y_n(\xi) \mathcal{C}^n, \tag{3.25}$$

where each coefficient y_n is a function of ξ only. Substituting this expansion into Eq. (3.23) and looking at order by order, one can derive differential equations for y_n. Unlike the case of the moment of inertia, we were not able to find analytic exact solutions to these equations for the modified Tolman VII model[3]. Thus, we further expand y_n about $\xi = 0$ as

$$y_n(\xi) \approx \sum_{k=1}^{K} y_n^{(2k)} \xi^{2k}, \tag{3.26}$$

where $y_n^{(2k)}$ is now a constant while K is the expansion order in terms of ξ. We expand Eq. (3.23) in powers of both $\mathcal{C}$ and ξ, find algebraic equations for $y_n^{(2k)}$ order by order, and solve them. We show $y_n(\xi)$ expanded up to 12th order in ξ ($K = 6$) in the supplemental Mathematica notebook [161].

Figure 3.4 compares the analytic relations between $\bar{\lambda}$ and $\mathcal{C}$ (the Love-C relations)

---

[3] For the original Tolman model, y_0 can be solved exactly in terms of hypergeometric functions, though the differential equation is too complicated to be solved for y_1 and higher.

for the original Tolman solution at different expansion order in $\mathcal{C}$ against the numerical relation. For the former, we fixed $K = 6$ for the ξ expansion. Unlike the I-C case in Fig. 3.2, the series does not converge. We found that the sound speed squared $(dp/d\rho)$ in Eq. (3.23) becomes inaccurate as one goes to higher order in $\mathcal{C}$. The analytic relation is given in series expansion in $\mathcal{C}$, thus the approximation becomes worse in a large $\mathcal{C}$ region. In this section, we keep up to 3rd order in $\mathcal{C}$ ($N = 3$ in Eq. (3.25)) and 12th order in ξ ($K = 6$ in Eq. (3.26)) that most accurately approximates the correct numerical relation. When deriving the I-Love relation, we will use the relation up to 6th order in $\mathcal{C}$ as we will explain in more detail in Sec. 3.5.

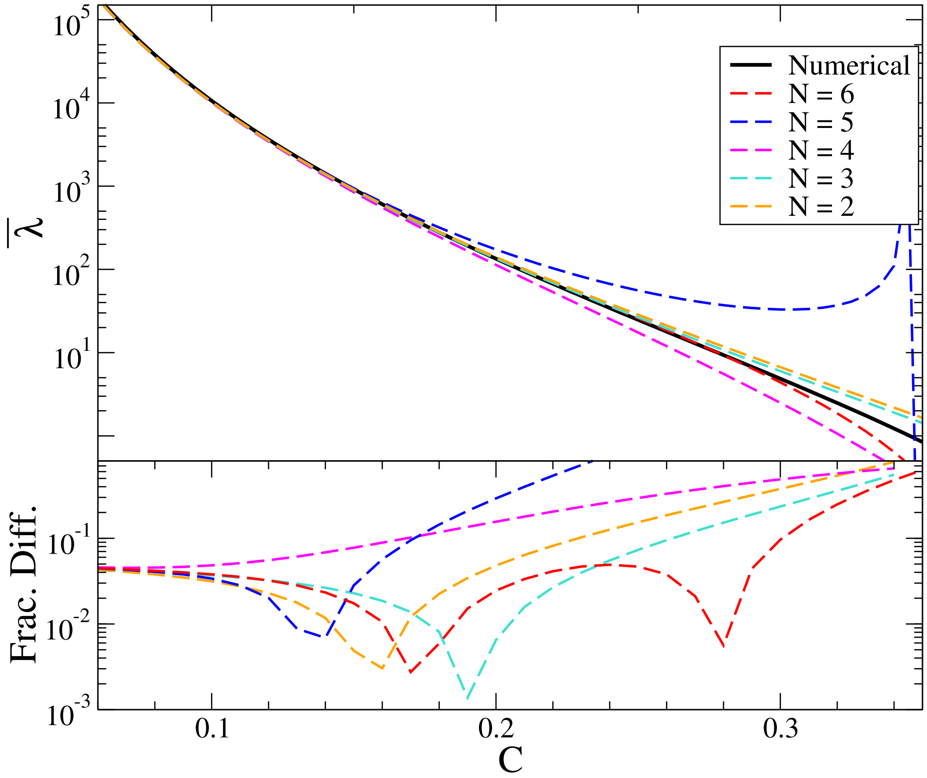

Figure 3.4: Similar to Fig. 3.2 but for the Love-C relation. Observe that the series does not converge in this case, and the third-order expansion gives the most accurate result.

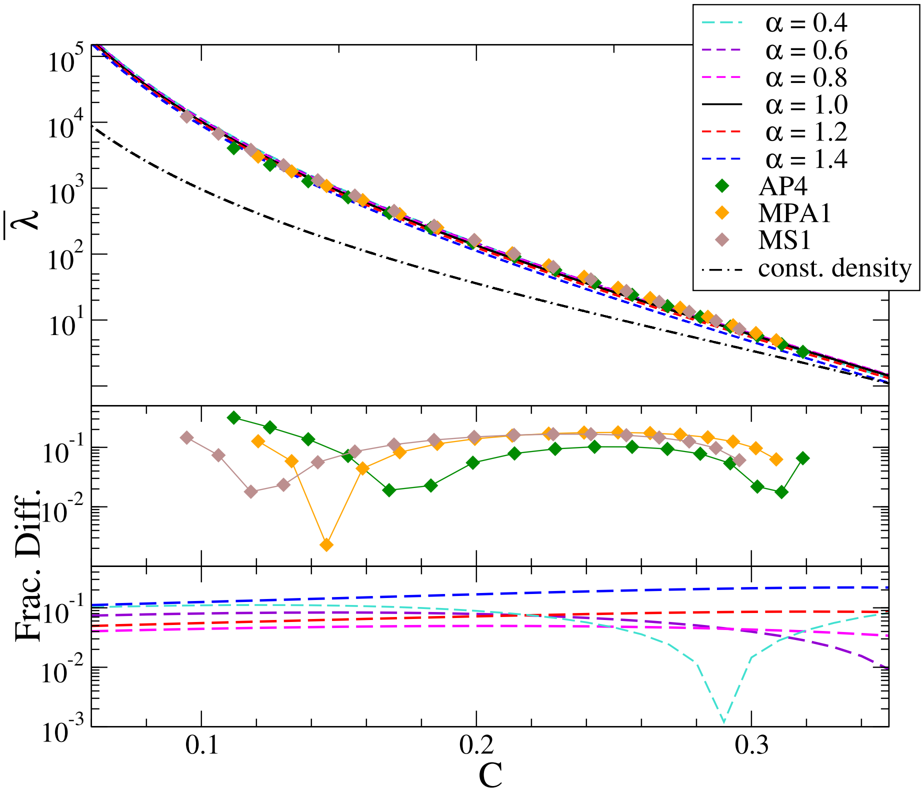

Figure 3.5: Similar to Fig. 3.3 but for the Love-C relation. The analytic relations for the modified Tolman model have been kept up to 3rd order in $\mathcal{C}$. Observe that the EoS-variation is kept under $\mathcal{O}(10\%)$ for both modified Tolman VII and realistic EoSs, in agreement with that for realistic EoSs in Fig. 15 of [99]

The top panel of Fig. 3.5 presents the analytic Love-C relations for the modified Tolman solution, together with those for the realistic EoSs and the one found in [1] for constant density stars. Observe that similar to Fig. 3.3, the analytic relation for the modified Tolman solution can accurately describe the results for the realistic EoSs while that for constant density stars fails to do so. The bottom panel shows the fractional difference in the Love-C relations between the modified and original Tolman solutions. Observe that the amount of the variation in α is of order 10%, consistent with the EoS-variation in the Love-C relation for realistic EoSs in the middle panel (see also [99]).

Similar to the I-C case, we can investigate further the amount of the α (or EoS) variation in the Love-C relation by expanding the analytic solution about the original Tolman solution. To achieve this, we first expand $\bar{\lambda}$ as

$$\bar{\lambda} \approx \sum_{n=0}^{N} \bar{\lambda}_n \mathcal{C}^{n-5}. \tag{3.27}$$

We then expand further each coefficient $\bar{\lambda}_n$ about $\alpha = 1$ and find

$$\bar{\lambda}_0 = 0.204[1 - 0.186(\alpha - 1) + \mathcal{O}(\alpha - 1)^2]$$

$$\bar{\lambda}_1 = -1.274[1 - 0.090(\alpha - 1) + \mathcal{O}(\alpha - 1)^2]$$

$$\bar{\lambda}_2 = 2.749[1 + 0.082(\alpha - 1) + \mathcal{O}(\alpha - 1)^2]$$

$$\bar{\lambda}_3 = -2.281[1 + 0.420(\alpha - 1) + \mathcal{O}(\alpha - 1)^2]$$

$$\bar{\lambda}_4 = 3.199[1 + 0.013(\alpha - 1) + \mathcal{O}(\alpha - 1)^2]$$

$$\bar{\lambda}_5 = -13.001[1 - 0.108(\alpha - 1) + \mathcal{O}(\alpha - 1)^2]$$

$$\bar{\lambda}_6 = 19.282[1 + 0.161(\alpha - 1) + \mathcal{O}(\alpha - 1)^2].$$

This expansion shows that the fractional α variation is only of order 10% or less for most of the coefficients, which again is consistent with the amount of EoS variation in the Love-C relation in Fig. 3.5. This gives us an analytic explanation for the amount of EoS variation in the relation.

3.5 I-Love Relation

Now that we have calculated the moment of inertia and tidal deformability, we can construct semi-analytic relations between these two quantities based on the modified Tolman VII solutions.

One can derive the I-Love relation ($\bar{I}$ as a function of $\bar{\lambda}$) semi-analytically based on the analytic I-C and Love-C relations by parametrically plotting $\bar{I}$ and $\bar{\lambda}$. Namely, we choose one $\mathcal{C}$ and plot a point in the I-Love plane using the above two analytic relations. We then change $\mathcal{C}$ and repeat the procedure to find the I-Love relation. This is semi-analytic in the sense that we are not providing a closed-form expression of $\bar{I}$ in terms of $\bar{\lambda}$.

Regarding the Love-C relation, we found that the expansion to sixth order in $\mathcal{C}$ gives us a more accurate semi-analytic I-Love relation than that with the 3rd-order expansion, which is counter-intuitive given that the 6th-order Love-C relation is less accurate than the 3rd-order one. This behavior arises because the amount of inaccuracy in the 6th-order Love-C relation partially cancels with that in the I-C relation, producing a more accurate I-Love relation. For this reason, we will use the sixth-order Love-C relation for constructing the I-Love relation.

The top panel of Fig. 3.6 presents such semi-analytic I-Love relations for the modified Tolman VII model. In most regimes, observe that the α-variation shown in the bottom panel is of $\mathcal{O}(1\%)$ at most. This reproduces the amount of the EoS-variation in the I-Love relations for realistic NSs shown in the middle panel and also found in [99, 101, 102]. The α variation becomes slightly larger when $\bar{I}$ and $\bar{\lambda}$ are smaller, though this is due to the fact that the sixth order Love-C relation becomes less accurate in the large $\mathcal{C}$ regime.

One can also obtain an approximate but completely analytic I-Love relation by first inverting the Love-C relation for $\mathcal{C}$ and substituting it to the I-C relation. For inverting the Love-C relation, one can find a series-expanded solution of the form

$$\mathcal{C} = \sum_{n=0} \frac{a_n}{\bar{\lambda}^{n/5}}, \tag{3.28}$$

with the coefficients a_n that is a function of α. The analytic I-Love relation obtained in this way, however, is not very accurate, at least up to the (sixth) order that we have worked on. We found that the variation in α can be $\mathcal{O}(10\%)$ or larger, and one may need to increase the order of the expansion to find a more accurate relation, which we leave for future work.

One can improve the semi-analytic model further by resumming the series-expanded

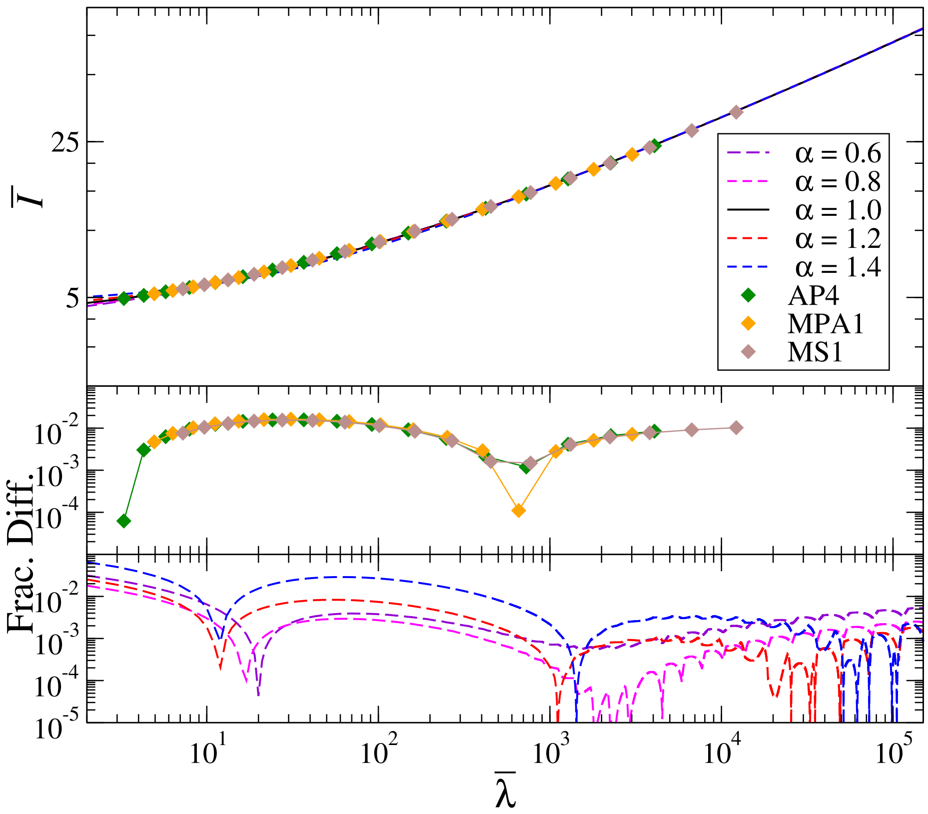

Figure 3.6: (Top) Similar to Fig. 3.3 but for the I-Love relation. The semi-analytic modified Tolman VII model is constructed by keeping the analytic I-C and Love-C relations up to 6th order in $\mathcal{C}$. Observe that the EoS-variation is kept around 1% for both realistic EoSs and the modified Tolman VII model.

I-C and Love-C (or the y_R expression to be more precise) relations using Padé approximant. Such Padé expressions for the modified Tolman solutions are lengthy and not very useful, while we managed to derive a simple form for the original Tolman solution. The results are given in Eqs. (1.1)–(1.3) in chapter 1, and the relations are show in Fig. 1.1. For the Padé resummation, we found that the 3rd order expansion of $y(\mathcal{C})$ provides a more accurate, semi-analytic I-Love relation (to be discussed in the next paragraph) than the 6th order expansion. This is why the Padé resummation is of order (3,3) for the I-C relation, while is of order (2,2) for the Love-C relation.

The top panel of Fig. 3.7 presents the semi-analytic I-Love relation for the original Tolman solution using the Padé expressions for the I-C and Love-C relations. For comparison, we also present the Padé-resummed relation for constant density stars [1] and realistic NSs using all 11 EoSs considered in Fig. 3.1. The middle (bottom) panel shows the relative fractional difference between the relation with each EoS and the constant-density (Padé-resummed original Tolman) model. Observe that the original Tolman relation always agrees with the realistic models within an error of 1% and gives a more accurate description than the constant density case, especially in the large compactness (small $\bar{\lambda}$) regime. Comparing the bottom panel of Fig. 3.7 with the middle panel of Fig. 3.6, one sees that the former slightly has a smaller fractional error, and thus the Padé resummed I-Love relation indeed proves us a more accurate result than the series-expanded one.

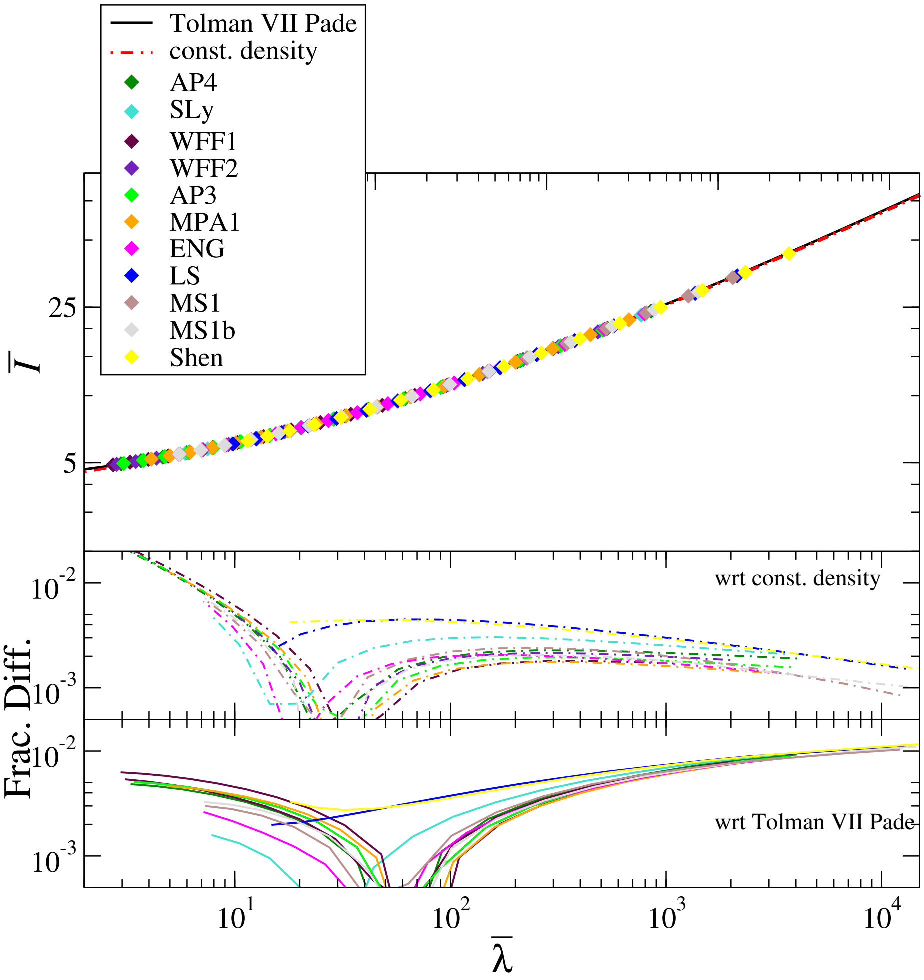

Figure 3.7: (Top) Semi-analytic, Padé-resummed I-Love relation for the original Tolman VII solution, together with the analytic relation for constant density stars [1] and numerical results for realistic EoSs. (Middle) The relative fractional difference of the relations for the realistic EoSs from the analytic one for constant density stars. (Bottom) Similar to the middle panel but for the Tolman VII relation. Observe that the Tolman VII model maintains universality with an EoS-variation of less than 1% for the whole range of $\bar{\lambda}$.

3.6 Possible origin of the universality

We now try to connect our analytic calculations to the possible origins of some of the universal relations. Regarding the I-Love-Q relations, Ref. [107] showed that the universality is related to approximate self-similarity of isodensity contours inside NSs, and this self-similarity becomes exact for constant-density stars. Similarly, Ref. [108] demonstrated that the origin of the universality can be attributed to the fact that realistic EoSs for NSs are "similar" to constant density EoSs, which is consistent with the findings in [107]. Unfortunately, these explanations do not apply to the I-C and Love-C relations, since NSs and constant density stars do not share the universality.

Here, we aim to obtain some insight into the possible origin of the I-C and Love-C universal relations based on our analytic calculations presented in the previous sections. The original Tolman VII solution is a two-parameter model characterized by the stellar mass and radius and, thus, can explain any mass-radius relations for NSs. Yet, we found that there are unique I-C and Love-C relations for the Tolman VII solution that agree well with those found numerically with realistic EoSs. The underlying assumption in the Tolman VII solution is that the energy density profile inside a star follows a quadratic function in the radial coordinate (Eq. (3.1)). All of this suggests that one can attribute the origin of the I-C and Love-C universality to the fact that the energy density profile for NSs roughly follows a quadratic function.

Figure 3.8 presents the energy density profiles for realistic NSs, together with realistic white dwarfs, Tolman VII quadratic model, and constant density stars. Observe

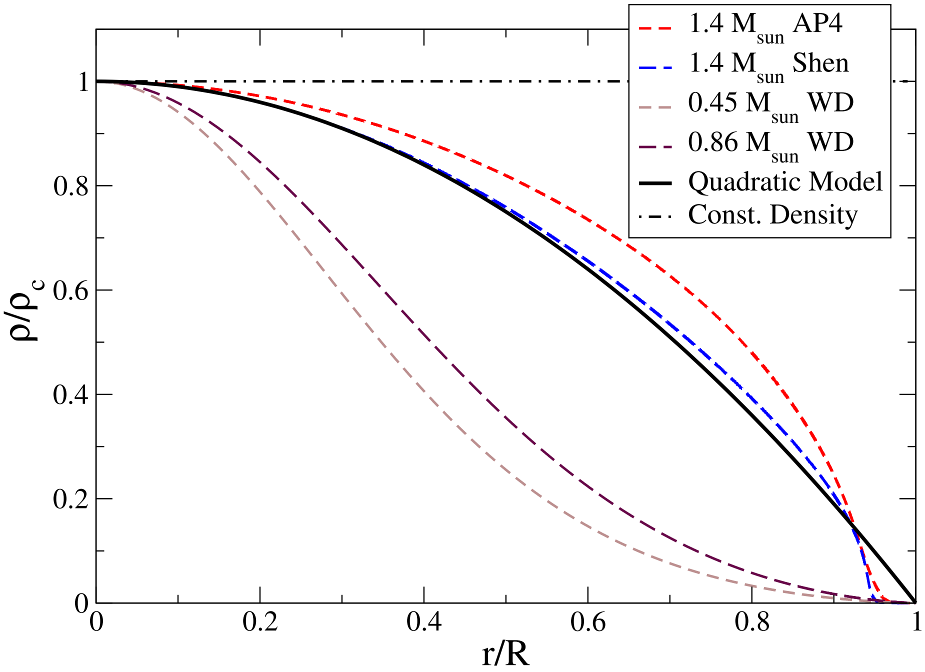

Figure 3.8: The normalized energy density profiles of NSs and white dwarfs, together with quadratic (original Tolman VII solution) and constant density models. The fact that realistic NS profiles approximately follow the quadratic function in Eq. (3.1) (whereas constant density stars and white dwarfs do not) can be interpreted as a possible origin of the I-C and Love-C universality.

that the NS profiles can be approximated well with the quadratic model, while white dwarfs and constant-density stars have different profiles. Universal relations for white dwarfs have been studied, e.g. in [187–189], which showed that they were quite different from the NS ones. The modified Tolman VII model that we also considered in this work accounts for the difference between the realistic NS profile and the quadratic one. As shown in the previous sections, we managed to recover the $\mathcal{O}(10\%)$ EoS-variation analytically. Figure 3.8 together with these analytic calculations support our claim that one possible origin of the universality for the I-C and Love-C relations is due to the fact that realistic NSs follow more or less the quadratic energy density profile and the deviation can explain the amount of the EoS-variation in the relations.

3.7 Conclusion

In this chapter, we derived analytic I-C, Love-C, and semi-analytic I-Love relations based on the modified Tolman VII model. We used series expansion in compactness to solve differential equations and found approximate expressions for the moment of inertia and tidal deformability. Varying the modified Tolman VII parameter α that enters the energy-density profile, we analytically showed the 10% EoS-variation in the I-C and Love-C relations, and the 1% EoS-variation in the I-Love relation that are consistent with the amount found numerically [99]. Our analytic relations more accurately describe the relations for realistic NSs than the constant density model [1] (more appropriate for quark stars [99]), especially for the I-C and Love-C relations. Our analytic relations are comparable to the fitted relations in their accuracy [99], and the former is based on a theoretical founding while the latter is phenomenological. Based on these analytic findings, we pointed out that a possible origin of the I-C and Love-C relations may be due to the energy density profile for realistic NSs approximately following a quadratic function. This can explain why the constant-density stars deviate from the NS branch in these relations. Such an origin is different from that for the universality in the I-Love-Q relations discussed in [107, 108].

Let us comment on a few possible directions for future work. One possibility includes improving the analytic results presented here. For example, one could try a different expansion in ξ or $\mathcal{C}$ for the Love-C relation, such as that in [190] for constant density stars. One could then try to construct a more accurate inversion of the relation, so that an accurate, analytic I-Love relation can be derived. Another avenue includes deriving similar, analytic expressions for multipole moments, such as quadrupole and octupole, so that one could construct, analytic, I-Love-Q relations [101, 102] and "no-hair" relations [191–193] for NSs. One could also derive analytic expressions for multipolar tidal deformabilities and construct analytic multipole Love relations [194]. Such studies may further extend our knowledge of the origin of these universal relations.

Chapter 4

Probing modified GW propagation through tidal effects of BNS

4.1 Introduction

In this chapter, we study an alternative approach of using standard sirens without EM counterparts to probe the modified GW propagation through the tidal effects of BNSs. This idea was first proposed in [195] within the context of probing cosmology with GW observations alone. The authors in [195] realized that the tidal deformability that characterizes tidal effects in a BNS depends on the intrinsic mass, so together with the measurement of the redshifted mass, one can infer the source's redshift provided that one knows the nuclear matter EoS *a priori.*

We here apply the above methodology to tests of modified GW propagation (or modified GW friction) to study how much improvement one gains from the case where one uses only BNSs with EM counterparts. We follow [112, 113] and work in a generic modified GW parametrization (Ξ_0, n), where Ξ_0 represents the ratio between the luminosity distance measured by GW and EM signals at large z while n denotes the redshift dependence on the ratio. Such a generic parametrization has a known mapping to theoretical constants in some specific non-GR theories [113]. We carry out a Fisher analysis to derive projected bounds on Ξ_0 for various n with ET and multi-band GW observations. The latter is a joint observation between ground- and space-based interferometers [196–203]. Here, we focus on multi-band observations between ET and DECIGO [204, 205]. B-DECIGO, the scientific pathfinder of DECIGO, is planned to be launched in the 2030s [205], while DECIGO is expected to be launched at a later time.

The organization of the rest of the chapter is as follows. In Sec. 4.2, we briefly introduce the formalism of how the modified luminosity distance is parameterized and the mapping between this theory-agnostic parametrization and constants in specific non-GR theories like scalar-tensor theories and phenomenological models. In Sec. 4.3, we will explain how to estimate uncertainties of the redshift measurement for a BNS event without EM counterpart from the tidal effect in the gravitational waveform. Section 4.4 describes the Fisher analysis for parameter estimation on the redshift and non-GR parameters. We present our results on the measurability of the redshift, modified GW propagation parameter, and theory-specific parameters in Sec. 4.5. In Sec. 4.6, we give concluding remarks and describe avenues for possible works.

4.2 Modified Luminosity Distance

GW sources can be used as standard sirens to probe cosmology from the relation between the luminosity distance d_L and the redshift z [206–208]. Such sources can also be used to probe gravity, since the above relation not only depends on cosmological parameters but also on the underlying gravitational theory.

4.2.1 Formalism

One can, in particular, probe generic theories that modify the Hubble friction term in the propagation equation of GWs [112][1]:

$$\tilde{h}''_A + 2\mathcal{H}[1+\alpha_M(\eta)]\tilde{h}'_A + k_{\rm gw}^2\tilde{h}_A = 0\,. \tag{4.1}$$

Here $\tilde{h}_A$ is the metric perturbation (or GW amplitude) in the Fourier domain with $A = +, \times$ representing the plus and cross polarization modes, a prime representing the derivative with respect to the conformal time η, $k_{\rm gw}$ is the wave number, $\mathcal{H} \equiv a'/a$ with a denoting the scale factor, and $\alpha_M(\eta)$ is the modified friction term. The above equation reduces to the one in GR when $\alpha_M = 0$. The friction term modification affects the GW amplitude, which can be absorbed into the luminosity distance. This leads to a difference in the luminosity distance measured through GWs $d_L^{\rm gw}(z)$ and EM waves $d_L^{\rm em}(z)$ as follows [112, 211]:

$$d_L^{\rm gw}(z) = d_L^{\rm em}(z) \exp\left[\int_0^z \frac{\alpha_M(z)}{1+z}dz\right]. \tag{4.2}$$

A useful parameterization has been proposed in [112] as

$$\frac{d_L^{\rm gw}(z)}{d_L^{\rm em}(z)} = \Xi_0 + \frac{1-\Xi_0}{(1+z)^n}. \tag{4.3}$$

---

[1] In general, the last term on the left-hand side of Eq. (4.1) can acquire non-GR corrections that modify the propagation speed of GWs and/or add a mass to the graviton, and an anisotropic stress source term may arise on the right-hand side (see e.g. [209, 210]).

Here Ξ_0 corresponds to the constant ratio of the luminosity distance in the limit $z \to \infty$ while n shows the redshift dependence of the ratio. GR is recovered when $\Xi_0 \to 1$ and this is the case when $z \to 0$. Such a parameterization allows us to treat the modification in the luminosity distance measurement from GWs in a generic way, and at the same time to map the modified GW propagation parameters (Ξ_0, n) to theoretical constants in known gravitational theories beyond GR.

4.2.2 Mapping to Scalar-tensor Theories and Phenomenological Models

In this work, we consider scalar-tensor theories and phenomenological models as specific examples [113].

4.2.2.1 Horndeski Theories

Let us first review scalar-tensor theories. We consider, in particular, theories within Horndeski theories [212], which are most general scalar-tensor theories with field equations containing up to second-order derivatives (see e.g. [213] for a recent review). The action is given by [113]

$$S = \int d^4x\sqrt{-g}\left[\sum_{i=2}^{5}\mathcal{L}_i + \mathcal{L}_{\rm m}(g_{\mu\nu}, \psi_{\rm m})\right] \tag{4.4}$$

with Lagrangian densities

$$\mathcal{L}_2 = G_2(\phi, X),$$

$$\mathcal{L}_3 = G_3(\phi, X)\Box\phi,$$

$$\begin{aligned}\mathcal{L}_4 =& G_4(\phi, X)\mathcal{R} - 2G_{4X}(\phi, X)\left[(\Box\phi)^2 - (\nabla_\mu\nabla_\nu\phi)^2\right],\\ \mathcal{L}_5 =& G_5(\phi, X)G_{\mu\nu}\nabla^\mu\nabla^\nu\phi + \frac{1}{3}G_{5X}(\phi, X)\\ & \times\left[(\Box\phi)^3 - 3\Box\phi(\nabla_\mu\nabla_\nu\phi)^2 + 2(\nabla_\mu\nabla_\nu\phi)^3\right],\end{aligned}$$

where ϕ is the scalar field, $X \equiv \partial_\mu\phi\partial^\mu\phi$, $\mathcal{R}$ and $G_{\mu\nu}$ represent the Ricci scalar and Einstein tensor in the Jordan frame metric $g_{\mu\nu}$. $G_i(\phi, X)$ are arbitrary functions of ϕ and X and $G_{iX} \equiv \partial G_i/\partial X$. The matter field ψ_m in the Lagrangian density for matter $\mathcal{L}_m$ is minimally coupled to gravity. Given that GW170817 placed a stringent bound on the propagation speed of GWs c_gw [12,214], we consider $G_{4X} = 0$ and $G_5 = \text{const.}$, which guarantees that $c_\mathrm{gw} = 1$ [215–217].

The correction to the Hubble friction term is related to G_4 through the effective Planck mass M_eff as

$$\alpha_M = \frac{d\ln M_\mathrm{eff}^2}{d\ln a}, \quad M_\mathrm{eff}^2 = 2G_4\,. \tag{4.5}$$

The modified GW propagation parameters are given by [113]

$$\Xi_0 = \lim_{z\to\infty}\frac{M_\mathrm{eff}(0)}{M_\mathrm{eff}(z)}, \quad n \approx \frac{\alpha_{M0}}{2(\Xi_0 - 1)}, \tag{4.6}$$

where α_{M0} is α_M at the present time.

As an example of Horndeski theories, we consider $f(R)$ gravity, where the Einstein-Hilbert action is modified with $R \to R + f(R)$ for an arbitrary function f. G_4 then becomes

$$G_4 = \frac{1 + f_R}{2}M_\mathrm{P}^2, \tag{4.7}$$

where $M_{\rm P}$ is the Planck mass that is related to the effective Planck mass as $M_{\rm P} = \lim_{z\to\infty} M_{\rm eff}(z)$. $f_R \equiv f'(R)$ and a prime represents a derivative with respect to R. For such a model, Ξ_0 and n are given by

$$\begin{aligned} \Xi_0 &= \sqrt{1+f_{R0}} \approx 1 + \frac{1}{2} f_{R0}, && (4.8) \\ n &\approx \left(\frac{f_R'}{f_R}\right)_0, && (4.9) \end{aligned}$$

where the subscript 0 corresponds to the present value. In particular, we consider a model proposed by Hu and Sawicki (HS). Ξ_0 and n for the HS $f(R)$ gravity are given in Table 4.1 where $\bar{n}$ is a positive integer and Ω_M is the matter energy density parameter.

$f(R)$ gravity is a special case of Brans-Dicke theory [218]. G_4 and G_2 in the latter theory are given by

$$G_4(\phi) \equiv \frac{M_{\rm P}^2\,\phi}{2}\,, \tag{4.10}$$

and $G_2 = -U(\phi) + X\omega(\phi)/\phi$, where ω is the Brans-Dicke function and U is the scalar field potential. The theory reduces to $f(R)$ gravity when $\omega = 0$. The mapping of (Ξ_0, n) to Brans-Dicke theory is given in Table 4.1, where $\delta\phi_0 \equiv \phi_0 - 1$.

4.2.2.2 Phenomenological Models

The second model we consider is a phenomenological parameterization on α_M motivated by a time-varying effective Planck mass $M_{\rm eff}$. We consider two different parameterization for α_M:

Non-GR Model	$\Xi_0 - 1$	n
HS $f(\mathrm{R})$ [219]	$\frac{1}{2} f_{\mathrm{R}0}$	$\frac{3(\bar{n}+1)\Omega_M}{4-3\Omega_M}$
designer $f(\mathrm{R})$ [220]	$-0.24\Omega_M^{0.76} B_0$	$3.1\Omega_M^{0.24}$
Brans-Dicke [218]	$\frac{1}{2}\delta\phi_0$	$\frac{3(\bar{n}+1)\Omega_M}{4-3\Omega_M}$
power law α_M [221]	$\frac{\alpha_{M0}}{2\bar{n}}$	$\bar{n}$
DE density α_M [221, 222]	$-\frac{\alpha_{M0}}{6\Omega_\Lambda \ln\Omega_M}$	$-\frac{3\Omega_\Lambda}{\ln\Omega_M}$
power law M_{eff} [223]	$\frac{1}{2}\Omega_+$	$\bar{n}$

Table 4.1: Mapping of the modified GW propagation parameters (Ξ_0, n) to parameters in scalar-tensor theories (top) and phenomenological models for α_M or the effective Planck mass M_{eff} (bottom) [113].

(i) power law:

$$\alpha_M = \alpha_{M0} a^{\bar{n}}; \tag{4.11}$$

(ii) dark energy density:

$$\alpha_M = \alpha_{M0} \frac{\Omega_\Lambda(a)}{\Omega_{\Lambda 0}}, \tag{4.12}$$

where Ω_Λ is the dark energy density parameter.

Once again, Ξ_0 and n for these models are summarized in Table 4.1.

In Appendix A, we review other models within Horndeski theories and phenomenological classes, and give the mapping to (Ξ_0, n) in Table 4.1.

4.3 Redshift Inference through tidal effect

To probe gravity from the luminosity distance-redshift relation in Eq. (4.3), one needs an independent measurement of d_L and z. The former is measured from the amplitude of GWs while the latter is more challenging to measure as it typically degenerates with the mass. If a BNS event has an associated EM counterpart, one can use the redshift information of the host galaxy, which has been used for GW170817 to measure the Hubble constant [207] and also to give future forecasts on testing the modified GW propagation [112]. However, BNS events with EM counterparts are expected to be rare, with a fraction of only $\sim 10^{-3}$ or so [165].

An alternative method to measure the redshift with GW observations alone is to use the tidal effect [195]. Such an effect in BNS is characterized by tidal deformabilities or Love numbers that depend on the intrinsic (source-frame) masses of NSs. Together with the redshifted mass measurement, one can break the degeneracy between the redshift and the mass to extract the former. This method requires one to know the nuclear matter EoS *a priori* which still has relatively large uncertainties. One may use future GW observations of nearby BNS sources ($z \lesssim 0.1$) with EM counterparts to determine the EoS, and use those of BNSs with large z to probe the modified GW propagation [195, 224].

Let us explain this tidal method in more detail by taking NRTidalv2 [225, 226] as an example. The tidal contribution to the GW phase in the frequency domain is given by

$$\psi_{\mathrm{T}}(x) = -\frac{13}{8\eta}\kappa_{\mathrm{eff}} x^{5/2} P(x), \tag{4.13}$$

where $x = (\pi M_z f)^{1/3}$ with $M_z = (1+z)M$ is the total redshifted mass with M representing the intrinsic total mass, η representing the symmetric mass ratio $m_A m_B/(m_A + m_B)^2$ and f is the observed GW frequency. $P(x)$ is a Padé-resummed function given by,

$$P(x) = \frac{1 + n_1 x + n_{3/2} x^{3/2} + n_2 x^2 + n_{5/2} x^{5/2} + n_3 x^3}{1 + d_1 x + d_{3/2} x^{3/2} + d_2 x^2}, \tag{4.14}$$

where the coefficients can be found in [225]. κ_{eff} is related to the tidal Love number k as

$$\kappa_{\mathrm{eff}} = \frac{2}{13}\left[\left(1 + 12\frac{X_B}{X_A}\right)\left(\frac{X_A}{C_A}\right)^5 k^A + (A \leftrightarrow B)\right]. \tag{4.15}$$

Here, subscript A and B denotes the two component stars, $X_A \equiv m_A/M$ and the compactness is given by $C_A \equiv m_A/R_A$ with the stellar radius R_A. Since k depends on the intrinsic stellar mass instead of the redshifted one, the tidal effect can be used to extract the redshift information from a GW observation alone.

4.4 Fisher Analysis

In this project, we carry out a parameter estimation based on a Fisher analysis [227], which is valid for sources with sufficiently large signal-to-noise ratios (SNRs). We perform two different Fisher calculations, one for the redshift estimate and another for the modified GW propagation parameter estimate. Below, we will explain each of these Fisher analyses in turn.

4.4.1 Redshift Estimate

The first step is to estimate the measurability of the redshift by using template gravitational waveforms of BNSs, which we take as the (non-spinning) IMRPhenomD-NRTidalv2 waveform [225, 226, 228, 229]. It consists of the IMRPhenomD waveform for point-particle binaries with an updated tidal effect added to the phase. The waveform $\tilde{h}$ in the frequency domain can be written as

$$\tilde{h}(f) = \tilde{A}(f) e^{-i\psi(f)}, \tag{4.16}$$

where $\tilde{A}$ is the IMRPhenomD amplitude[2] while ψ is the phase given by[3]

$$\psi(f) = \psi_{\rm pp}(f) + \psi_{\rm T}(f). \tag{4.17}$$

Here $\psi_{\rm pp}$ is the (non-spinning) point-particle term that is taken from the IMRPhenomD waveform while $\psi_{\rm T}$ is the tidal contribution given in Eq. (4.13) that is parameterized by the Love number k. In our analysis, we use the tidal deformability $\lambda \equiv (2/3)R^5 k$, which is a function of the NS mass m. It is convenient to Taylor

---

[2] The NRTidal waveform also has a tidal correction to the amplitude, though the tidal effect is mostly determined from the phase and thus we do not include such effects in the amplitude for simplicity.

[3] In this work, we include the tidal phase only in the inspiral part of the IMRPhenomD phase, though we have checked that our results are unaffected even if we include the tidal phase also in the intermediate portion of the waveform.

expand $\lambda(m)$ about a fiducial mass m_0 as [195, 224]

$$\begin{aligned}\lambda &= \lambda_0 + \lambda_1(m - m_0) + \mathcal{O}[(m - m_0)^2] \\ &= \tilde{\lambda}_0 + \tilde{\lambda}_1 m + \mathcal{O}[(m - m_0)^2], \end{aligned} \tag{4.18}$$

where λ_i are the Taylor coefficients about m_0 while $\tilde{\lambda}_0 = \lambda_0 - \lambda_1 m_0$ and $\tilde{\lambda}_1 = \lambda_1$.

One can compute the measurability of parameters θ^i from a Fisher matrix as follows. We first assume that the detector noise is stationary and Gaussian. Then, the probability distribution of θ^i becomes also Gaussian as

$$p(\theta^i) \propto \exp\left[-\frac{1}{2}\Gamma_{ij}\left(\theta^i - \hat{\theta}^i\right)\left(\theta^j - \hat{\theta}^j\right)\right], \tag{4.19}$$

where $\hat{\theta}^i$ are the maximum likelihood parameters. Γ_{ij} is the Fisher matrix defined as

$$\Gamma_{ij} = 4\Re \int_{f_{\rm low}}^{f_{\rm high}} \frac{\partial_i \tilde{h} \partial_j \tilde{h}}{S_n(f)} df, \tag{4.20}$$

where $\partial_i \equiv \partial/\partial\theta^i$ while S_n is the noise spectral density. $f_{\rm high}$ and $f_{\rm low}$ are the high and low frequency cutoffs to be discussed later.

$$\tilde{\Gamma}_{ij} = \sum_A \Gamma_{ij}^{(A)}, \tag{4.21}$$

where A is the label of each detector. Finally, the 1σ root-mean-square error on θ_i is given by

$$\Delta\theta^i = \sqrt{(\tilde{\Gamma}^{-1})_{ii}}. \tag{4.22}$$

In Fig. 4.1, we present S_n for ET and DECIGO, together with the GW spectrum for GW170817 and a BNS with $(1.35, 1.35)M_\odot$ at $z = 1$. For ET, we choose the low and high frequency cutoffs in the Fisher matrix in Eq. (4.20) as

$$f_{\rm low}^{(\rm ET)} = 1{\rm Hz}, \quad f_{\rm high}^{(\rm ET)} = \min(f_{\rm ISCO}, f_{\rm cont}), \tag{4.23}$$

where

$$f_{\rm ISCO} = \frac{1}{6^{3/2}\pi M_z}, \tag{4.24}$$

is the frequency at the innermost stable circular orbit (ISCO) while $f_{\rm cont}$ is the (redshifted) contact frequency of two NSs and is given by

$$f_{\rm cont} = \frac{1}{2^{3/2}\pi(1+z)}\sqrt{\frac{M}{R^3}}, \tag{4.25}$$

for an equal-mass BNS with R representing the stellar radius. For an NS with a soft (stiff) EoS, the radius is relatively small (large), and $f_{\rm ISCO} < f_{\rm cont}$ ($f_{\rm ISCO} > f_{\rm cont}$). On the other hand, for DECIGO, we choose the low and high cutoff frequencies as

$$\begin{aligned} f_{\rm low}^{(\rm DEC)} &= 0.233 \left(\frac{1M_\odot}{\mathcal{M}_z}\right)^{5/8} \left(\frac{1{\rm yr}}{T_{\rm obs}}\right)^{3/8} {\rm Hz}, \\ f_{\rm high}^{(\rm DEC)} &= 100{\rm Hz}, \end{aligned} \tag{4.26}$$

where $\mathcal{M}_z = M_z \eta^{3/5}$ is the redshifted chirp mass, $T_{\rm obs}$ is the observation time and $f_{\rm low}^{(\rm DEC)}$ corresponds to the (redshifted) frequency at $T_{\rm obs}$ before coalescence.

Let us now explain parameters θ^i specific to our analysis. We use the sky-averaged waveform and the parameters are given by

$$\theta^i = (\ln\mathcal{M}_z, \eta, t_c, \phi_c, \ln A, \ln z)\,. \tag{4.27}$$

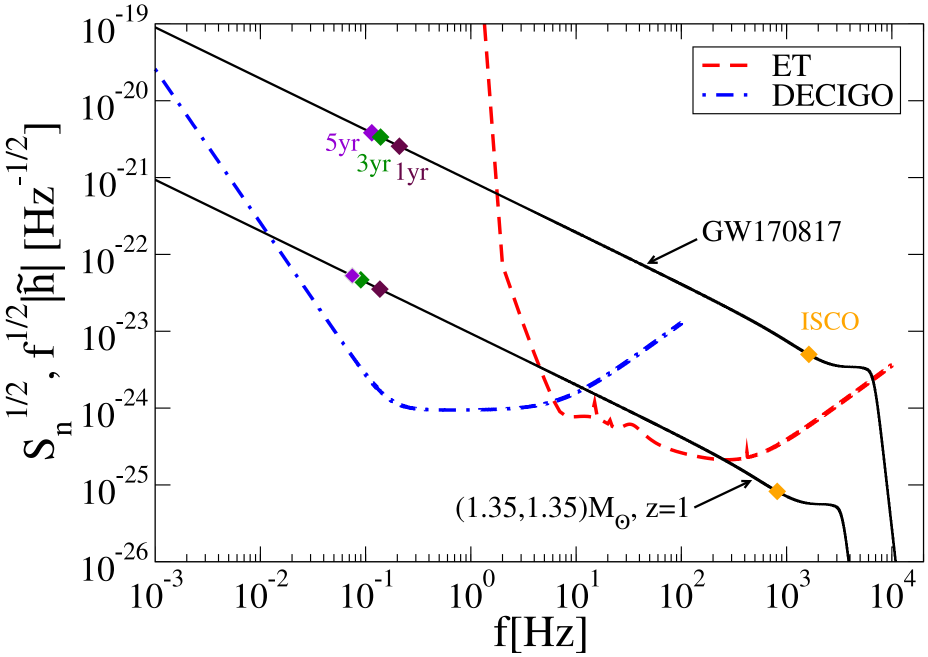

Figure 4.1: The noise spectral densities for ET [230] and DECIGO [35]. We also present the GW spectrum for GW170817 and a BNS with $(1.35, 1.35)M_\odot$ at $z = 1$. For each GW spectrum, we show the frequency at ISCO and that at 1yr, 3yr, and 5yr before coalescence.

Here $\eta = m_1 m_2/M^2$ is the symmetric mass ratio with individual masses m_A, and t_c and ϕ_c are the coalescence time and phase respectively. The amplitude parameter A is given by $A = \mathcal{M}_z^{5/6}/(\sqrt{30}\pi^{2/3} d_L^{\rm gw})$, which corresponds to the leading, sky-averaged amplitude in the frequency domain without the frequency dependence [231]. We assume the tidal parameters $\tilde{\lambda}_0$ and $\tilde{\lambda}_1$ are known *a priori* from BNSs with $z < 0.1$ (we discuss how the imperfect knowledge of the EoS affects the measurability of the redshift in Appendix C). Regarding fiducial values for Fisher analyses, we choose $m_1 = m_2 = m_0 = 1.35M_\odot$, $t_c = 0$, $\phi_c = 0$, and vary z or $d_L^{\rm gw}$. Fiducial values for $\tilde{\lambda}_0$ and $\tilde{\lambda}_1$are summarized in Table C.1 in Appendix C for three EoSs as representatives of soft, intermediate, and stiff classes: SLy [232], MPA1 [233] and MS1 [234].

4.4.2 Parameter Estimation for Modified GW Propagation

We now move on to explaining the second Fisher analysis for estimating the measurability of cosmological parameters and the modified GW propagation parameter. We consider a spatially-flat Universe and work on the following four parameters [112]:

$$p^i = (\ln H_0, \ln\Omega_M, w_0, \Xi_0)\,. \tag{4.28}$$

Here H_0 is the Hubble constant, Ω_M is the matter-energy density parameter at present time, w_0 is the EoS parameter for dark energy [235, 236][4] while Ξ_0 is the modified GW propagation parameter in Eq. (4.3). The luminosity distance measured by EM observations depends only on the first three parameters in Eq. (4.28) as

$$d_L^{\rm em}(z) = (1+z)\int_0^z \frac{{\rm d}\tilde{z}}{H(\tilde{z})}, \tag{4.29}$$

with the Hubble parameter given by

$$H(z) = H_0\sqrt{\Omega_M(1+z)^3 + (1-\Omega_M)(1+z)^{3(1+\omega_0)}}. \tag{4.30}$$

We can construct a Fisher matrix to estimate the measurability of the parameters p^i by studying how $\ln d_L^{\rm gw}$ depends on each of these parameters and comparing it with a measurement error on $\ln d_L^{\rm gw}$. Combining information from multiple events, we can

---

[4] The EoS for dark energy is given by $P_{\rm DE} = w_0 \varepsilon_{\rm DE}$ where $P_{\rm DE}$ and $\varepsilon_{\rm DE}$ are the pressure and energy density of dark energy.

write down the Fisher matrix as [224]

$$F_{ij}^{(\mathrm{A})} = \sum_a \frac{(\partial \ln d_L^{\mathrm{gw}}/\partial p_i)(\partial \ln d_L^{\mathrm{gw}}/\partial p_j)}{(\Delta \ln d_L^{\mathrm{gw}})^2_{(\mathrm{A})}}\bigg|_a . \tag{4.31}$$

Here a labels each BNS while $A = (\mathrm{gw}, \mathrm{em})$ labels whether the redshift is measured from GWs through the tidal effects or from EM counterparts. $(\Delta \ln d_L^{\mathrm{gw}})^2_{(\mathrm{A})}$ is the total error on $\ln d_L^{\mathrm{gw}}$ given by

$$\begin{aligned}(\Delta \ln d_L^{\mathrm{gw}})^2_{(\mathrm{A})} &= (\Delta \ln d_L^{\mathrm{gw}})^2_{\mathrm{gw}} + \epsilon_A \left(\frac{\partial \ln d_L^{\mathrm{gw}}}{\partial z}\Delta z\right)^2 \\ &\quad + (\Delta \ln d_L^{\mathrm{gw}})^2_{\mathrm{lens}} ,\end{aligned} \tag{4.32}$$

with $\epsilon_{\mathrm{gw}} = 1$ and $\epsilon_{\mathrm{em}} = 0$. The first term on the right-hand side is the measurement error on $\ln d_L^{\mathrm{gw}}$ through GWs, the second term is due to the measurement error on the redshift, while the last term is due to the gravitational lensing given by [237]

$$(\Delta \ln d_L^{\mathrm{gw}})_{\mathrm{lens}} \simeq 0.05z. \tag{4.33}$$

The first two terms are computed from Γ_{ij} in the previous subsection, either with ET alone or with the multi-band observations. For BNSs with redshift identified from EM counterparts, the measurement error on the redshift is typically negligible and we drop the second term in Eq. (4.32) (i.e. $\epsilon_{\mathrm{em}} = 0$) for such cases.

In this work, we follow [224] and assume that all BNSs are identical except for their redshifts. Under this assumption, one can turn the summation in F_{ij} into an integral as

$$F_{ij}^{(\mathrm{A})} = \int_{z_{\min}}^{z_{\max}} \frac{(\partial \mathrm{ln} d_L^{\mathrm{gw}}/\partial p_i)(\partial \mathrm{ln} d_L^{\mathrm{gw}}/\partial p_j)}{(\Delta \ln d_L^{\mathrm{gw}})^2_{(\mathrm{A})}} \mathcal{R}(z) \mathrm{d}z. \tag{4.34}$$

We choose the minimum and maximum redshifts ($z_{\min}$ and $z_{\max}$) as $z_{\min} = 0.1$ and $z_{\max} = 2$. This is because we use BNS sources with $z < 0.1$ (with EM counterparts) to determine the NS EoS while the SNR becomes too small for detection when $z > 2$ [5]. $\mathcal{R}(z)$ is the distribution of BNS mergers which is given by [239]

$$\mathcal{R}(z) = \frac{4\pi r^2(z)\dot{n}_0 s(z)}{H(z)(1+z)} T_{\mathrm{obs}}, \tag{4.35}$$

in which $\dot{n}_0 = 10^{-6}\mathrm{Mpc}^{-3}\mathrm{yr}^{-1}$ [240] is the current BNS merger rate, $r(z)$ is the comoving distance, and

$$s(z) = \begin{cases} 1 + 2z & (z \leq 1) \\ \frac{3}{4}(5 - z) & (1 < z \leq 5) \end{cases}, \tag{4.36}$$

shows the redshift evolution of the merger rate. We show the BNS merger rate within each redshift bin and the accumulated merger rate up to a given redshift in Fig. 4.2.

Unlike the multiband GW observations of stellar-mass BBHs with ground-based detectors and LISA whose rate is much lower than that with ground-based detectors alone [196], the rate for joint detection of GWs from BNSs with ET + DECIGO is comparable or even higher than ET alone. This is because the signal-to-noise ratio (SNR) of BNS GW detection with DECIGO is higher than that of ET, as can be seen

---

[5] The SNR for a sky-averaged BNS at $z = 2$ with ET is 4.5 which may be smaller than the detection threshold SNR, though the latter may be reduced if we have additional information from DECIGO for multi-band observations (see e.g. [238] for related work).

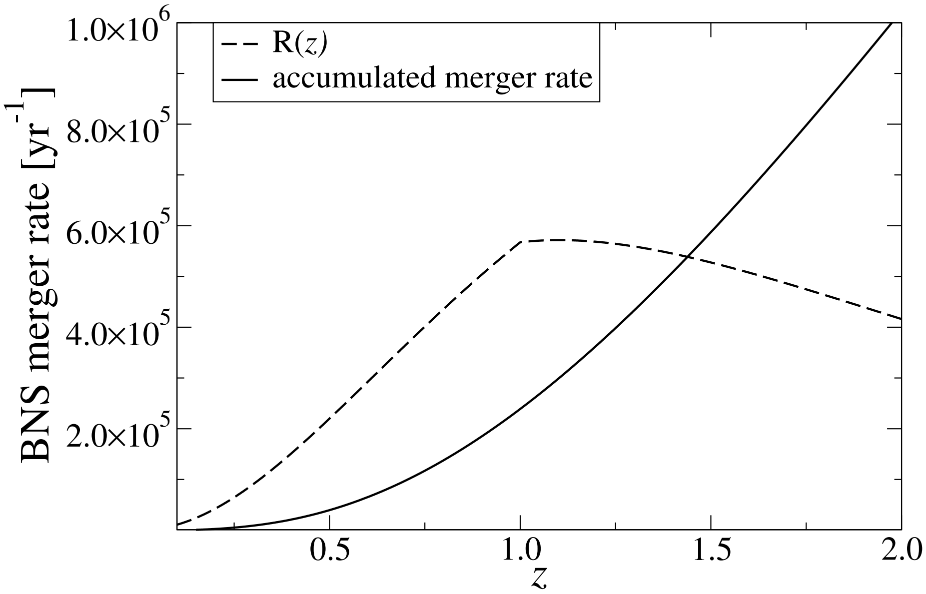

Figure 4.2: The BNS merger rate per unit redshift ($\mathcal{R}(z)$) and the accumulated number of events up to a given redshift ($\int_0^z \mathcal{R}(z)dz$) as a function of z.

from Fig. 4.1. Thus, DECIGO can detect GW signals from BNSs whose signals can also be detected with ET. Moreover, since DECIGO will be able to give a precursor alert to ET, the detection SNR threshold may be lowered (as we explain in footnote 5), which will increase the rate compared to the case with ET alone.

Given that various cosmological observations, including cosmic microwave background (CMB), baryon acoustic oscillation (BAO) and supernovae, measured cosmological parameters with some errors, one can impose prior on such parameters for our Fisher analysis. For simplicity, we impose Gaussian priors with standard deviation $\sigma^0_{p^i}$ for each parameter. The Fisher matrix for BNSs with redshift identification due to EM counterparts is given by,

$$\tilde{F}^{(\mathrm{em})}_{ij} = \alpha_{\mathrm{em}} F^{(\mathrm{em})}_{ij} + \frac{\delta_{ij}}{(\sigma^0_{p^i})^2}\,. \tag{4.37}$$

Here $\alpha_{\rm em}$ is the fraction of total BNSs with which the redshifts are identified through their EM counterparts [165]. One can further add BNSs whose redshift is identified through the tidal measurement of GWs as

$$\tilde{F}_{ij}^{(\rm gw+em)} = (1-\alpha_{\rm em})F_{ij}^{(\rm gw)} + \alpha_{\rm em}F_{ij}^{(\rm em)} + \frac{\delta_{ij}}{(\sigma_{p^i}^0)^2}\,. \tag{4.38}$$

The 1-σ root-mean-square error on p^i can be estimated as

$$\Delta p^i = \sqrt{(\tilde{F}^{-1})_{ii}}\,. \tag{4.39}$$

We end this section by describing the fiducial values and priors for p^i. For the former, we use $H_0 = 67.64\,{\rm km\ s^{-1}Mpc^{-1}}, \Omega_M = 0.3087, w_0 = -1, \Xi_0 = 1$. This corresponds to the ΛCDM model in GR with the first two parameter values being the best-fit values from CMB, BAO and supernovae observations [112]. For the prior, we use [112]

$$(\sigma_{\Xi_0}^0, \sigma_{\omega_0}^0, \sigma_{\ln H_0}^0, \sigma_{\ln \Omega_M}^0) = (\infty, 0.0535, 0.018, 0.039), \tag{4.40}$$

which is obtained from the same datasets as those for the above fiducial values.

4.5 Results

We now present our main results. We first show the measurability of redshift with GW observations. We next use this to compute the measurability of the modified GW propagation parameter Ξ_0 and cosmological parameters. We finally map the projected bounds on Ξ_0 to those on example theories within the Horndeski class and example phenomenological models.

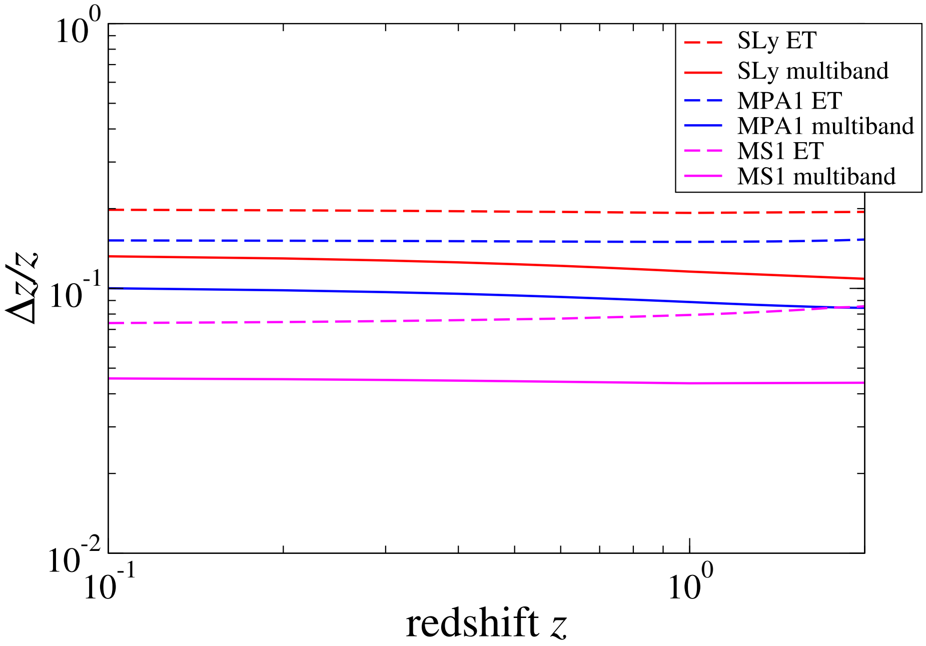

Figure 4.3: The fractional uncertainty of the redshift as a function of the source redshift with ET and multi-band GW observations (with a 3-yr observation for the latter). We present the results for SLy (soft) [232], MPA1 (intermediate) [233] and MS1 (stiff) [234] EoSs. Notice that the uncertainty is insensitive to z and is larger for softer EoSs.

4.5.1 Redshift Inference

We begin by showing the measurement accuracy of z with GW observations using ET and multi-band (ET + DECIGO) detections in Fig. 4.3 for the three representative EoSs. Observe that the redshift can be measured to $\mathcal{O}(10\%)$ and is insensitive to the BNS redshift. Notice also that the measurability of z increases as the EoS becomes stiffer. This is because the NS radius becomes larger, and the tidal effect in turn becomes stronger. We further see that the multi-band detection improves the measurability of z from the case with ET alone by $\sim 50\%$. The result for ET in Fig. 4.3 is consistent with that in [195]. The difference originates from using e.g. different point-particle waveforms (IMRPhenomD v.s. Taylor F2) and tidal effects (5 and 6PN v.s. NRTidal fit).

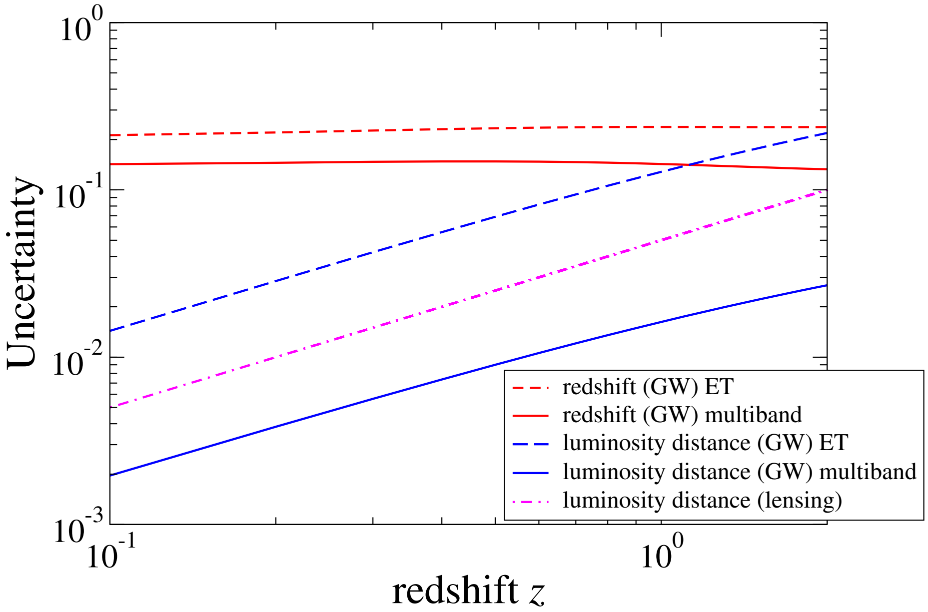

Figure 4.4: Various sources of the luminosity distance measurement uncertainties in Eq. (4.32) as a function of the BNS redshift. We use the SLy EoS and assume multi-band observations (with a 3-yr observation time). Notice that the redshift uncertainty dominates the error budget throughout.

Before showing bounds on Ξ_0, let us first present in Fig. 4.4 different errors on the luminosity distance (Eq. (4.32)) in the second Fisher matrix F_{ij}. We chose SLy EoS and the multi-band observation. Notice that the error propagated from the redshift measurement in Fig. 4.3 dominates the other two errors (direct measurement of d_L^{gw} from GWs and the lensing) for both ET alone and multi-band observations. On the other hand, when there is an EM counterpart, the error from redshift is negligible and it is the lensing (direct luminosity distance measurement) error that gives the dominant contribution for multi-band (ET alone) observations.

4.5.2 Constraints on GW propagation parameter Ξ_0

Having the redshift measurability at hand, we next present the measurability of the modified GW propagation parameter Ξ_0. Figure 1.2 in executive summary Sec. 1.1.3 presents such a measurement error on Ξ_0 for $n = 2.5$ against the fraction $\alpha_{\rm em}$ of the redshift identification of BNSs through EM counterparts for ET and multi-band observations. We show the results using BNSs with EM counterparts only (whose redshifts are identified), and combining BNSs with and without the counterparts. We chose the SLy EoS and an observation time of 3 yrs for DECIGO in the multi-band observations (see Appendix B for how the results change with a different choice of EoSs and observation time). Notice first that the addition of BNS events without EM counterparts improves the measurability of Ξ_0 from the case with EM counterparts alone by a factor of a few. Notice also that for the combined case, BNSs with EM counterparts have a noticeable contribution when $\alpha_{\rm em} \gtrsim 0.1$ for ET alone and $\alpha_{\rm em} \gtrsim 0.01$ for multi-band observations (where the red curves drop). Furthermore, when $\alpha_{\rm em} \sim 1$ (i.e. most of BNSs have EM counterparts), multi-band observations significantly improve the bound on Ξ_0 from the case with ET alone. This is because when $\alpha_{\rm em} \sim 1$, the error budget in the luminosity distance measurement is different between ET and multi-band cases as already explained in Sec. 4.5.1 and in Fig. 4.4.

Next, Fig. 4.5 presents the measurability of Ξ_0 against the index n in the luminosity distance ratio expression (Eq. (4.3)) for a multi-band observation with combined BNS events (both with and without redshift identification through EM counterparts) for $\alpha_{\rm em} = 2 \times 10^{-3}$ [6]. We show the results for the three representative EoSs. Notice first that the measurement error of Ξ_0 is mostly insensitive to n and varies only by $\sim 20\%$. Notice also that the error decreases for stiffer EoSs (MS1), which is consistent with the measurement error of z in Fig. 4.3.

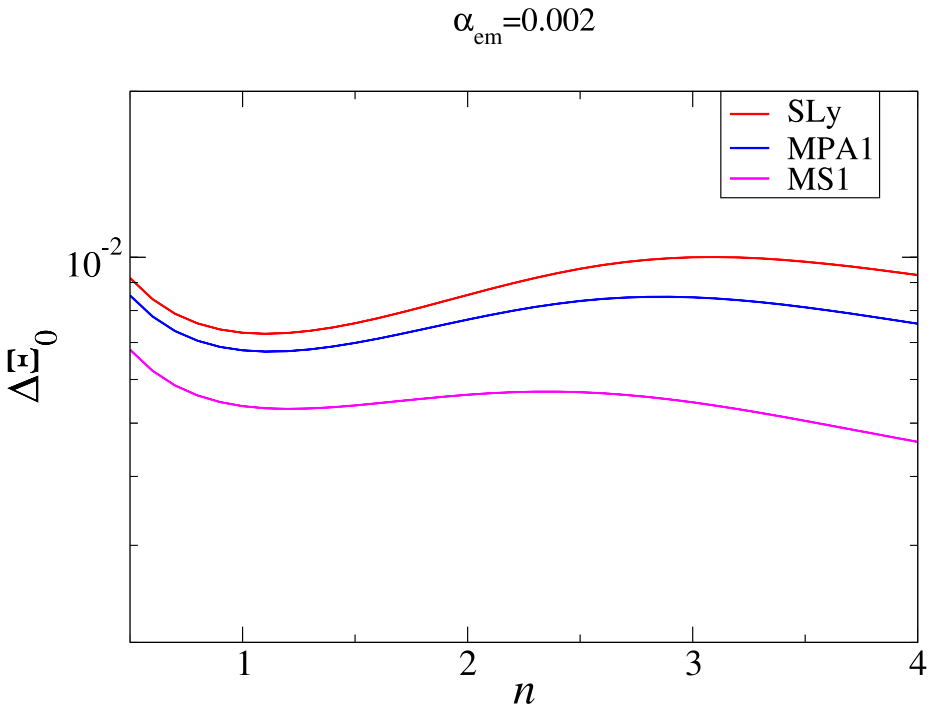

Figure 4.5: Measurability of Ξ_0 against the index n in the modified GW luminosity distance in Eq. (4.3) for three representative EoSs. We consider a multi-band observation with combined BNS events with and without EM counterparts. We fix the fraction of BNSs with EM counterparts as $\alpha_{\rm em} = 2 \times 10^{-3}$. The observational time is 3 years. Observe that the measurability is not very sensitive to the choice of n.

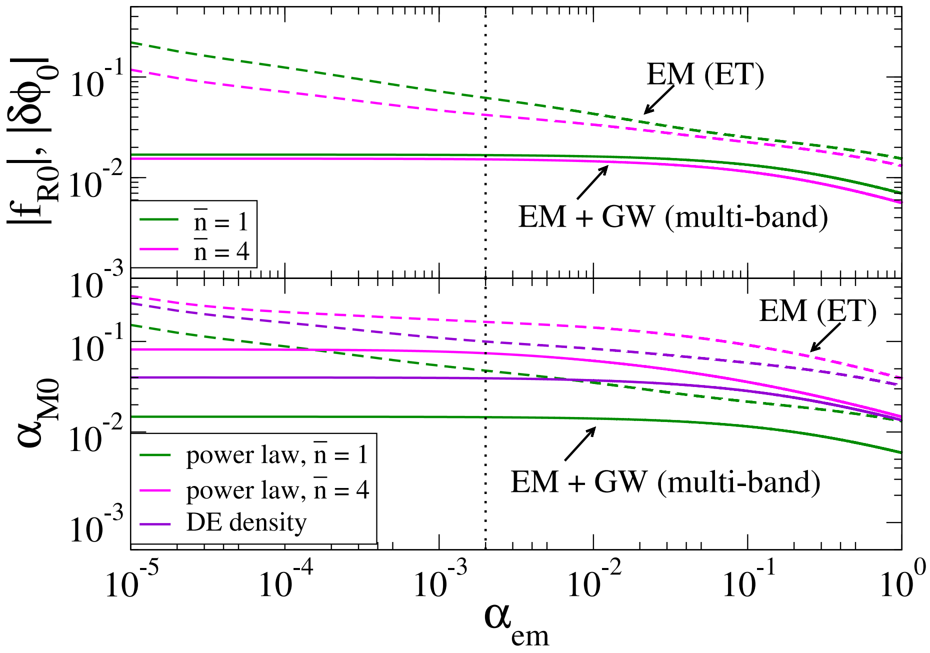

Figure 4.6: (Top) Projected bounds on parameters in the HS $f(R)$ gravity ($|f_{R0}|$) and Brans-Dicke theory ($|\delta\phi_0|$) as a function of the fraction $\alpha_{\rm em}$ for redshift identification through EM counterparts. We present the bounds for the following two cases: (i) GW observations of BNSs with ET where the sources' redshifts are identified through EM counterparts only (dashed), and (ii) multi-band GW observations of BNSs whose redshifts are identified through either EM counterparts or GW tidal effects (solid). For each case, we show the bounds for two choices of the positive index $\bar{n}$. We assume 3-year observations and the SLy EoS. The dashed vertical line at $\alpha_{\rm em} = 2 \times 10^{-3}$ [165] corresponds to an example value for the fraction of BNSs with redshift identification. (Bottom) A similar bound on the phenomenological $\alpha_{\rm M}$ models in Eqs. (4.11) and (4.12).

4.5.3 Mapping to Horndeski Theories

Finally, we consider mapping the bounds on the modified GW propagation parameter Ξ_0 to those on scalar-tensor theories and phenomenological models. The top panel of Fig. 4.6 shows bounds on the HS $f(R)$ gravity $|f_{R0}|$ and Brans-Dicke theory $|\delta\phi_0|$ as a function of $\alpha_{\rm em}$ for various choices of the positive integer $\bar{n}$. Observe that the addition of BNSs with redshift identification through tidal measurements and the use of multi-band observations improve the bounds on these theories from the case with ET observations of BNSs with EM counterparts by a factor of 2–10. Observe also that the bounds are insensitive to a variation in $\bar{n}$, especially for the multi-band case.

Similarly, the bottom panel of Fig. 4.6 presents bounds on α_{M0} in the two phenomenological models mentioned in Sec. 4.2.2.2. Notice that the amount of improvement on the bounds with the addition of BNSs without EM counterparts and multi-band observations is similar to those on scalar-tensor theories in Fig. 4.6. Notice also that the variation in $\bar{n}$ is larger for this case than that for scalar-tensor theories in the top panel.

4.6 Conclusion

In this chapter, we considered using GWs from BNS mergers both with and *without* EM counterparts to probe a modified GW propagation effect in the amplitude due

---

[6] The fraction $\alpha_{\rm em} = 2 \times 10^{-3}$ is derived for short gamma-ray bursts assuming that 2% of them points to us and only 10% of them can have measurable redshift due to noisy spectrum, dimming at high redshift, etc. [165]. This fraction can be larger for other sources, such as kilonova, or if we take into account off-axis emission.

to a modified friction in the tensor perturbation evolution. For the events without EM counterparts, we use the tidal information to break the degeneracy between the redshift and the mass [195]. We found that by including BNSs without EM counterparts and using multi-band GW observations between ET and DECIGO, one can improve the measurability on the modified GW propagation parameter Ξ_0 by a factor of a few compared to the case with ET observations of BNSs with EM counterparts that has been studied previously. We further mapped these projected bounds on Ξ_0 to those on specific non-GR theories and phenomenological models. For example, we found that a parameter in an $f(R)$ gravity can be constrained to $|f_{R0}| \lesssim 10^{-2}$. These findings show the impact of using the tidal information and multi-band observations to probe a modified GW propagation (or modified friction) effect entering the waveform amplitude.

We end by presenting possible directions for future avenues. One could improve the analysis here by carrying out a Bayesian parameter estimation study (instead of a Fisher analysis) and drawing BNSs from a population model to allow for different parameters (like masses). One should also relax the sky-averaged assumption and account for sky location and orientation of a BNS. This could be important given that there was a strong correlation between the luminosity distance and the inclination angle for GW170817 [62]. However, in Appendix D, we carried out an additional analysis by relaxing the sky-averaged assumption for DECIGO and showed that in most cases, the measurement error for the luminosity distance is still smaller than that from the redshift measurement. This suggests that the result presented here with the sky-averaged analysis should not change much for multi-band observations, even if one accounts for the correlation. It would be also important to take into account systematic uncertainties due to imperfect knowledge of the EoS and certain universal relations may help to break the degeneracy among various tidal parameters [63, 104, 182, 241, 242]. Lastly, one could also attempt to combine the tidal method presented here with other approaches that do not require EM counterparts, such as correlating dark sirens with galaxy catalogs [116,243,244] or using the known NS mass distribution [245, 246].

Part B

Testing general relativity with binary black holes and mixed binaries

Chapter 5

Constraints on EdGB gravity from black hole-neutron star GW events

5.1 Introduction

In this chapter, we derive new bounds on EdGB gravity through GWs from NSBH binaries. Some forecasts on constraining the theory with such systems were made in [247] based on a Fisher analysis. The authors showed that the existing bounds can be improved further for NSBH binaries with a sufficiently small BH mass. We here derive new bounds through a Bayesian analysis using GW200105 and GW200115 [248]. We also consider GW190814, which is consistent with BBH or NSBH, and find bounds on EdGB gravity for the BBH and NSBH assumptions separately. We perform Bayesian inference to analyze the above events by adopting IMRPhenomXPHM waveform [249–251] (a phenomenological inspiral-merger-ringdown waveform for precessing BBHs in GR) as our base GR waveform and include EdGB corrections to the inspiral phase. We set a high frequency cutoff as $f_{\mathrm{high}} = 0.018/M$ [252] (for the total mass M in a unit of second) on the strain data, since the EdGB modifications to the waveform within the PN expansion is only valid for the phase at the inspiral stage. We also carry out independent Fisher analyses for cross-checking the results.

We improve previous analyses by deriving and including EdGB corrections to the waveform phase to higher PN orders. Recently, Shiralilou et al. [253,254] derived the waveform valid to 1PN order higher than the leading tensor/scalar non-dipole and scalar dipole emission respectively. We update this by taking the waveform in scalar-tensor theories (in the Jordan frame) valid to 2PN relative to the leading for each of dipole and non-dipole contributions [255]. We apply a conformal transformation in scalar-tensor theories to go from the Jordan frame to the Einstein frame, find the mapping between the scalar fields in scalar-tensor theories and EdGB gravity, and use the scalar charges for BHs and NSs in the latter theory. We checked that this correctly reproduces the leading -1PN correction in EdGB gravity known previously [120,134].

This chapter is organized as follows. We first review EdGB gravity and corrections to the waveform phase in Sec. 5.2. We next explain in Sec. 5.3 two methods of data analysis adopted in this work, namely Bayesian inference through MCMC and a Fisher analysis. In Sec. 5.4, we present our results and conclude in Sec. 5.5.

5.2 Einstein-dilation Gauss-Bonnet gravity

Let us first review EdGB gravity within the context of sGB theory and explain corrections to the gravitational waveform from GR.

5.2.1 Theory

We begin by presenting the action for sGB gravity [130–133]:

$$S = \int d^4x\sqrt{-g}\left[\frac{\mathcal{R}}{16\pi} - \frac{1}{2}(\nabla\phi)^2 + \alpha_{\text{GB}} f(\phi)\mathcal{R}^2_{\text{GB}}\right] + S_m \,. \tag{5.1}$$

Here g is the determinant for the metric $g_{\mu\nu}$, $\mathcal{R}$ is the Ricci scalar, ϕ is a scalar field, α_{GB} is the coupling constant between the scalar field and the metric, S_m is the matter action, and

$$\mathcal{R}^2_{\text{GB}} = R_{\mu\nu\sigma\rho}R^{\mu\nu\sigma\rho} - 4R_{\mu\nu}R^{\mu\nu} + \mathcal{R}^2 \,, \tag{5.2}$$

is the GB invariant. $f(\phi)$ is an arbitrary function of the scalar field that determines how it is coupled to the metric. EdGB gravity is realized by choosing $f(\phi) = e^{-\gamma\phi}$ for a constant γ. As shown in [256,257], this theory can be written in a second-order, hyperbolic form that is well-posed for numerical relativity evolution within a range of parameter space.

String theory predicts even higher-order curvature terms in the action that we do include in the analysis. To justify this and treat the theory as an effective field theory, we work in the small coupling approximation scheme (or reduced-order scheme) where we assume that the GR contribution is dominant and handle EdGB corrections as small perturbations. In particular, we define a dimensionless coupling constant

$$\zeta \equiv \frac{16\pi\alpha^2_{\text{GB}}}{L^4} \,, \tag{5.3}$$

where L is the characteristic length of the system and assume $\zeta \ll 1$. This technique has been used to find scalar charges of compact objects [81, 134, 258], corrections to the GW phase at the inspiral stage [134], and to carry out numerical simulations of BBH mergers [259].

Let us study the theory within the small coupling approximation scheme in more detail. We perturb field equations in $\alpha_{\rm GB}$ and solve them order by order. Then, $\phi = \mathcal{O}(\alpha_{\rm GB})$ and one can expand $f(\phi)$ in small ϕ as:

$$f(\phi) = f(0) + f'(0)\phi + \mathcal{O}(\phi^2)\,. \tag{5.4}$$

The first term is a constant and this does not change the field equations from the GR ones as the GB invariant is a topological term and can be rewritten as a total derivative. Thus, the leading effect comes from the second term where the scalar field is linearly coupled to the GB invariant. For this reason, we consider the following action in this work:

$$S = \int d^4x\sqrt{-g}\left[\frac{\mathcal{R}}{16\pi} - \frac{1}{2}(\nabla\phi)^2 + \alpha_{\rm GB}\phi\mathcal{R}^2_{\rm GB}\right] + S_m\,, \tag{5.5}$$

where we have absorbed $f'(0)$ into $\alpha_{\rm GB}$. In this theory, BHs can have non-vanishing scalar charges [81, 134] while NSs do not [258].

Current astrophysical bounds on $\sqrt{\alpha_{\rm GB}}$ are summarized in Table 1.3 in the executive summary section. Besides these, one could use electromagnetic radiation emitted by gas or stars orbiting BHs. For example, simulations of the reflection spectrum of thin accretion disks with present and future X-ray missions show that current missions cannot distinguish BHs in GR and those in sGB gravity, while next-generation missions may be able to distinguish them [260]. Another possibility is to use Solar System experiments, though they are weaker than the astrophysical bounds in Table 1.3 by six orders of magnitude [131, 261] as the curvature of spacetime in the vicinity of the Sun is much smaller than that of BHs and NSs.

5.2.2 Gravitational Waveforms

We next find EdGB corrections to the gravitational waveform phase. Given that most of the signal-to-noise ratios (SNRs) for GWs from NSBHs and (small mass) BBHs come from the inspiral portion, we focus on the inspiral stage in our analysis. The leading correction to the phase at the inspiral stage enters at -1PN order due to the scalar dipole radiation and was derived in [131]. Some of the higher PN corrections were recently derived in [253, 254]. Here, we identified even higher PN corrections using the waveforms in scalar-tensor theories [255] (see Appendix E for details of the derivation).

Within the stationary phase approximation [262, 263], the waveform in the Fourier space is given by:

$$h(f) = A(f) \exp\left[i\, \Psi(f)\right] , \quad \Psi(f) = \Psi_{\mathrm{GR}}(f) + \delta\Psi(f) \,. \tag{5.6}$$

Here $A(f)$ is the amplitude, Ψ_{GR} is the GR phase, and the EdGB correction to the phase $\delta\Psi$ (up to $\mathcal{O}(\alpha_{\mathrm{GB}}^2)$) is given in a form

$$\delta\Psi = \sum_i \delta\Psi_{\,i\,\mathrm{PN}} = \frac{\alpha_{\mathrm{GB}}^2}{M^4} \sum_i c_i\, v^{-5+2i} \,. \tag{5.7}$$

Here $v = (\pi M f)^{1/3}$ is the relative velocity of the binary constituents with GW frequency f and the total mass $M = m_1 + m_2$, where m_1 and m_2 are the masses of the primary and secondary objects of the system. The coefficients c_i up to 2PN order can be found in Appendix E. We note that corrections at 1.5PN and 2PN terms contain terms that have not been computed yet and are thus not fully complete.

5.3 Data Analysis

In this project, we carry out two independent analyses to find constraints on $\sqrt{\alpha_{\text{GB}}}$. The first method is an MCMC analysis based on Bayesian inference by using the publicly-available GW data. The second method is a simpler Fisher analysis that can be used to obtain rough bounds on $\sqrt{\alpha_{\text{GB}}}$ to cross-check the results from the first method.

Which GW events shall we consider? Since the EdGB corrections to the phase are proportional to α_{GB}^2/M^4, such corrections become larger for systems with smaller total masses. If the data is consistent with GR, this translates to a stronger bound on EdGB gravity. Furthermore, the leading scalar dipole radiation is proportional to the square of the difference in the scalar charges between two objects. This means that we expect to find stronger bounds on $\sqrt{\alpha_{\text{GB}}}$ for systems with smaller mass ratios ($q = m_2/m_1 < 1$). For these reasons, we will consider the two NSBH events, GW200105 and GW200115, from O3a, (whose total masses are $10.9 M_\odot$ and $7.1 M_\odot$, and mass ratios are 0.22 and 0.26, respectively [248, 264]). We also employ GW190814 [265] whose mass ratio is small (0.11) and the secondary mass is $m_2 \approx 2.6 M_\odot$. The system is consistent with both BBH and NSBH, though the probability of an NS with 2.6 $M_\odot$ may be small [266–268]. Given the uncertainty in the nature of the secondary object, we consider both possibilities of GW190814 being a BBH and an NSBH. We also use GW151226, a BBH with a relatively small mass, to check our results against those found previously [126, 127].

5.3.1 Bayesian Inference

To unveil the basic information of compact binary systems behind GW events, one usually makes use of a reliable method – Bayesian inference [269, 270]. According to the Bayes' theorem, a posterior probability $p(\boldsymbol{\vartheta}|d,\mathcal{H})$ on parameters $\boldsymbol{\vartheta}$ from data d under a given hypothesis $\mathcal{H}$ is given by:

$$p(\boldsymbol{\vartheta}|d,\mathcal{H}) = \frac{p(d|\boldsymbol{\vartheta},\mathcal{H})\;p(\boldsymbol{\vartheta}|\mathcal{H})}{p(d|\mathcal{H})} = \frac{p(d|\boldsymbol{\vartheta},\mathcal{H})\;p(\boldsymbol{\vartheta}|\mathcal{H})}{\int d\boldsymbol{\vartheta}\;p(d|\boldsymbol{\vartheta},\mathcal{H})\;p(\boldsymbol{\vartheta}|\mathcal{H})}. \tag{5.8}$$

Here $p(d|\boldsymbol{\vartheta},\mathcal{H})$ is the likelihood function while $p(\boldsymbol{\vartheta}|\mathcal{H})$ is the prior on $\boldsymbol{\vartheta}$. With a stationary Gaussian noise, the log-likelihood function $\log p(d|\boldsymbol{\vartheta},\mathcal{H})$ can be expressed as:

$$\log p(d|\boldsymbol{\vartheta},\mathcal{H}) = \log\bar{\alpha} - \frac{1}{2}\sum_k \left\langle d_k - h_k(\boldsymbol{\vartheta})|d_k - h_k(\boldsymbol{\vartheta})\right\rangle, \tag{5.9}$$

where the index k refers to different detectors and $\log\bar{\alpha}$ is the normalization factor while d_k and $h_k(\boldsymbol{\vartheta})$ are the data and waveform templates from given detectors. The inner product between complex functions a and b is defined as:

$$\langle a(t)|b(t)\rangle = 2\int_{f_{\rm low}}^{f_{\rm high}} \frac{\tilde{a}^*(f)\tilde{b}(f)+\tilde{a}(f)\tilde{b}^*(f)}{S_n(f)}df. \tag{5.10}$$

Here $*$ refers to a complex conjugate, $S_n(f)$ is the power spectral density (PSD) of given detectors, f_{low} is the low frequency cutoff of GW data (to be explained later), and $f_{\mathrm{high}} = 0.018/M$ [252] is the approximate maximum frequency at the inspiral stage. Notice that f_{high} is not a fixed number, but varies among different MCMC realizations.

For our analysis, the parameters are those in GR plus the EdGB coupling constant $\sqrt{\alpha_{\mathrm{GB}}}$:

$$\boldsymbol{\vartheta} = (\mathcal{M}, q, a_1, a_2, \theta_1, \theta_2, \phi_1, \phi_2, \alpha, \delta, \psi, \iota, \phi_{\mathrm{ref}}, t_c, d_L, \sqrt{\alpha_{\mathrm{GB}}})\,. \tag{5.11}$$

Here $\mathcal{M} = (m_1 m_2)^{3/5}/M^{1/5}$ is the detector frame chirp mass, $q = m_2/m_1 (< 1)$ is the mass ratio, a_A are the dimensionless spin magnitudes while (θ_A, ϕ_A) are the polar and azimuthal angles of the spin angular momentum of the Ath body, (α, δ) are the sky location of the binary (right ascension and declination), ψ is the polarization angle of GWs with respect to the earth-centered coordinates, ι is the inclination angle of the binary's orbital angular momentum relative to the detector's line of sight, ϕ_{ref} is the reference phase at the reference frequency, t_c is the coalescence time, and d_L is the luminosity distance.

We find posterior distributions on all parameters $\boldsymbol{\vartheta}$ for GW events taken from Gravitational Wave Open Science Center (GWOSC) [271] as follows. We perform MCMC samplings through the PyCBC package [272,273] and emcee_pt sampler [274] with 500 walkers and 3 temps. We analyze 32 s of data for GW200105 and 64 s of data for GW200115. Regarding the low frequency cutoff, we set $f_{\mathrm{low}} = 20\,\mathrm{Hz}$ except for

LIGO Livingston for GW200115, where $f_{\rm low} = 25\,{\rm Hz}$ was used to avoid some excess noise localized at low frequency [248]. Regarding priors, we assume a uniform distribution on $\sqrt{\alpha_{\rm GB}}$ with $[0, 5]\,{\rm km}$ for GW200105, GW200115 and GW190814 (BBH), and $[0, 15]\,{\rm km}$ for GW190814 (NSBH). As for spin priors, we adopt isotropic spin distribution on (θ_A, ϕ_A) with a high-spin prior on the magnitude, a_1 and $a_2 \lesssim 0.99$, for all of the MCMC analyses.

For the base waveform model in GR, we adopt IMRPhenomXPHM (that is also used in [168]) from LALSimulation package [275], which is a phenomenological model in the frequency domain that includes spin precession and higher order multipole radiation modes. As the $(l, m) = (3, 3)$ mode is found to be non-negligible for GW200105, GW200115, and GW190814 [248,265], we include this mode with corresponding EdGB corrections in these events while we only consider the dominant $(l, m) = (2, 2)$ mode for GW151226. We adopt IMRPhenomXPHM model that was constructed for BBHs. As for NSBHs, the tidal effects were found to be negligible [248] for the events considered in this work, and thus it is safe to adopt the same waveform model.

5.3.2 Fisher analysis

We next explain the second method for the data analysis, namely the Fisher information matrix (FIM) method [262, 276–278], which is valid when the SNR is large and the noise is stationary and Gaussian. FIM is previously used and introduced in Chap. 4. To minimize repetitive referencing, a brief explanation of this technique was provided.

We begin by expanding the log-likelihood function at the maximum likelihood point $\boldsymbol{\vartheta}^{\rm ML}$ for a given hypothesis $\mathcal{H}$:

$$\begin{aligned}\log p(d|\boldsymbol{\vartheta}, \mathcal{H}) &\propto -\frac{1}{2}\sum_k \langle d_k - h_k(\boldsymbol{\vartheta})|d_k - h_k(\boldsymbol{\vartheta})\rangle\,,\\ &\propto -\frac{1}{2}\sum_k \Gamma^{(k)}_{ij}\,\Delta\boldsymbol{\vartheta}^i\,\Delta\boldsymbol{\vartheta}^j\,,\end{aligned} \tag{5.12}$$

where $\Delta\boldsymbol{\vartheta}^i = \boldsymbol{\vartheta}^{i,\,\rm ML} - \boldsymbol{\vartheta}^i$ is the error of a given parameter relative to the value at the maximum likelihood point and $\Gamma^{(k)}_{ij}$ is the FIM evaluated at the maximum likelihood point $\boldsymbol{\vartheta}^{\rm ML}$:

$$\Gamma^{(k)}_{ij} = \left\langle \frac{\partial h(\boldsymbol{\vartheta})}{\partial \boldsymbol{\vartheta}^i} \,\middle|\, \frac{\partial h(\boldsymbol{\vartheta})}{\partial \boldsymbol{\vartheta}^j} \right\rangle\bigg|_{\boldsymbol{\vartheta}^{\rm ML}}\,, \qquad \Gamma_{ij} = \sum_k \Gamma^{(k)}_{ij}\,, \tag{5.13}$$

where the inner product is given in Eq. (5.10) with the power spectral density $S_n^{(k)}$ for the kth detector. Notice that the elements of FIM are partial derivatives of the waveform template with respect to given parameters. Similar to the Bayesian inference, one can introduce a prior to find the posterior distribution on $\boldsymbol{\vartheta}$. We follow [279] and impose a Gaussian prior, for simplicity, with a standard deviation $\sigma^{(0)}_{\vartheta^i}$ on each parameter. FIM then becomes

$$\tilde{\Gamma}_{ij} = \frac{1}{\left(\sigma^{(0)}_{\theta^i}\right)^2}\delta_{ij} + \Gamma_{ij}\,. \tag{5.14}$$

The inverse of the FIM is an estimator of the error covariance matrix Σ_{ij}. The standard error is the square root of the diagonal elements of the covariance matrix. For a given parameter $\boldsymbol{\vartheta}^i$, the standard error can be expressed as:

$$\sqrt{\langle(\delta\boldsymbol{\theta}^i)^2\rangle} = \sqrt{\Sigma_{ii}}\,, \quad \Sigma_{ij} = \left(\tilde{\Gamma}^{-1}\right)_{ij}\,. \tag{5.15}$$

Regarding the base waveform in GR, we follow [120] and use IMRPhenomD instead of IMRPhenomXPHM that was used for the Bayesian inference analysis (as explained in Sec. 5.3.1). The former is a simpler version of the latter in the sense that it is valid only for spin-aligned systems (i.e. no spin precession) and includes only the dominant mode. This simplification is justified as we only use the FIM analysis to cross-check the results from the Bayesian inference, which is more robust. Moreover, Perkins et al. [127] showed that the difference in the waveform models between IMRPhenomPv2 (a precessing model similar to IMRPhenomXPHM but only includes the dominant mode) and IMRPhenomD changes the bound on $\sqrt{\alpha_{\rm GB}}$ only by $\sim 20\%$. For simplicity, we use a sky-averaged waveform (and rescale the amplitude so that the SNR matches with the observed one) and the parameters for this second method are as follows:

$$\boldsymbol{\vartheta} = \left(\mathcal{M}, q, a_1, a_2, \phi_{\rm ref}, t_c, d_L, \alpha_{\rm GB}^2\right)\,. \tag{5.16}$$

Notice that we take $\alpha_{\rm GB}^2$ as our EdGB parameter instead of $\sqrt{\alpha_{\rm GB}}$. This is because the former is what enters directly in the waveform and if one chooses to use the latter, the Fisher matrix becomes singular when we take the fiducial value as $\alpha_{\rm GB} = 0$ (for the fiducial values of other parameters, we use those reported by LVC and set $\phi_{\rm ref} = t_c = 0$). We impose a Gaussian prior [279] with the standard deviation of $\sigma_{a_1} = \sigma_{a_2} = 1$ and $\sigma_{\phi_{\rm ref}} = \pi$.

	GW200105	GW200115	GW190814		GW151226	combined
	NSBH	NSBH	NSBH	BBH	BBH	
Fisher	1.55	0.91	7.39	0.90	4.19 (2.51 [127])	0.59
Bayesian	1.90	1.33	2.72	0.37 (0.4 [168])	3.43 (4.4 [127])	1.18
small coupl. limit	4.40	2.94	11.4	1.27	3.81	—

Table 5.1: Constraints on $\sqrt{\alpha_{\rm GB}}$ [km] at 90% credible level with Fisher analysis and Bayesian inference from selected NSBH and BBH events. For GW190814, we consider both NSBH and BBH possibilities due to the uncertainty in the nature of the secondary object. These constraints are derived by using the leading phase correction at -1PN order, which are improved by approximately 7–15% if we include higher PN corrections. Our results for GW190814 (BBH) and GW151226 are consistent with those found in previous work shown in brackets. The last column shows the bound by combining posteriors from GW200105, GW200115, GW190814 (NSBH), and the combined posterior from selected BBHs from GWTC-1 and GWTC-2 catalogs obtained in [127]. The last row shows the upper limits on $\sqrt{\alpha_{\rm GB}}$ that is valid within the small coupling approximation (Eq. (5.17)). Observe that all the bounds from the Fisher and Bayesian analyses are within these upper limits, showing the validity of our results.

5.4 Results

5.4.1 Leading Correction

We now present our results. Constraints on $\sqrt{\alpha_{\rm GB}}$ from various GW events with Bayesian and Fisher analyses are summarized in Table 5.1[1]. Here, we only included the leading -1PN correction to the waveform phase. Observe that the bounds from

---

[1] Notice that there are some differences in Bayesian and Fisher analyses, such as the waveform modeling (PhenomXPHM vs IMRPhenomD), sGB parameter ($\sqrt{\alpha}_{\rm sGB}$ vs $\alpha^2_{\rm sGB}$) and its prior (uniform vs Gaussian). This may explain why Fisher bounds are weaker than the Bayesian ones in some cases.

the two analyses for each GW event agree within a factor of ~ 3. Since the phase corrections are derived within the small coupling approximation, we need to check whether the bounds presented here satisfy this approximation. Following [127], we require

$$16\pi \frac{\alpha_{\rm GB}^2}{m^4} \leq 0.5\,, \tag{5.17}$$

where m is the smallest length scale in the binary. We choose $m = m_2$ (the mass of the smaller BH) for BBH while $m = m_1$ (the mass of the BH) for NSBH[2]. We present in Table 5.1 the upper limit on $\sqrt{\alpha_{\rm GB}}$ that satisfies the above bound. Notice that all the Fisher and Bayesian bounds satisfy the small coupling approximation and thus are reliable. Notice also that our Fisher and Bayesian results for GW151226 and GW190814 (BBH) are consistent with those in [127, 168][3]. Our results are also roughly consistent with the forecast made in [247] for bounds on $\sqrt{\alpha_{\rm GB}}$ with NSBHs derived through a Fisher analysis. For example, the bound for a BH mass of $8M_\odot$ and an SNR of 8 (similar to GW200115 where the BH mass is $5.7M_\odot$ and an SNR of 11.4 [248]) was found to be $\sqrt{\alpha_{\rm GB}} \lesssim 0.4$km with advanced LIGO's design sensitivity which has a slightly different shape for the noise curve than that with O3 detectors.

The most stringent constraint comes from GW190814 (BBH) though the event is still consistent with NSBH and thus such a bound may not be robust. The reason why the bound on $\sqrt{\alpha_{\rm GB}}$ is stronger for BBH than NSBH for GW190814 can be understood

---

[2] For simplicity, we use the mass estimates found by LVC assuming GR while Ref. [127] used the median values of the masses from posterior distributions including $\sqrt{\alpha_{\rm GB}}$.

[3] Perhaps a small discrepancy in the results for GW190814 (BBH) is due to the fact that we vary the coalescence time t_c in our Bayesian inference while it seems that Ref. [168] fixed this parameter (at least the posterior distribution on this parameter is not shown in Appendix A of [168]).

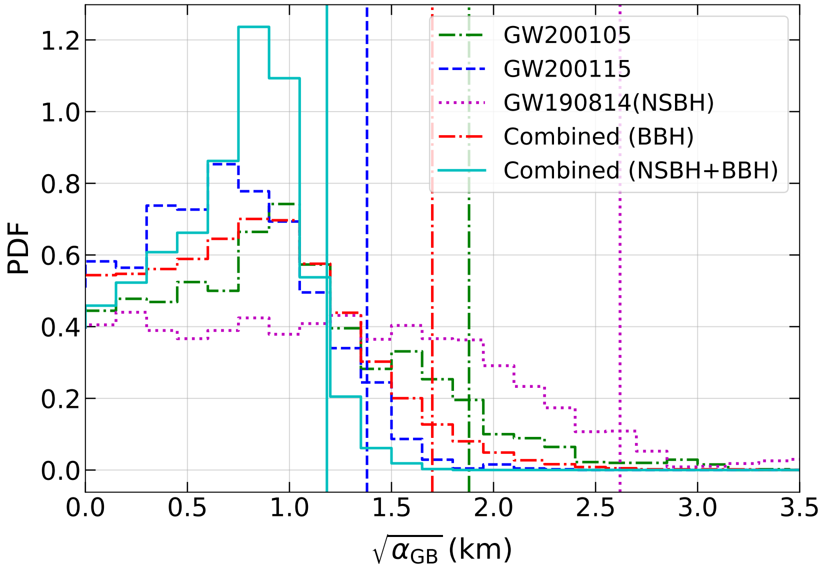

Figure 5.1: Posterior probability distributions for $\sqrt{\alpha_{\rm GB}}$ from selected GW events. We also show an upper bound on $\sqrt{\alpha_{\rm GB}}$ at 90% credible level for each event as vertical lines, which indicates the result is consistent with GR. The posteriors are found by including only the leading EdGB correction to the phase at -1PN order.

as follows. First, notice that the leading correction to the phase is proportional to $(m_1^2 s_2 - m_2^2 s_1)^2/M^4$ (see Eq. (E.7)). Second, let us consider the case $m_1 \gg m_2$ for simplicity. In this case, we find $c_{-1} \propto 1$ for BBH while $c_{-1} \propto q^4$ for NSBH (the scalar charge s_2 is 0 for an NS). Thus, the EdGB correction can be much larger for BBH than NSBH.

Besides constraints from the events GW151226 and GW190814 (BBH) which have already been derived in the previous works [127, 168], we here derived bounds from NSBHs (GW200105, GW200115, and GW190814) for the first time. We present the posterior distributions for $\sqrt{\alpha_{\rm GB}}$ for these events in Fig. 5.1. The bound from GW200115 is $\sqrt{\alpha_{\rm GB}} \lesssim 1.33\,$km, which is stronger than the bound obtained in [127] by stacking several BBHs from GWTC-1 and GWTC-2 catalogs ($\sqrt{\alpha_{\rm GB}} \lesssim 1.7\,$km). Observe that the posterior distributions are quite different from Gaussian centered at $\sqrt{\alpha_{\rm GB}} = 0$, which partially explains the difference between the Fisher and Bayesian results (see also TABLE II, FIG. 2, and FIG. 3 in [127]).

Furthermore, we derive combined bounds by multiplying normalized posterior histograms on $\sqrt{\alpha_{\rm GB}}$[4] from GW200105, GW200115, GW190814 (with the NSBH assumption that gives us a more conservative bound), and combined BBH bounds in [127]. We found a stringent bound of $\sqrt{\alpha_{\rm GB}} \lesssim 1.18\,$km through the Bayesian analysis as shown in Table 5.1 and Fig. 5.1.

5.4.2 Effects of Higher PN Corrections

We next study the effect of higher PN corrections to the waveform phase by including PN corrections up to 2PN as presented in Appendix E. Perkins et al. [127] carried out a similar analysis though such higher PN corrections were not available at that time. Thus, the authors considered three different ways to parameterize the unknown 0PN correction (which is 1PN higher than the leading −1PN correction) based on the functional forms at 1PN order in GR and the leading −1PN EdGB corrections. They then marginalized over such a parameter and concluded that higher PN corrections do not affect the results much and the bounds derived with the leading correction are robust. We check this outcome by using explicit forms of the higher PN corrections in EdGB gravity.

---

[4] This corresponds to the second method discussed in Sec. IIIE of [127] for obtaining combined bounds.

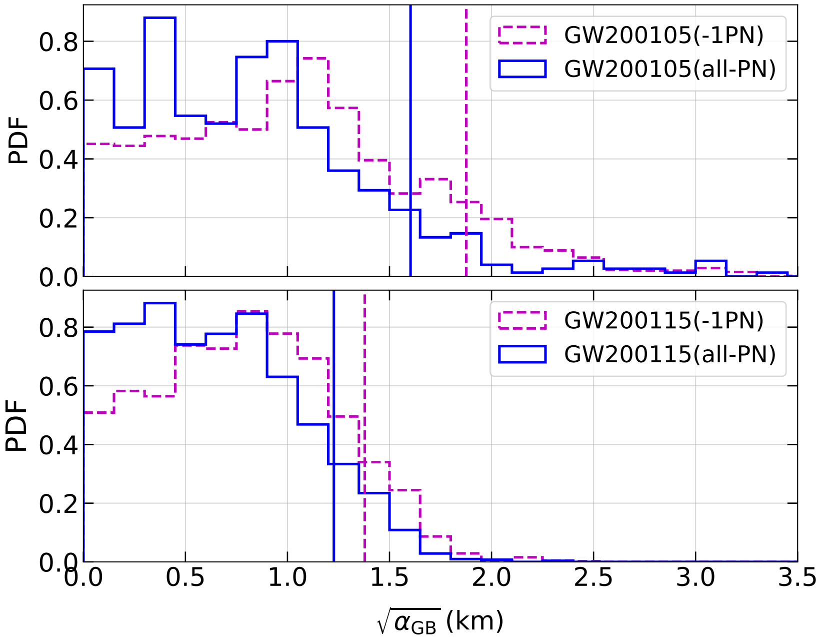

Figure 5.2: A comparison of the posteriors on $\sqrt{\alpha_{\rm GB}}$ from the leading -1PN correction and those including higher PN corrections (up to 2PN) for GW200105 (top) and GW200115 (bottom). Observe that the 90% upper bounds on $\sqrt{\alpha_{\rm GB}}$ are improved by 14.5% for GW200105 and 6.9% for GW200115, respectively.

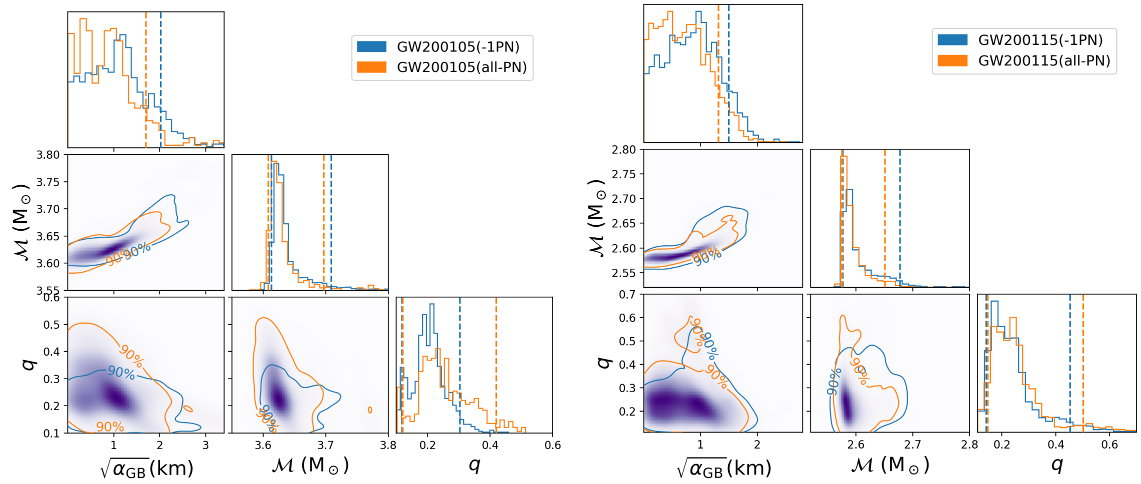

Figure 5.3: Posterior probability distributions for the EdGB coupling constant $\sqrt{\alpha_{\rm GB}}$, the chirp mass $\mathcal{M}$, and the mass ratio q from GW200105 (left) and GW200115 (right). We compare the marginal posterior distributions for the case with the leading EdGB correction at -1PN order (blue) and the case including higher PN orders up to 2PN (orange). The purple-shaded regions indicate the posterior probabilities of the latter case, and the solid lines represent the 90% credible regions for the two cases. The vertical dashed lines show the one-sided 90% confidence interval for $\sqrt{\alpha_{\rm GB}}$ and the two-sided 90% credible intervals for $\mathcal{M}$ and q.

Figure 5.2 presents posteriors on $\sqrt{\alpha_{\mathrm{GB}}}$ for GW200105 and GW200115 with and without higher PN corrections, while Fig. 5.3 shows corresponding corner plots on $\sqrt{\alpha_{\mathrm{GB}}}$, $\mathcal{M}$ and q. Notice that the inclusion of the higher PN corrections does not affect the posteriors much, especially for GW200115. The 90% credible upper bound on $\sqrt{\alpha_{\mathrm{GB}}}$ improves from the case with the leading correction by 14.5% for GW200105 and 6.9% for GW200115 respectively. These findings are consistent with those in [127] and a very recent work [280] that investigated the improvement one obtains when including higher PN order terms.

5.5 Conclusion

In this chapter, we derived bounds on EdGB gravity using GWs from NSBH binaries. Using the leading PN correction, we found $\sqrt{\alpha_{\mathrm{GB}}} \lesssim 1.33\,\mathrm{km}$ as a 90% credible limit from GW200115, which is stronger than the bound in [127] found by combining selected BBHs from GWTC-1 and GWTC-2 catalogs. We also derived combined bounds by stacking posterior distributions on $\sqrt{\alpha_{\mathrm{GB}}}$ from GW200105, GW200115, GW190814 and the combined posteriors from selected BBHs in [127], and found $\sqrt{\alpha_{\mathrm{GB}}} \lesssim 1.18\,\mathrm{km}$. We further derived higher PN corrections in the waveform phase up to 2PN order from the results in scalar-tensor theories [255]. Using these, we improved bounds on $\sqrt{\alpha_{\mathrm{GB}}}$ for GW200105 and GW200115 from the case with leading PN correction alone by 14.5% and 6.9% respectively.

The analysis carried out here can easily be extended to probe other theories of gravity. We looked at constraining dynamical Chern-Simons gravity [281], which is a parity-violating quadratic gravity whose leading PN correction to the phase is derived in [282]. Similar to the case with BBHs [120, 126, 127], we were not able to find meaningful bounds that satisfy the small coupling approximation. For future work, one could consider e.g. sGB gravity with the coupling function $f(\phi) \propto \phi^2$ or $f(\phi) \propto 1 - e^{-6\phi^2}$ that admits spontaneous scalarization of BHs [142, 144].

Chapter 6

Tests of gravity with GWs through machine learning

6.1 Introduction

In this chapter, we investigate accelerating the Bayesian inference (especially for theories beyond GR) on GW strain data, facilitated by the use of neural networks. Machine-learning techniques, particularly artificial neural networks, are a promising avenue for enabling this necessary speed-up in the analysis. Neural networks, which are flexible function approximators, can be trained to optimize a loss function by tuning millions of parameters using stochastic gradient descent. These networks can approximate extremely complex functions, and since functions can parametrize conditional distributions, neural networks can be used to model posterior probability distributions for physical parameters from GW data. After training these networks on GW data, they can be run on new data to produce accurate estimates of the posterior probability distributions in a fraction of the time a stochastic sampler would take. There have recently been several efforts to speed up parameter estimation by using such neural networks within GR [157–160].

One key observation made in the field [157, 158, 160] is that, while the network is able to learn posterior distributions, it is not necessary to obtain posterior samples during training. By applying Bayes' rule, training of a neural network can be done using only samples from the prior and the likelihood. This method, known as the likelihood-free inference, does not require any likelihood evaluations, making it a faster and more efficient approach compared to those that do require these evaluations. This technique is especially useful in cases where it is time-consuming and computationally expensive to derive posterior samples and evaluate the likelihood. A very promising approach of the likelihood-free inference is achieved by introducing a latent variable and performing a variational Bayesian inference, implemented by using the variational autoencoder framework [283, 284]. Gabbard et al. [158] first applied a conditional variational autoencoder (CVAE) to GW parameter estimation and successfully reproduced results from classic sampling methods with significantly less time.

Our main goal in this project is to build from these initial successes in GR and to train a neural network to perform GW data analysis in theories beyond GR. With these machine-learning techniques, we expect to be able to explore a larger parameter space of these theories than those considered by most previous studies. This will give a more accurate representation of how well beyond-GR theories can be constrained with GWs. The new analysis will also provide a more efficient framework for searching for deviations from GR that may start to appear in the data once current (and future) detectors begin their operation with a sufficiently improved sensitivity that some of the subtle effects currently hidden in the noise begin to emerge from these instrumental backgrounds. Our work is still underway, with the latest objective of reproducing the GR inference results presented in [160].

This chapter is organized as follows. In section 6.2, we describe the basic neural network model, CVAE, for the parameter estimation. In section 6.3, we discuss some preliminary results we found with CVAE and the model's drawback. In section 6.4, we briefly discuss how to tackle this drawback through the use of normalizing flows [160]. We will also summarize our current progress and future directions in this section.

6.2 Conditional Variational Autoencoder (CVAE)

Variational autoencoders (VAEs) have emerged as one of the most popular approaches to unsupervised learning of complicated distributions and were shown to perform well when applied towards high-resolution synthetic image generation [285], computational imaging inference [286], predicting future from static images [287] and so on. The "C" added in front of "VAE" stands for "conditional", which means that the output conditions on certain latent distributions are modelled by Gaussian distributions. A CVAE can learn a compressed representation (or latent space) of high-dimensional data such as images, audios, or texts. However, in addition to the data, a CVAE can also take a set of conditions as input, allowing it to generate samples that are conditioned on specific attributes or characteristics. As a variational inference technique, CVAE is well-suited for function approximations and promises faster results than current sampling approaches.

6.2.1 Loss Function

For all neural network models, the central goal of their training is to minimize a pre-defined loss function, characterized by the features we wish the network to learn. Let us first begin by discussing the construction of loss functions in CVAE suitable for posterior inference of a GW strain data.

As mentioned in Chapter 5, the objective of GW parameter estimation is to ascertain the physical parameters responsible for generating the detected strain data in the detectors, which is achieved through Bayes' theorem. Assuming a prior distribution $p(x)$ of system parameters x, and strain data y conditioned on x has a likelihood model $p(y|x)$, the posterior distribution would be

$$p(x \mid y) = \frac{p(y \mid x)p(x)}{p(y)}. \tag{6.1}$$

The goal for CVAE is to generate a distribution $r_\theta(x \mid y)$ that is equal to the true posterior distribution $p(x \mid y)$ given by a Bayesian sampling. This goal can be achieved by minimizing the cross entropy, defined as,

$$H(p, r) = -\int dx\, p(x \mid y) \log r_\theta(x \mid y). \tag{6.2}$$

This quantity becomes minimum when the two distributions are equal. To be more specific, we wish to make $r_\theta(x \mid y)$ as similar as possible to the target for all possible measurements y, which makes the target loss function to be

$$H = -\mathrm{E}_{p(y)}\left[\int dx p(x \mid y) \log r_\theta(x \mid y)\right], \tag{6.3}$$

where $\mathrm{E}_{p(y)}[\cdot]$ represents taking the expectation value over the distribution of y. Then, by converting the expectation value into an integral weighted by y and using Bayes' theorem, we have

$$H = -\int dx p(x) \int dy p(y \mid x) \log r_\theta(x \mid y), \tag{6.4}$$

where $p(x)$ is the prior distribution on x and $p(y \mid x)$ is the likelihood.

In CVAE, the distribution $r_\theta(x \mid y)$ is constructed through a latent variable z [286] as

$$r_\theta(x \mid y) = \int dz r_{\theta_1}(z \mid y) r_{\theta_2}(x \mid y, z). \tag{6.5}$$

Here $r_{\theta_1}(z \mid y)$ is called the encoder network, while $r_{\theta_2}(x \mid y, z)$ is the decoder network (θ_1 and θ_2 represent the trainable parameters in the networks). It has been shown in [288] that simply minimizing H over θ_1 and θ_2 is an intractable problem, and a network cannot be trained to directly perform the task. A recognition function $q_\phi(z \mid x, y)$ is needed to derive an evidence lower bound (ELBO) for the loss function. Thus, instead of minimizing the loss function, we will minimize the ELBO instead.

Before we derive the ELBO for H, let us first define the Kullback-Leibler (KL) divergence. This divergence is a type of statistical distance that measures how one probability distribution is different from a second, reference probability distribution. Then we could write the KL-divergence between the recognition function and the distribution $r_\theta(z \mid x, y)$ as

$$\mathrm{KL}\left[q_\phi(z \mid x,y) || r_\theta(z \mid x,y)\right] = \quad \int dz q_\phi(z \mid x,y) \log\left(\frac{q_\phi(z \mid x,y)}{r_\theta(z \mid x,y)}\right). \tag{6.6}$$

As derived in [158], the quantity $\log r_\theta(x \mid y)$ could be written in terms of a KL-divergence and an ELBO term as follows,

$$\begin{aligned}\log r_\theta(x \mid y) &= \int dz q_\phi(z \mid x,y)\left[\log\left(\frac{r_{\theta_2}(x \mid y,z) r_{\theta_1}(z \mid y)}{q_\phi(z \mid x,y)}\right) + \log\left(\frac{q_\phi(z \mid x,y)}{r_\theta(z \mid x,y)}\right)\right] \\ &= \mathrm{ELBO} + \mathrm{KL}\left[q_\phi(z \mid x,y) \| r_\theta(z \mid x,y)\right].\end{aligned} \tag{6.7}$$

Since the KL-divergence is non-negative, we have

$$\log r_\theta(x \mid y) \geq \ \mathrm{ELBO}\ . \tag{6.8}$$

The ELBO term could be further expressed as a reconstruction loss term L and another KL-divergence between q_ϕ and r_{θ_1}

$$H \leq -\int dx p(x) \int dy p(y \mid x)[\overbrace{\mathrm{E}_{q_\phi(z|x,y)}\left[\log r_{\theta_2}(x \mid z,y)\right]}^{L} - \overbrace{\mathrm{KL}\left[q_\phi(z \mid x,y) \| \mid r_{\theta_1}(z \mid y)\right]}^{\mathrm{KL}}]. \tag{6.9}$$

In practice, Eq. (6.9) could be approximated as a sum over a batch of N_b draws from the prior $p(x)$, the likelihood $p(y \mid x)$ and the recognition function q_ϕ.

$$H \lesssim \frac{1}{N} \sum_{n=1}^{N_\mathrm{b}} \left[-\log r_{\theta_2}\left(x_n \mid z_n, y_n\right) + \mathrm{KL}\left[q_\phi\left(z \mid x_n, y_n\right) \| r_{\theta_1}\left(z \mid y_n\right)\right]\right], \tag{6.10}$$

in which the reconstruction cost L measures how well the decoder predicts the true signal parameters x, and the KL-divergence cost measures the similarity between the distributions modelled by the encoder and recognition networks.

6.2.2 Model Configuration

The CVAE model configuration employed in this project adopted the model used in [158]. We will give a brief overview of this model in this section. There are three components consisting CVAE, encoder network r_{θ_1}, decoder network r_{θ_2}, and recognition network q_ϕ. The structure of the training process is also represented graphically in figure 6.1.

The vector input for the multichannel (each channel represents a different GW detector) 1-dimensional time-series data y is first processed by the encoder network r_{θ_1}. The input passes through a sequence of one-dimensional convolutional and fully connected layers, output parameters (means, log-variances, and component weights) of a diagonal n_z-dimensional Gaussian mixture model in the latent space. The reason for using this mixture model representation stems from the multi-modal nature of GW posterior distributions. By utilizing this flexibility, the encoder network could try to represent the time-series data as belonging to several potential latent space regions. In this project, we first choose the number of modes in the latent space to be $M = 4$, since we intend to start from 4-parameter inference. The dimension of the latent space adopted the choice in [158], which is $n_z = 10$. Note that there are limitations to this flexibility and the network needs to be improved by adding more

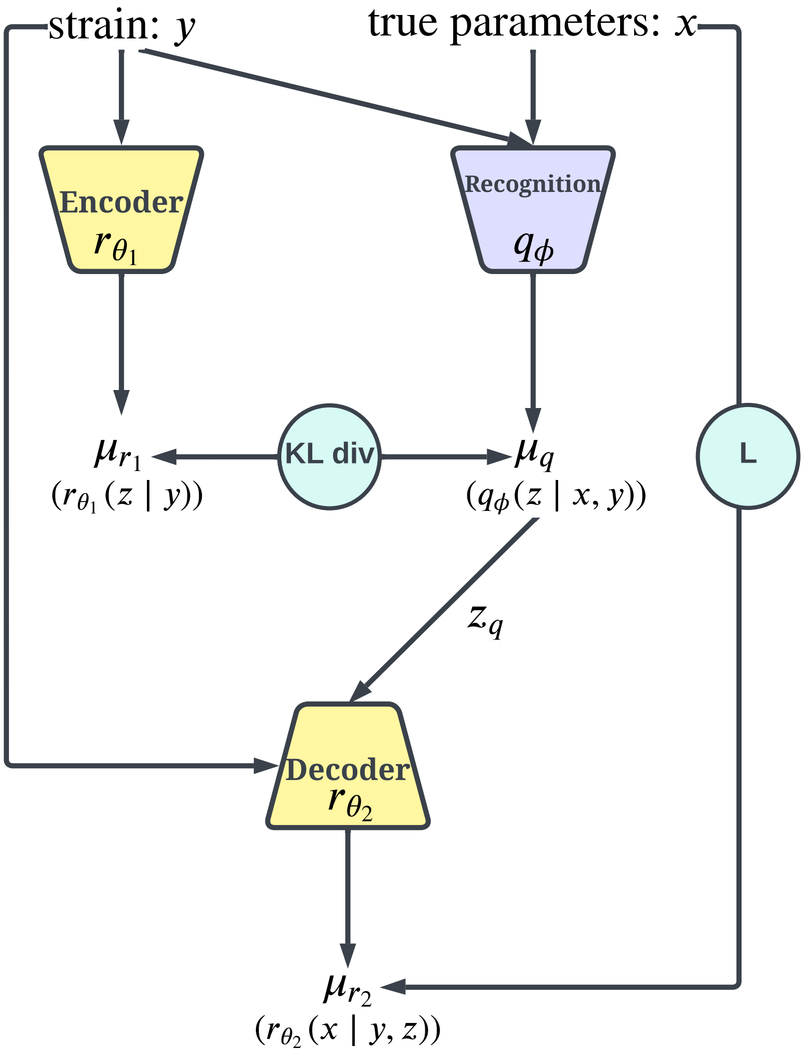

Figure 6.1: Configuration of the CVAE neural network training process. The recognition network receives both noisy GW signals y and their corresponding true parameters x as inputs, while only y is fed to the encoder network. The recognition network outputs a latent space representation $q_\phi(z \mid x, y)$, and is compared with encoder output distribution $r_{\theta_1}(z \mid y)$ using the KL-divergence, which forms one component of the total cost function. One sample z_q from the q_ϕ latent space representation is generated and passed to the decoder network r_{θ_2} together with the input data y. The output of the decoder represents a distribution in the physical parameter space, from which the other cost component L is computed by evaluating this distribution at the location of the injection input x.

features.

The recognition network, q_ϕ, exhibits similarities with the encoder network, with only two notable distinctions. First, the network takes the time-series input y and the true injection parameters x as inputs. Note that only the input y undergoes those convolutional layer processing. Following the final convolutional layer, which flattens the output, the x injection parameters are appended. The resulting compound time-series data or feature space, along with the true signal parameters, undergoes further processing via the remaining fully-connected layers. Secondly, the network output specifies a single-modal diagonal n_z-dimensional Gaussian. These parameters include n_z means and log-covariances. This is because the q_ϕ distribution is conditional on the true injection values, so it would contain information on which mode in the latent space a particular time-series should belong to.

The decoder network r_{θ_2} shares an identical structure to that of the encoder network, differing mainly in their respective outputs. In particular, the decoder output represents the parameters governing an n_x-dimensional distribution in the physical parameter space (n_x denotes the number of physical parameters we intend to infer).

The encoder, decoder, and recognition networks are trained simultaneously. The encoder takes time-series y as input and outputs a set of variables μ_{r_1} which defines a Gaussian mixture distribution in the latent space. At the same time, the recognition encoder takes both y and the injection parameters x and outputs an uncorrelated uni-mode Gaussian distribution defined by μ_q. A sample z_q is then drawn from the distribution μ_q, and is passed to the decoder r_{θ_2}, along with y. The decoder outputs a set of parameters μ_{θ_2} that define a distribution in the physical space. As for the loss function, 1) the KL-divergence is computed between the encoder output distribution $r_{\theta_1}(z \mid y)$ and recognition output $q_\phi(z \mid x, y)$. Note that in this case, since $r_{\theta_1}(z \mid y)$ is not Gaussian, the KL-divergence could not be computed analytically. A single Monte Carlo sample integration is used to compute the KL-divergence, and an average is taken over the batch of input data; 2) the first term in the loss function, called reconstruction loss, is computed by evaluating the probability density given by μ_{θ_2} at the true x training value. Same with the KL-divergence, the average is taken over the batch of the input data. The two loss components are summed, and all trainable parameters are updated according to the gradient of the loss with respect to these network parameters.

As for the testing procedure, we only keep the encoder and decoder components. A test sample y, independent of training sets, will be fed into the encoder, from which a latent distribution parameterized by μ_{r_1} will be obtained. We then repeatedly draw samples z_{r_1} from the latent distribution and feed these samples along with the original y data into the decoder. For each latent space sample input, the decoder outputs a distribution in the physical parameter space, and a random x realization will be drawn from this distribution. Each x realization corresponds to a latent space sample z_{r_1}. A histogram of these x realizations would give us the final posterior distribution $r_\theta(x \mid y)$.

6.3 Training Results

As the first step before using CVAE to infer non-GR parameters in GW strain data, we need to reproduce the training results shown in previous literature [158] within GR, which is a BBH signal parameter estimation, to make sure our code works in GR. For this benchmark analysis, we assume four parameters (within GR) are unknown: the component masses m_1, m_2, the luminosity distance d_L, and the time of coalescence t_c. Each parameter has a uniform prior with fixed ranges shown in Tab. 6.1.

Parameter name	symbol	min	max
primary mass $[M_\odot]$	m_1	35	80
secondary mass $[M_\odot]$	m_2	35	80
luminosity distance [Gpc]	d_{L}	1	3
time of coalescence $[s]$	t_c	0.65	0.85

Table 6.1: Prior boundaries used in the BBH signal parameters for the CVAE training and testing.

We use a sampling frequency of 1024 Hz and a duration of 1 second time series signal, with a minimum cutoff frequency to be 20 Hz. The waveform template model is IMRPhenomPv2 [289]. We used a total of 10^6 training samples to cover the BBH parameter space we wish to perform inference on. Every time a training sample is used, a random Gaussian noise realization is given to make the network adapt to noisy strain data. We chose a batch size of 512 with a learning rate of 10^{-4}, and trained the CVAE network for 490 epochs. In figure 6.2, we used a test case to show how CVAE's performance improved as training epochs increase. This is more obvious for the primary mass and time of coalescence inferences, while for secondary mass and luminosity distance, the improvement in performance is not significant.

We also used the same test case to compare with the results given by Dynesty [151] sampler in `Bilby` [290], which is shown in figure 6.3. In the Dynesty sampling, we used five walkers in the sampling process. We extract 2000 samples from the posterior on the 4 physical parameters for the trained model and Dynesty sampler. CVAE is more efficient in producing the posterior distribution, which has an approximate 100 times speedup compared to the Dynesty sampler. For the posterior distribution for parameters m_1, m_2 and t_c, we can see that the distributions given by the neural network are more inclined to center around those true injection values, while also maintaining a tighter constraint on some of the target variables, e.g. m_1 and m_2.

While CVAE has achieved reasonable results compared to the benchmark methods, there are some issues that need to be resolved. One significant problem is that CVAE's posterior distributions tend to exhibit a Gaussian-like behavior, whereas actual sampling results demonstrate clear signs of non-Gaussian features. This issue stems from minimizing the KL-divergence during training. Specifically, when computing the KL-divergence, we compare a multi-modal Gaussian mixture distribution generated by the decoder network with a uni-modal Gaussian distribution generated by the recognition network. The multi-modal feature of the mixture distribution is expected to capture the non-Gaussian aspect of the true distribution. However, during training, the KL-divergence collapses quickly to a very small value (approximately

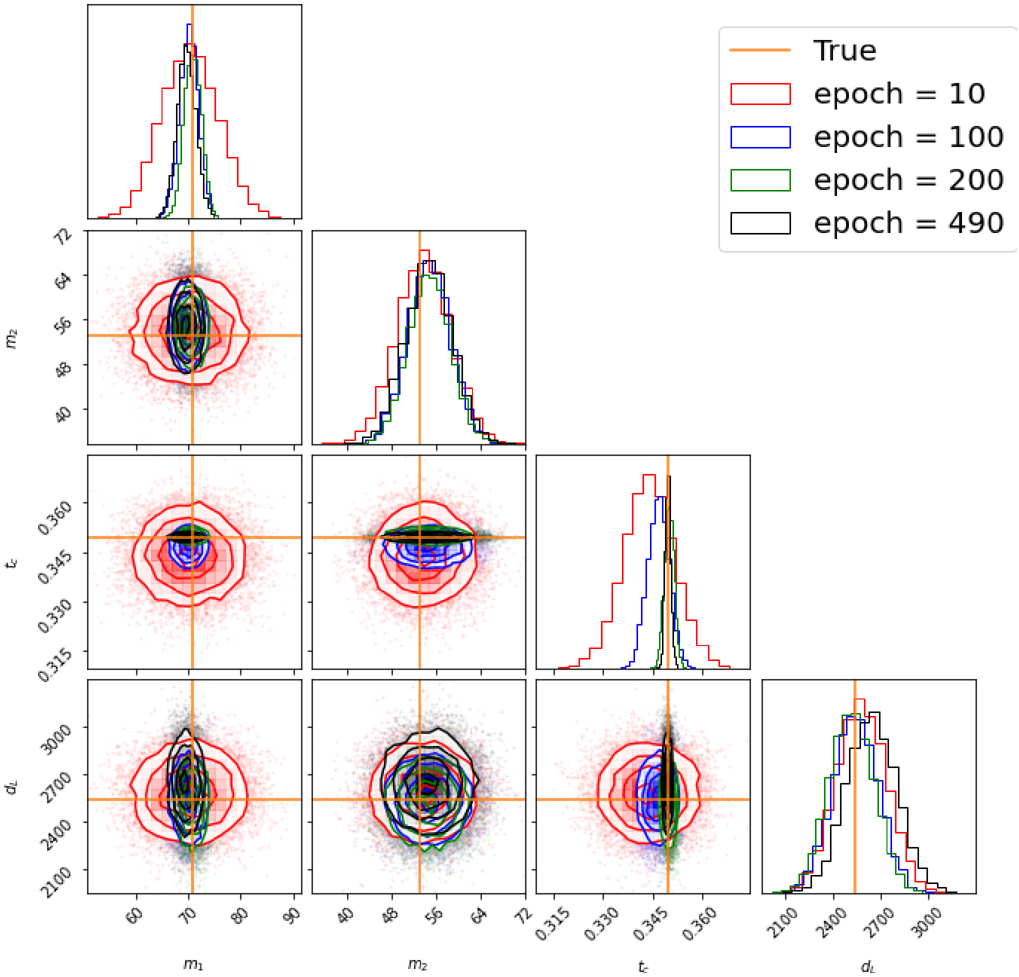

Figure 6.2: Corner plot showing 2 and 1-dimensional marginalized posterior distributions for one example test case with increasing training epochs. The true injection value is given in orange lines.

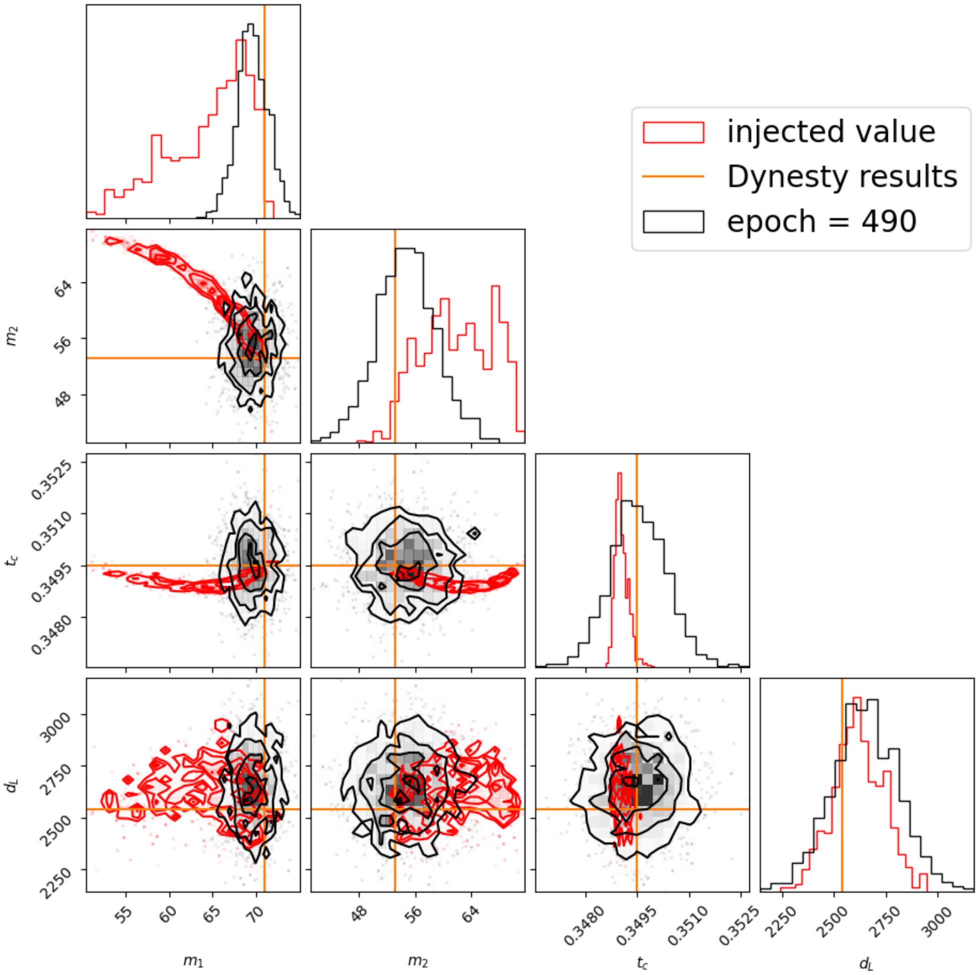

Figure 6.3: Similar to Fig. 6.2, but this time the comparison is between CVAE results and the benchmark sampling results using Dynesty.

10^{-6}), leading to a high suppression in the multi-modal feature and resulting in only one mode in the mixture dominating the distribution. We are currently working to address this issue and will discuss a possible improvement plan in the next section.

6.4 Future directions: CVAE with normalizing flows

Green et al. [160] proposed a novel approach to enhance the flexibility of modeling GW parameter estimation posterior distributions. Specifically, they introduced a combined model that integrates normalizing flow [291–293] with CVAE. The incorporation of normalizing flow within the model framework offers a more comprehensive strategy for achieving a flexible variational inference of posteriors over latent variables.

Let us first briefly introduce the concept of normalizing flows here. Normalizing flows refer to a type of transformation applied to probability densities that involve a sequence of invertible mappings. By repeatedly applying the rule for change of variables through this sequence, the initial density "flows" through the mappings, ultimately resulting in a valid probability distribution. This property of obtaining a valid probability distribution through a sequence of invertible mappings is what characterizes the "normalizing" aspect of this type of flow. A normalizing flow represents the distribution in terms of a mapping $f_d : u \mapsto \theta$ from simpler distributions. Figure 6.4 shows a more detailed description of how this certain mapping works. The mapping f_d is invertible and has a simple Jacobian determinant, which makes the distribution $q(\theta|d)$ to have fast sampling and density evaluation. Thus, one could start from a simple standard normal distribution and obtain a more complex distribution

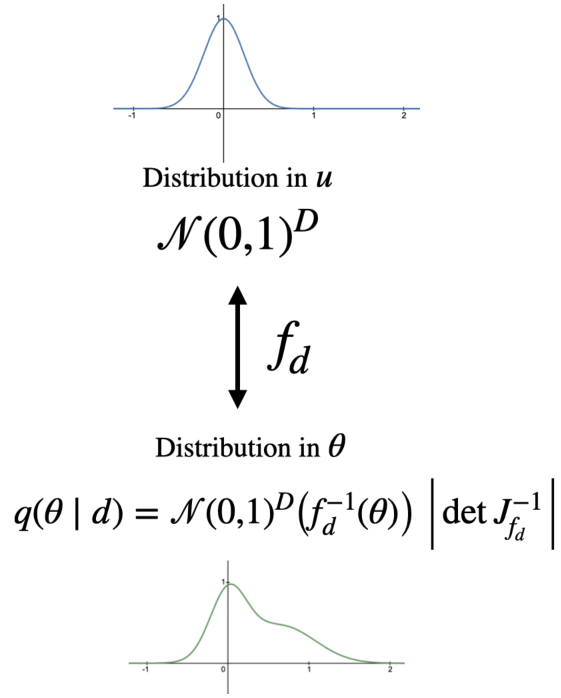

Figure 6.4: A diagram showing how normalizing flow works.

by applying a normalizing flow.

Green et al. first came up with the application of normalizing flow to the modeling of GW posterior distributions in [160]. By integrating normalizing flows within the encoder, decoder, and recognition networks, they significantly enhanced the versatility of CVAE, thereby introducing the autoregressive CVAE. As in [158], they experimented with the new network on BBH waveforms with added noise drawn from a stationary Gaussian distribution with a fixed power spectral density. The autoregressive CVAE effectively modeled the multimodality present in ϕ_0 posterior distribution, a characteristic unattainable by CVAE alone. This breakthrough has proven extremely valuable in addressing the challenges noted in the preceding section, and our ongoing work involves the integration of this normalizing flow component within our CVAE framework.

In conclusion, this project is still an ongoing endeavor, with considerable progress yet to be made before the CVAE network can be effectively utilized for parameter estimation beyond GR. The successful implementation of CVAE for the four-parameter estimation of BBH signals within the GR framework has demonstrated acceptable precision and enhanced efficiency. Our next step is combining the normalizing flows into the current CVAE to accurately capture multi-modal characteristics, as exhibited by traditional Bayesian sampling techniques. The pursuit of this objective is currently underway in our research.

Appendix

Appendix A

Additional Scalar-tensor Theory and Phenomenological Model

In this appendix, we present the mapping between the modified GW propagation parameters (Ξ_0, n) to additional scalar-tensor theories and phenomenological models, and present future projected bounds on these theories/models through tidal measurement of BNS mergers. The mapping is summarized in Table 4.1.

- *Designer $f(R)$ gravity* [220]: Other than the HS model, an interesting $f(R)$ gravity model includes the designer model that exactly reproduces the standard cosmological expansion history. The model is characterized by the Compton wavelength parameter

  $$B_0 \equiv \left. \frac{H f_R'}{H'(1+f_R)} \right|_0 \approx -2.1\Omega_M^{-0.76} f_{R0} \,. \tag{A.1}$$

  The top panel of Fig. A.1 presents the bound on $|B_0|$ with GWs from BNSs using a three-year observation of a multi-band network as a function of $\alpha_{\rm em}$. We used $n = 2.34$, which is close to $n = 2.5$ in Fig. 1.2 and thus follows the

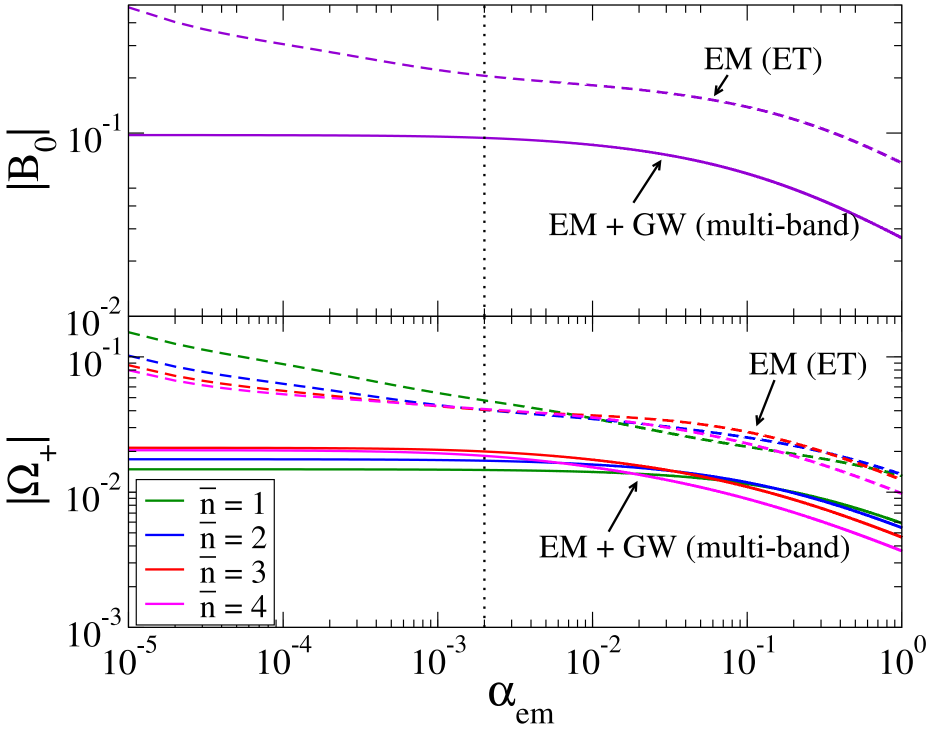

Figure A.1: Similar to Fig. 4.6 but for the bounds on the Compton wavelength parameter $|B_0|$ in the designer $f(R)$ gravity (top) and $|\Omega_+|$ in the power law $M_{\rm eff}$ formalism (bottom).

same trend. Observe that the bounds on B_0 increases by a factor of $2-5$ if we add BNS events without EM counterparts.

- *power law* $M_{\rm eff}$: On top of the phenomenological models for α_M, we consider a phenomenological model on the effective Planck mass $M_{\rm eff}$. As an example, we consider a simple power law model for $M^2_{\rm eff}$ given by [223]

$$M^2_{\rm eff} = \frac{1}{8\pi}\left(1+\Omega_+ a^{\bar{n}}\right) , \tag{A.2}$$

where Ω_+ and $\bar{n}$ are constant parameters. α_M in this model is given by

$$\alpha_M = \frac{\bar{n}\Omega_+ a^{\bar{n}-1}}{1+\Omega_+ a^{\bar{n}}} . \tag{A.3}$$

Using the mapping in Table 4.1, we present in the bottom panel of Fig. A.1 the projected bounds on $|\Omega_+|$ for BNSs with and without EM counterparts for various $\bar{n}$. Observe that the addition of BNSs without EM counterparts improve the bound by an order of magnitude for small $\alpha_{\rm em}$ and $\bar{n}$. On the other hand, the improvement is by a factor of a few irrespective of $\bar{n}$ when $\alpha_{\rm em} \sim 1$.

Appendix B

Observation time and EoS dependence on $\Delta\Xi_0$

In this appendix, we carry out some additional investigations on the measurability of Ξ_0 with multi-band GW observations. Figure B.1 presents how $\Delta\Xi_0$ depends on the observation period. Notice that the observation time has the most significant effect when $\alpha_{\rm em} \sim 1$. For this case, the error on the luminosity distance measurement is dominated by the lensing that is independent of the observation time. Moreover, the prior on the second Fisher matrix $\tilde{F}_{ij}$ in Eq. (4.37) is less important and the measurability scales with $T_{\rm obs}^{-1/2}$ since the number of BNS events increases linearly with $T_{\rm obs}$ (see Eq. (4.35)). On the other hand, for smaller $\alpha_{\rm em}$, the prior on $\tilde{F}_{ij}$ becomes more important and the above scaling breaks down. Notice also that the observation time has a larger effect on the case with all BNSs (with and without EM counterparts) than BNSs with EM counterparts only. This is because for the former, the error on the luminosity distance measurement is dominated by the redshift uncertainty, and a longer observation time helps more to break the degeneracy between the redshift and other parameters.

Figure B.2 presents $\Delta\Xi_0$ with multi-band observations for the three representative EoSs. For the case with BNSs with EM counterparts alone, EoS only affects the first Fisher matrix $\tilde{\Gamma}_{ij}$ through the maximum frequency cutoff. Since the effect is small, we only consider the SLy EoS for this case. Notice that the measurability of Ξ_0 improves as we make the EoS stiffer. This is as expected from the measurability of the redshift from Fig. 4.3.

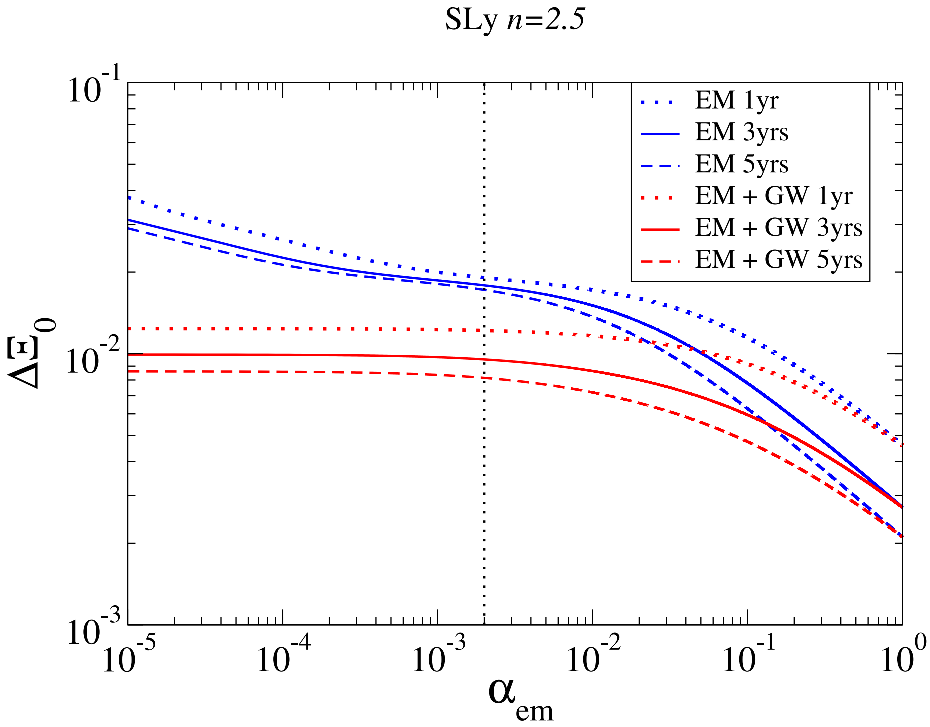

Figure B.1: Measurement errors on the modified GW propagation parameter Ξ_0 as a function of $\alpha_{\rm em}$ for three different observation periods. We consider BNSs with redshift identified from EM counterparts only (blue), as well as those with redshift identification by EM and GW observations (red). We fix $n = 2.5$, choose the SLy EoS and consider multi-band observations.

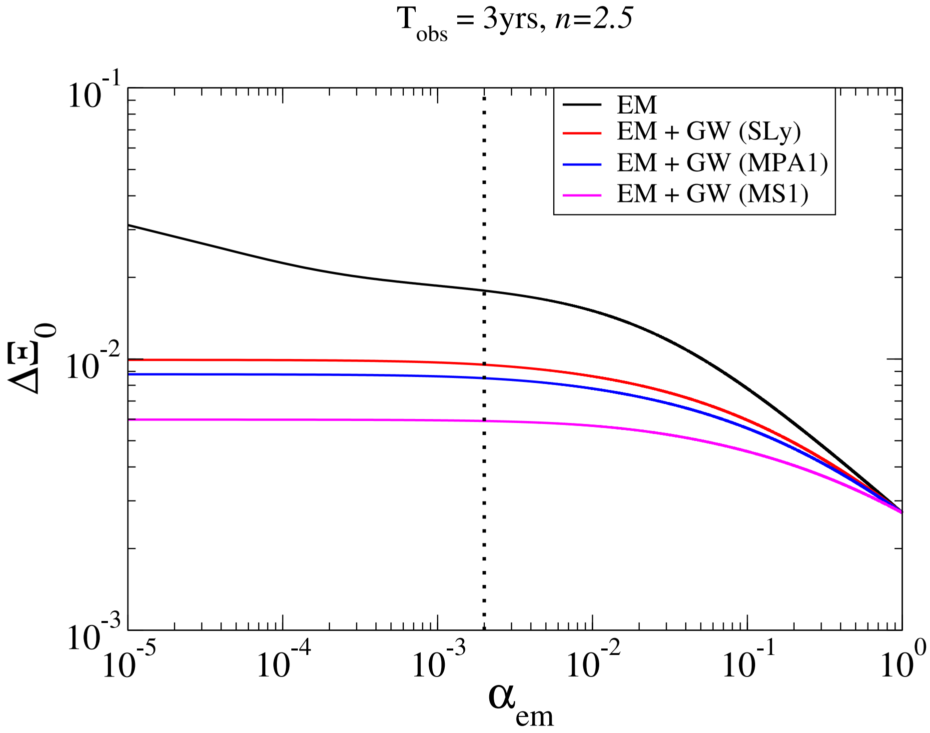

Figure B.2: Similar to Fig. B.1 but showing how $\Delta\Xi_0$ varies with EoSs. We fix $T_{\rm obs} = 3$yrs and $n = 2.5$.

Appendix C

Inclusion of $\tilde{\lambda}_0$ and $\tilde{\lambda}_1$

In this appendix, we study how the imperfect knowledge of the EOS may affect the measurability of the redshift. For this, we include $\tilde{\lambda}_0$ and $\tilde{\lambda}_1$ into a search parameter set θ^i in Eq. (4.27) for the first Fisher analysis:

$$\theta^i = \left(\ln\mathcal{M}_z, \eta, t_c, \phi_c, \ln A, \ln\tilde{\lambda}_0, \ln\tilde{\lambda}_1, \ln z\right). \tag{C.1}$$

For simplicity, we follow [227, 294] and assume a Gaussian prior with standard deviations $\sigma_{\tilde{\lambda}_0}$ and $\sigma_{\tilde{\lambda}_1}$. The effective Fisher matrix now becomes

$$\tilde{\Gamma}_{ij} = \sum_A \Gamma_{ij}^{(A)} + \frac{\delta_{ij}}{\left(\sigma_{\theta^i}\right)^2}. \tag{C.2}$$

To give an example, we consider a prior for $\tilde{\lambda}_0$ and $\tilde{\lambda}_1$ that corresponds to measuring them through a network of LIGO Hanford/Livingston and Virgo (HLV) shown in Table C.1 that is taken from [224]. Following this reference, we assume that all BNSs with $z < 0.1$ detected through such a network has EM counterparts and can be used to measure $\tilde{\lambda}_0$ and $\tilde{\lambda}_1$. This is somewhat optimistic, though the authors in [224] found that the measurability of these tidal parameters do not change much even if

	SLy		MS1	
	pessimistic (30 BNSs)	optimistic (384 BNSs)	pessimistic (30 BNSs)	optimistic (384 BNSs)
$\tilde{\lambda}_0$	4.46		12.41	
$\sigma_{\tilde{\lambda}_0}$	0.039	0.014	0.029	0.009
$\tilde{\lambda}_1$	-1.99		-3.35	
$\sigma_{\tilde{\lambda}_1}$	0.025	0.0125	0.019	0.009

Table C.1: Values of $\tilde{\lambda}_0$ [10^{36}gcm^{2}s^2], $\tilde{\lambda}_1$ [(10^{36}gcm^{2}s$^2/M_\odot$)] and their standard deviations for Gaussian priors for SLy and MS1. The priors are taken from the results of two cases under the detection of HLV in Section 5.4 in [224], the pessimistic case with 30 BNSs and the optimistic case with 384 BNSs.

one only uses BNSs with $z < 0.05$.

Figure C.1 presents the measurability of the redshift for multi-band GW observations, where $\tilde{\lambda}_0$ and $\tilde{\lambda}_1$ are included in the search parameter for Fisher analyses for the SLy and MS1 EoSs. We consider a pessimistic (optimistic) case with 30 (384) detected BNSs with $z < 0.1$ for a 3-yr observation. For reference, we show the result without $\tilde{\lambda}_0$ and $\tilde{\lambda}_1$ in the search parameter set from Fig. 4.3. Notice that the uncertainty in the EoS affects the measurability of the redshift only for BNSs with low z. Moreover, such an uncertainty on the EoS will be reduced if one uses ET instead of LHV. We thus expect the effect of imperfect knowledge of the EoS to be small, and neglect them in the main text.

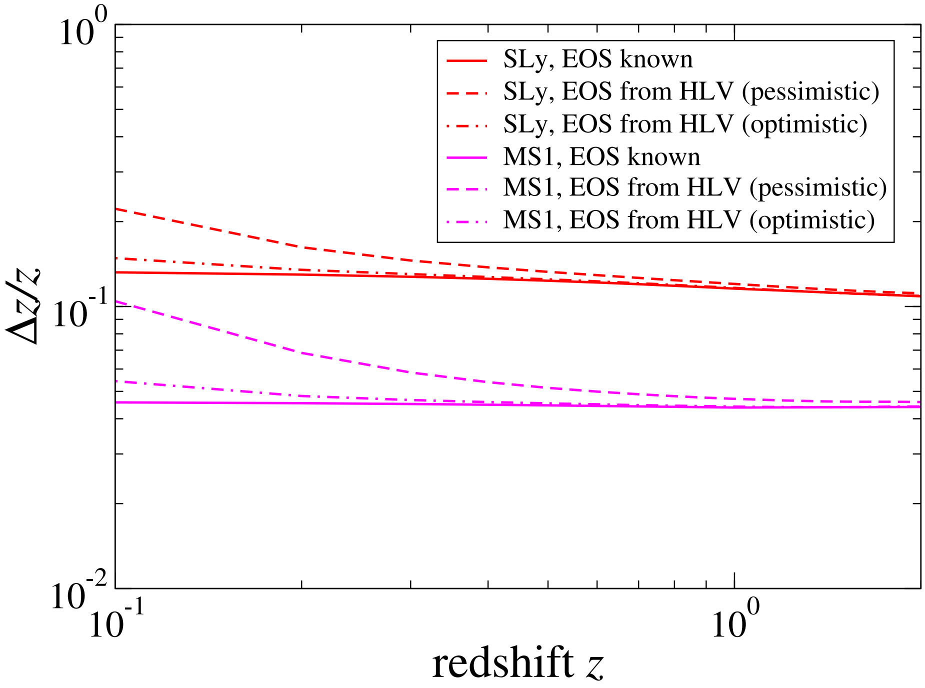

Figure C.1: The measurability of the redshift with multi-band GW observations for the case where (i) the EoS is known *a priori* and (ii) $\tilde{\lambda}_0$ and $\tilde{\lambda}_1$ are obtained from a network of HLV observations [224]. For the latter, we consider both pessimistic (30 BNSs) and optimistic cases (384 BNSs) for 3-yr observations. We show the results for SLy (soft) and MS1 (stiff) EoS.

Appendix D

Degeneracy between luminosity distance and binary orientation

In this appendix, we estimate the amount of degeneracy between the luminosity distance and binary orientation for multi-band observations. Since the measurability of the luminosity distance for the multi-band observation is mostly determined by observations with DECIGO (due to its high SNR and a large effective baseline of 1AU), we focus on the latter for simplicity. The binary inclination varies over time due to the motion of DECIGO, and thus it is useful to work in a barycentric frame (centered at the Sun) [231,295–297]. In such a frame, we can describe the sky location of a BNS by (θ_s, ϕ_s) and the direction of its orbital angular momentum as (θ_L, ϕ_L). Following [297], we perform a new Fisher analysis with search parameters given by[1]

$$\theta^i = (\ln\mathcal{M}_z, \eta, t_c, \phi_c, \ln A, \theta_s, \phi_s, \theta_L, \phi_L)\,, \tag{D.1}$$

---

[1] In this appendix, we do not include z since we focus on DECIGO which is insensitive to the effect close to merger. This does not affect the luminosity distance measurement since the amplitude parameters are mostly uncorrelated with the phase parameters.

and we take into account the motion of the detectors. We use a restricted PN waveform where we only consider the leading Newtonian contribution for the amplitude while we include up to 2PN order in the phase. We carry out a Monte Carlo simulation in which we consider 10^3 BNSs at $z = 1$ with the angle parameters randomly drawn from a uniform distribution in $\cos\theta_s$, ϕ_s, $\cos\theta_L$ and ϕ_L [231, 296, 297].

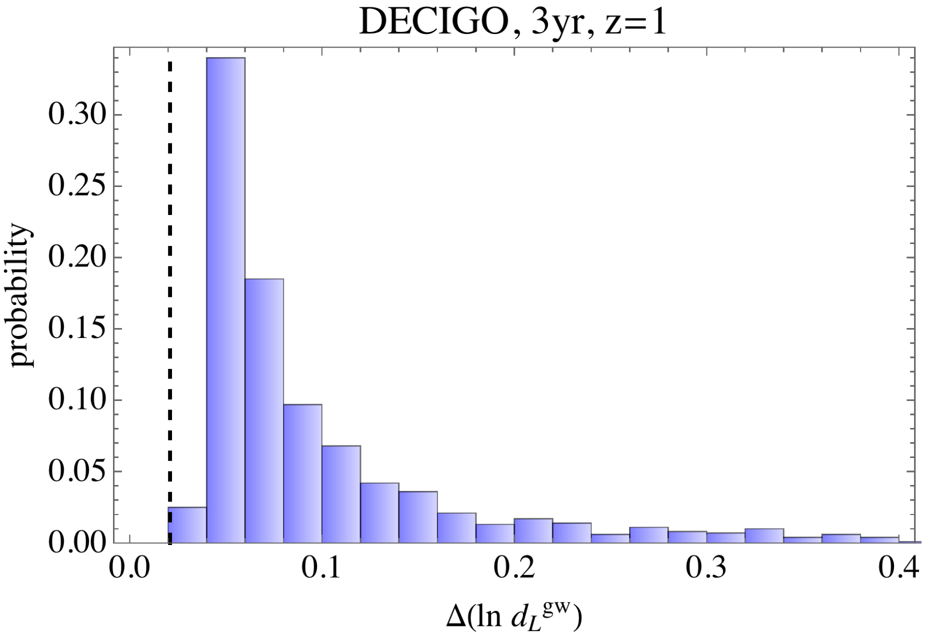

Figure D.1: Histogram for the probability of the luminosity distance measurability with DECIGO for at $z = 1$ whose sky location and orientation are randomly distributed. The black dashed vertical line shows the measurability with the sky-averaged case. Notice that most of the binaries have the fractional error of less than 10% even if we account for the degeneracy between d_L^{gw} and binary orientations.

Figure D.1 presents the distribution of the luminosity distance measurability for a 3-yr observation with DECIGO for BNSs at $z = 1$. For comparison, we also show the measurability when we use a sky-averaged waveform as done in the main part of this work, which roughly agrees with the blue solid curve in Fig. 4.4 at $z = 1$ (suggesting that the error is indeed determined from the DECIGO measurement for multi-band observations). Notice that although the sky-averaged analysis underestimates the error, the measurement error is below 10% for most of BNSs and thus does not exceed the error on the luminosity distance from the redshift measurement. This shows that the bound on Ξ_0 for multi-band observations found in Chap. 4 through the sky-averaged analysis will not be affected much even if we include the effect of binary sky location and orientation.

Appendix E

EdGB Corrections to Gravitational Waveforms

In this appendix, we explain how to map the waveform (for non-spinning BBHs) in scalar-tensor theories [255] to that in EdGB gravity. The former is valid to 2PN order higher than the leading for each of tensor and scalar emission.

The waveform in scalar-tensor theories is derived in the Jordan frame, while EdGB gravity is in the Einstein frame. Therefore, we first turn the former into the Einstein frame. This can be realized by using the mapping provided in Appendix A of [255]. After this transformation, the waveform is given in terms of the scalar charge α_A and its derivative β_A for the Ath body.

The next step is to find these charges in EdGB gravity and substitute this into the waveform. We can compute these following [298] which uses a slightly different convention for sGB gravity:

$$S = \frac{1}{16\pi} \int d^4x \sqrt{-g} \left[R - 2(\nabla\varphi)^2 + \alpha_{\text{GB}} \bar{f}(\varphi) \mathcal{R}^2_{\text{GB}} \right] + S_m \,. \tag{E.1}$$

One can perform the following rescaling in the scalar field φ and the identification of the function $\bar{f}(\varphi)$ to recover the action in Eq. (5.5):

$$\bar{f}(\varphi) = 2\sqrt{16\pi}\varphi\,, \quad \varphi = \frac{\sqrt{16\pi}}{2}\phi\,. \tag{E.2}$$

From this, α_A and β_A for a non-rotating BH to leading order in $\alpha_{\rm GB}$ are given by:

$$\alpha_A^{\rm BH} = -\frac{\alpha_{\rm GB}\bar{f}'(\varphi_0)}{2m_A^2} = -\frac{\sqrt{16\pi}\alpha_{\rm GB}}{m_A^2}\,, \tag{E.3}$$

$$\beta_A^{\rm BH} = -\frac{\alpha_{\rm GB}^2\bar{f}'(\varphi_0)^2}{2m_A^2} = -\frac{32\pi\alpha_{\rm GB}^2}{m_A^2}\,, \tag{E.4}$$

where φ_0 is the asymptotic value of the scalar field φ at infinity. When substituting these into the waveform expression, the terms with β_A enter at $\mathcal{O}(\alpha_{\rm GB}^4)$ and are negligible. For α_A, we add the spin dependence as:

$$\alpha_A^{\rm BH} = -\frac{\sqrt{16\pi}s_A\alpha_{\rm GB}}{m_A^2}\,, \tag{E.5}$$

where the spin dependent factor is given by: [120, 258]

$$s_A = 2\frac{\sqrt{1-\chi_A^2}-1+\chi_A^2}{\chi_A^2}\,. \tag{E.6}$$

This reduces to $s_A^{\rm BH} \to 1$ in the limit $\chi_A \to 0$. For NSs, $\alpha_A^{\rm NS} = \mathcal{O}(\alpha_{\rm GB}^3)$ and is negligible while $\beta_A^{\rm NS}$ has not been computed. Though we expect the $\alpha_{\rm GB}$ dependence to be the same as BH and ignore such terms in the waveform.

Using these charge expressions in the dominant harmonics ($\ell = m = 2$) of the waveform and keeping only to $\mathcal{O}(\alpha_{\rm GB}^2)$, EdGB corrections to the waveform can be expressed as in Eq. (5.7) with the coefficients given as follows:

$$c_{-1} = -\frac{5\pi}{448}\frac{(m_1^2 s_2 - m_2^2 s_1)^2}{\eta^5 M^4}\,, \tag{E.7}$$

$$c_0 = -\frac{5\pi}{43008}\frac{(659 + 728\eta)\left(m_1^2 s_2 - m_2^2 s_1\right)^2}{\eta^5 M^4} - \frac{5\pi}{16}\frac{s_1 s_2}{\eta^3}\,, \tag{E.8}$$

$$c_{0.5} = \frac{75\pi^2}{448}\frac{(m_1^2 s_2 - m_2^2 s_1)^2}{\eta^5 M^4}\,, \tag{E.9}$$

$$\begin{aligned} c_1 = &-\frac{5\pi}{48384}\frac{\left(m_1^2 s_2 + m_2^2 s_1\right)^2 (535 + 924\eta)}{\eta^5 M^4} \\ &- \frac{25\pi}{576}\frac{\left(m_1^2 s_2 - m_2^2 s_1\right)^2}{\eta^5 M^4}\left[\frac{12497995}{1016064} - \frac{11\,(m_1 - m_2)\left(m_1^2 s_2 + m_2^2 s_1\right)}{2M\left(m_1^2 s_2 - m_2^2 s_1\right)} + \frac{15407\eta}{1440} + \frac{165\eta^2}{16}\right], \end{aligned} \tag{E.10}$$

$$c_{1.5} = \frac{\pi^2}{2}\frac{\left(m_1^2 s_2 - m_2^2 s_1\right)^2}{\eta^5 M^4} - \frac{6\pi^2 s_1 s_2}{\eta^3} - \frac{3 f_3^{\mathrm{GB}}}{32\eta}\,, \tag{E.11}$$

$$c_2 = \frac{5\pi}{32514048}\frac{1}{\eta^5 M^5}\Bigg[\left(m_1^5 s_2^2 + m_2^5 s_1^2\right)\left(-4341025 + 65553264\eta - 684432\eta^2\right).$$

$$\begin{aligned} &+ \eta M^2\left(m_1^3 s_2^2 + m_2^3 s_1^2\right)\left(20044511 + 65553264\eta - 684432\eta^2\right) \\ &+ 54\eta^2 M^5 s_1 s_2\left(12952549 - 19310256\eta - 366128\eta^2\right)\Bigg] - \frac{15 f_4^{GB}}{64\eta}. \end{aligned} \tag{E.12}$$

Here $\eta \equiv m_1 m_2/M^2$ is the symmetric mass ratio while f_3^{GB} and f_4^{GB} represent our ignorance of the correction to the tensor non-dipole emission in EdGB gravity at 1.5PN and 2PN orders[1]. Recently, Bernard et al. [299] published their work on deriving 1.5PN order correction to GWs in scalar-tensor theory, which in our context, the $f_3^{\rm GB}$ in Eq. (E.11) is found to be,

$$f_3^{\rm GB} = \frac{32\pi^2 s_1 s_2 \alpha^2}{3\eta^2 M^4} + \mathcal{O}(\alpha^3). \tag{E.13}$$

As Eq. (E.13) shows, the term related to $f_3^{\rm GB}$ actually enters the waveform at $\mathcal{O}(\alpha^4)$ when one also takes into account the α^2 factor in Eq. (5.7). The above corrections can be mapped to the parameterized post-Einsteinian (PPE) framework [169,300,301] of

$$\delta\Psi = \sum_i \beta_i^{\rm PPE} v^{-5+2i}\,, \tag{E.14}$$

with

$$\beta_i^{\rm PPE} = \frac{\alpha_{\rm GB}^2}{M^4} c_i\,. \tag{E.15}$$

The leading -1PN term (c_{-1} or $\beta_{-1}^{\rm PPE}$) derived here agrees with those found in [120, 134].

Figure E.1 presents each PN correction term in the phase against the GW frequency f for GW200115, together with the leading GR term. We chose $\sqrt{\alpha_{\rm GB}} =$ 1.33km that is the 90% credible limit found through our Bayesian inference in Table 5.1. Notice that the EdGB corrections are subdominant to GR by at least an order of magnitude. Notice also that the leading EdGB correction at -1PN order dominates higher PN contributions at $f \lesssim 200$Hz and the latter becomes only important

---

[1] We have replaced $f_i^{\rm ST}$ in [255] to $(\alpha_{\rm GB}^2/M^4) f_i^{\rm GB}$ for $i = 3, 4$.

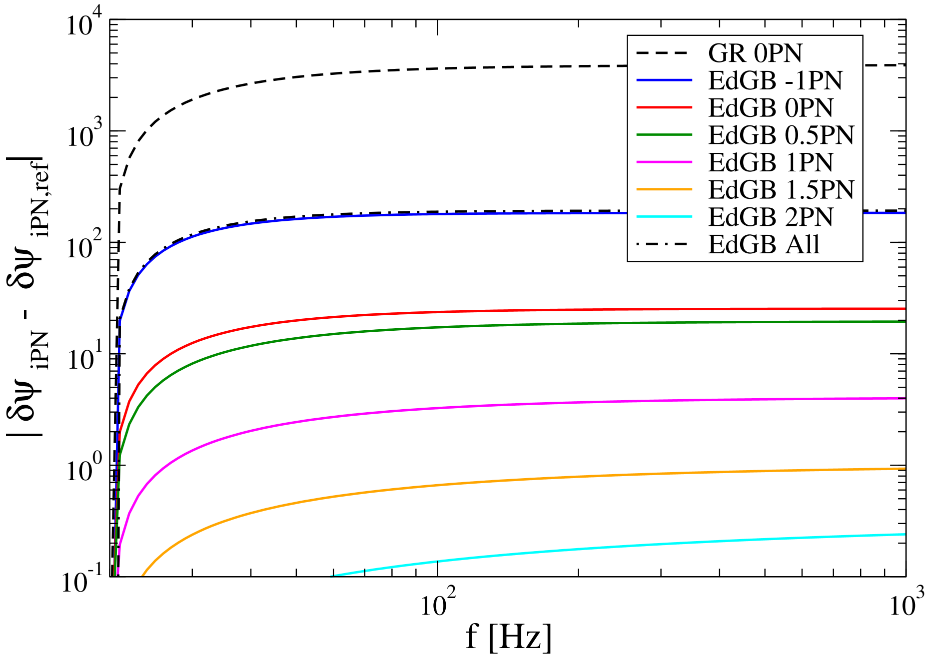

Figure E.1: Comparison of EdGB corrections to the phase entering at different PN orders as a function of the GW frequency. We also present the leading phase in GR and the contribution from all of the EdGB corrections combined. For each contribution, we show the phase relative to that at a reference frequency chosen to be 20Hz. We chose $(m_1, m_2) = (5.9, 1.4)M_\odot$ and $(\chi_1, \chi_2) = (0.31, 0)$, corresponding to GW200115, and $\sqrt{\alpha_{\mathrm{GB}}} = 1.33\,\mathrm{km}$ that is the 90% credible limit found through our Bayesian inference (see Table 5.1).

when the frequency becomes high (though the noise becomes larger as the frequency becomes higher), which explains why higher PN corrections do not affect the bound on $\sqrt{\alpha_{\mathrm{GB}}}$ much. It is interesting to note that for $f \gtrsim$ 200Hz, the EdGB phase is dominated by the contribution at 1.5PN order, though the phase is still incomplete at this order (we have set the unknown contributions f_3^{GB} and f_4^{GB} to 0 in Fig. E.1).

Let us comment on up to which PN order the above waveform corrections are complete. The α_{GB} dependence in the above corrections enter only through the scalar charges α_A. There are other contributions to the waveform where α_{GB} appears explicitly, though such contributions enter at 3PN order and are negligible for our purpose [2]. For non-spinning binaries, they are complete up to 1PN order. The expressions at 1.5PN and 2PN include currently unknown f_3^{GB} and f_4^{GB} but they also have other missing contributions, such as the scalar dipole radiation at 1.5PN and 2PN orders (which correspond to 2.5PN and 3PN relative to the leading −1PN contribution) and the correction to the binding energy or Kepler's law at 3PN that couples to the −1PN dipole radiation and enter at 2PN in the waveform. For spinning binaries, the waveform is complete only up to 0PN order, as the effect of spins are only included through the scalar charges α_A. Missing contributions include e.g. a spin-orbital coupling in the binding energy at 1.5PN order that couples with the leading dipole radiation to enter at 0.5PN in the waveform.

We end by comparing the 0PN corrections found here with different functional forms considered in [127]. Using Eqs. (E.7) and (E.8), the 0PN correction to the phase can be expressed as:

$$\delta\Psi_{\mathrm{0PN}} = \frac{659+728\eta}{96} v^2 \delta\Psi_{-\mathrm{1PN}} + \frac{5\pi}{16}\frac{s_1 s_2}{\eta^3}\frac{\alpha_{\mathrm{GB}}^2}{M^4} v^{-5} \,. \tag{E.16}$$

The first term is similar to one of the functional forms considered in [127]:

$$\delta\Psi_{\mathrm{0PN}}^{(\mathrm{PNSY},1)} = \frac{5}{756}(743+924\eta)\gamma\, u^2\, \delta\Psi_{-\mathrm{1PN}} \,, \tag{E.17}$$

---

[2] We count the PN order in powers of v/c while Shilarirou et al. [253, 254] counts in powers of $1/c$. With the latter counting, the α_{GB} dependence other than scalar charges enters at 1PN.

where γ is a constant that does not depend on binary parameters, $u \equiv (\pi \mathcal{M} f)^{1/3}$ and the η dependence is taken from that in the phase at 1PN order in GR. The η dependence in the two expressions, however, are different. The second term in Eq. (E.16) is similar to another functional form considered in [127]:

$$\Psi_{\mathrm{0PN}}^{(\mathrm{PNSY},2)} = 16\pi \frac{\alpha_{\mathrm{GB}}^2}{M^4} \gamma u^{-5} \,, \tag{E.18}$$

though, again, the expressions are different. This is because, if one maps the second term in Eq. (E.16) to Eq. (E.18), γ depends on binary parameters through η and s_A.

Bibliography

[1] T. K. Chan, A. P. O. Chan, and P. T. Leung, "I-love relations for incompressible stars and realistic stars," *Phys. Rev. D*, vol. 91, p. 044017, Feb 2015. [Online]. Available: https://link.aps.org/doi/10.1103/PhysRevD.91.044017

[2] T. Clifton, P. G. Ferreira, A. Padilla, and C. Skordis, "Modified gravity and cosmology," *Physics Reports*, vol. 513, no. 1, pp. 1–189, 2012, modified Gravity and Cosmology. [Online]. Available: https://www.sciencedirect.com/science/article/pii/S0370157312000105

[3] A. Joyce, B. Jain, J. Khoury, and M. Trodden, "Beyond the cosmological standard model," *Physics Reports*, vol. 568, pp. 1–98, 2015, beyond the cosmological standard model. [Online]. Available: https://www.sciencedirect.com/science/article/pii/S0370157314004487

[4] B. Famaey and S. S. McGaugh, "Modified newtonian dynamics (mond): Observational phenomenology and relativistic extensions," *Living Reviews in Relativity*, vol. 15, no. 1, Sep 2012. [Online]. Available: http://dx.doi.org/10.12942/lrr-2012-10

[5] M. Milgrom, "The mond paradigm," 2008. [Online]. Available: https://arxiv.org/abs/0801.3133

[6] B. Jain and J. Khoury, "Cosmological tests of gravity," *Annals of Physics*, vol. 325, no. 7, pp. 1479–1516, 2010, july 2010 Special Issue. [Online]. Available: https://www.sciencedirect.com/science/article/pii/S0003491610000667

[7] K. Koyama, "Cosmological tests of modified gravity," *Reports on Progress in Physics*, vol. 79, no. 4, p. 046902, mar 2016. [Online]. Available: https://dx.doi.org/10.1088/0034-4885/79/4/046902

[8] V. Salvatelli, F. Piazza, and C. Marinoni, "Constraints on modified gravity from planck 2015: when the health of your theory makes the difference," *Journal of Cosmology and Astroparticle Physics*, vol. 2016, no. 09, p. 027–027, Sep 2016. [Online]. Available: http://dx.doi.org/10.1088/1475-7516/2016/09/027

[9] M. Milgrom, "Modification of the newtonian dynamics as a possible alternative to the hidden mass hypothesis/sup 1/," *Astrophys. J.; (United States)*, vol. 270:2, 7 1983. [Online]. Available: https://www.osti.gov/biblio/5668018

[10] B. P. Abbott *et al.*, "Observation of gravitational waves from a binary black hole merger," *Phys. Rev. Lett.*, vol. 116, p. 061102, Feb 2016. [Online]. Available: https://link.aps.org/doi/10.1103/PhysRevLett.116.061102

[11] B. P. Abbott *et al.*, “GW170817: Observation of Gravitational Waves from a Binary Neutron Star Inspiral,” *Phys. Rev. Lett.*, vol. 119, no. 16, p. 161101, 2017, 1710.05832.

[12] B. P. Abbott *et al.*, “Gravitational Waves and Gamma-rays from a Binary Neutron Star Merger: GW170817 and GRB 170817A,” *Astrophys. J.*, vol. 848, no. 2, p. L13, 2017, 1710.05834.

[13] T. L. S. Collaboration, the Virgo Collaboration, and the KAGRA Collaboration, “Gwtc-3: Compact binary coalescences observed by ligo and virgo during the second part of the third observing run,” 2021,” 2111.03606.

[14] B. P. Abbott, R. Abbott, T. D. Abbott, S. Abraham, F. Acernese, K. Ackley, C. Adams, V. B. Adya, C. Affeldt, M. Agathos, and et al., “Prospects for observing and localizing gravitational-wave transients with advanced ligo, advanced virgo and kagra,” *Living Reviews in Relativity*, vol. 23, no. 1, Sep 2020. [Online]. Available: http://dx.doi.org/10.1007/s41114-020-00026-9

[15] F. Acernese, M. Agathos, K. Agatsuma, D. Aisa, N. Allemandou, A. Allocca, J. Amarni, P. Astone, G. Balestri, G. Ballardin, and et al., “Advanced virgo: a second-generation interferometric gravitational wave detector,” *Classical and Quantum Gravity*, vol. 32, no. 2, p. 024001, Dec 2014. [Online]. Available: http://dx.doi.org/10.1088/0264-9381/32/2/024001

[16] J. Aasi, B. P. Abbott, R. Abbott, T. Abbott, M. R. Abernathy, K. Ackley, C. Adams, T. Adams, P. Addesso, and et al., "Advanced ligo," *Classical and Quantum Gravity*, vol. 32, no. 7, p. 074001, Mar 2015. [Online]. Available: http://dx.doi.org/10.1088/0264-9381/32/7/074001

[17] B. Abbott, R. Abbott, T. Abbott, S. Abraham, F. Acernese, K. Ackley, C. Adams, R. Adhikari, V. Adya, C. Affeldt, and et al., "Gwtc-1: A gravitational-wave transient catalog of compact binary mergers observed by ligo and virgo during the first and second observing runs," *Physical Review X*, vol. 9, no. 3, Sep 2019. [Online]. Available: http://dx.doi.org/10.1103/PhysRevX.9.031040

[18] R. Abbott, T. Abbott, S. Abraham, F. Acernese, K. Ackley, A. Adams, C. Adams, R. Adhikari, V. Adya, C. Affeldt, and et al., "Gwtc-2: Compact binary coalescences observed by ligo and virgo during the first half of the third observing run," *Physical Review X*, vol. 11, no. 2, Jun 2021. [Online]. Available: http://dx.doi.org/10.1103/PhysRevX.11.021053

[19] T. L. S. Collaboration and the Virgo Collaboration, "Gwtc-2.1: Deep extended catalog of compact binary coalescences observed by ligo and virgo during the first half of the third observing run," 2021," 2108.01045.

[20] R. Abbott, T. D. Abbott, S. Abraham, F. Acernese, K. Ackley, A. Adams, C. Adams, R. X. Adhikari, V. B. Adya, C. Affeldt, and et al., "Population

properties of compact objects from the second ligo–virgo gravitational-wave transient catalog," *The Astrophysical Journal Letters*, vol. 913, no. 1, p. L7, May 2021. [Online]. Available: http://dx.doi.org/10.3847/2041-8213/abe949

[21] B. P. Abbott, R. Abbott, T. D. Abbott, S. Abraham, F. Acernese, K. Ackley, C. Adams, R. X. Adhikari, V. B. Adya, C. Affeldt, and et al., "A gravitational-wave measurement of the hubble constant following the second observing run of advanced ligo and virgo," *The Astrophysical Journal*, vol. 909, no. 2, p. 218, Mar 2021. [Online]. Available: http://dx.doi.org/10.3847/1538-4357/abdcb7

[22] B. Abbott, R. Abbott, T. Abbott, S. Abraham, F. Acernese, K. Ackley, C. Adams, V. Adya, C. Affeldt, M. Agathos, and et al., "Search for the isotropic stochastic background using data from advanced ligo's second observing run," *Physical Review D*, vol. 100, no. 6, Sep 2019. [Online]. Available: http://dx.doi.org/10.1103/PhysRevD.100.061101

[23] A. Ghosh, R. Brito, and A. Buonanno, "Constraints on quasinormal-mode frequencies with ligo-virgo binary–black-hole observations," *Physical Review D*, vol. 103, no. 12, Jun 2021. [Online]. Available: http://dx.doi.org/10.1103/PhysRevD.103.124041

[24] B. Abbott, R. Abbott, T. Abbott, F. Acernese, K. Ackley, C. Adams, T. Adams, P. Addesso, R. Adhikari, V. Adya, and et al., "Gw170817: Measurements of neutron star radii and equation of state," *Physical*

Review Letters, vol. 121, no. 16, Oct 2018. [Online]. Available: http://dx.doi.org/10.1103/PhysRevLett.121.161101

[25] F. Hernandez Vivanco, R. Smith, E. Thrane, P. D. Lasky, C. Talbot, and V. Raymond, "Measuring the neutron star equation of state with gravitational waves: The first forty binary neutron star merger observations," *Physical Review D*, vol. 100, no. 10, Nov 2019. [Online]. Available: http://dx.doi.org/10.1103/PhysRevD.100.103009

[26] B. Abbott, R. Abbott, T. Abbott, F. Acernese, K. Ackley, C. Adams, T. Adams, P. Addesso, R. Adhikari, V. Adya, and et al., "Constraining the p -mode– g -mode tidal instability with gw170817," *Physical Review Letters*, vol. 122, no. 6, Feb 2019. [Online]. Available: http://dx.doi.org/10.1103/PhysRevLett.122.061104

[27] Z. Pan, Z. Lyu, B. Bonga, N. Ortiz, and H. Yang, "Probing crust meltdown in inspiraling binary neutron stars," *Physical Review Letters*, vol. 125, no. 20, Nov 2020. [Online]. Available: http://dx.doi.org/10.1103/PhysRevLett.125.201102

[28] S. Y. Lau and K. Yagi, "Probing hybrid stars with gravitational waves via interfacial modes," *Physical Review D*, vol. 103, no. 6, Mar 2021. [Online]. Available: http://dx.doi.org/10.1103/PhysRevD.103.063015

[29] T. Akutsu, M. Ando, K. Arai, Y. Arai, S. Araki, A. Araya, N. Aritomi, H. Asada, Y. Aso, S. Atsuta, K. Awai, S. Bae, L. Baiotti, M. A. Barton,

K. Cannon, E. Capocasa, C.-S. Chen, T.-W. Chiu, K. Cho, Y.-K. Chu, K. Craig, W. Creus, K. Doi, K. Eda, Y. Enomoto, R. Flaminio, Y. Fujii, M. K. Fujimoto, M. Fukunaga, M. Fukushima, T. Furuhata, S. Haino, K. Hasegawa, K. Hashino, K. Hayama, S. Hirobayashi, E. Hirose, B. H. Hsieh, C.-Z. Huang, B. Ikenoue, Y. Inoue, K. Ioka, Y. Itoh, K. Izumi, T. Kaji, T. Kajita, M. Kakizaki, M. Kamiizumi, S. Kanbara, N. Kanda, S. Kanemura, M. Kaneyama, G. Kang, J. Kasuya, Y. Kataoka, N. Kawai, S. Kawamura, T. Kawasaki, C. Kim, J. Kim, J. C. Kim, W. S. Kim, Y. M. Kim, N. Kimura, T. Kinugawa, S. Kirii, Y. Kitaoka, H. Kitazawa, Y. Kojima, K. Kokeyama, K. Komori, A. K. H. Kong, K. Kotake, R. Kozu, R. Kumar, H.-S. Kuo, S. Kuroyanagi, H. K. Lee, H. M. Lee, H. W. Lee, M. Leonardi, C.-Y. Lin, F.-L. Lin, G. C. Liu, Y. Liu, E. Majorana, S. Mano, M. Marchio, T. Matsui, F. Matsushima, Y. Michimura, N. Mio, O. Miyakawa, A. Miyamoto, T. Miyamoto, K. Miyo, S. Miyoki, W. Morii, S. Morisaki, Y. Moriwaki, T. Morozumi, M. Musha, K. Nagano, S. Nagano, K. Nakamura, T. Nakamura, H. Nakano, M. Nakano, K. Nakao, T. Narikawa, L. Naticchioni, L. N. Quynh, W. T. Ni, A. Nishizawa, Y. Obuchi, T. Ochi, J. J. Oh, S. H. Oh, M. Ohashi, N. Ohishi, M. Ohkawa, K. Okutomi, K. Ono, K. Oohara, C. P. Ooi, S.-S. Pan, J. Park, F. E. P. Arellano, I. Pinto, N. Sago, M. Saijo, S. Saitou, Y. Saito, K. Sakai, Y. Sakai, Y. Sakai, M. Sasai, M. Sasaki, Y. Sasaki, S. Sato, N. Sato, T. Sato, Y. Sekiguchi, N. Seto, M. Shibata,

T. Shimoda, H. Shinkai, T. Shishido, A. Shoda, K. Somiya, E. J. Son, A. Suemasa, T. Suzuki, T. Suzuki, H. Tagoshi, H. Tahara, H. Takahashi, R. Takahashi, A. Takamori, H. Takeda, H. Tanaka, K. Tanaka, T. Tanaka, S. Tanioka, E. N. T. S. Martin, D. Tatsumi, T. Tomaru, T. Tomura, F. Travasso, K. Tsubono, S. Tsuchida, N. Uchikata, T. Uchiyama, T. Uehara, S. Ueki, K. Ueno, F. Uraguchi, T. Ushiba, M. H. P. M. van Putten, H. Vocca, S. Wada, T. Wakamatsu, Y. Watanabe, W.-R. Xu, T. Yamada, A. Yamamoto, K. Yamamoto, K. Yamamoto, S. Yamamoto, T. Yamamoto, K. Yokogawa, J. Yokoyama, T. Yokozawa, T. H. Yoon, T. Yoshioka, H. Yuzurihara, S. Zeidler, Z. H. Zhu, and K. collaboration, "Kagra: 2.5 generation interferometric gravitational wave detector," *Nature Astronomy*, vol. 3, no. 1, pp. 35–40, 2019. [Online]. Available: https://doi.org/10.1038/s41550-018-0658-y

[30] D. Reitze, R. X. Adhikari, S. Ballmer, B. Barish, L. Barsotti, G. Billingsley, D. A. Brown, Y. Chen, D. Coyne, R. Eisenstein, M. Evans, P. Fritschel, E. D. Hall, A. Lazzarini, G. Lovelace, J. Read, B. S. Sathyaprakash, D. Shoemaker, J. Smith, C. Torrie, S. Vitale, R. Weiss, C. Wipf, and M. Zucker, "Cosmic explorer: The u.s. contribution to gravitational-wave astronomy beyond ligo," *arxiv*, 2019. [Online]. Available: https://arxiv.org/abs/1907.04833

[31] M. Maggiore, C. V. D. Broeck, N. Bartolo, E. Belgacem, D. Bertacca, M. A. Bizouard, M. Branchesi, S. Clesse, S. Foffa, J. Garcí a-Bellido, S. Grimm, J. Harms, T. Hinderer, S. Matarrese, C. Palomba,

M. Peloso, A. Ricciardone, and M. Sakellariadou, "Science case for the einstein telescope," *Journal of Cosmology and Astroparticle Physics*, vol. 2020, no. 03, pp. 050–050, mar 2020. [Online]. Available: https://doi.org/10.1088%2F1475-7516%2F2020%2F03%2F050

[32] T. Robson, N. J. Cornish, and C. Liu, "The construction and use of lisa sensitivity curves," *Classical and Quantum Gravity*, vol. 36, no. 10, p. 105011, apr 2019. [Online]. Available: https://dx.doi.org/10.1088/1361-6382/ab1101

[33] J. Luo, L.-S. Chen, H.-Z. Duan, Y.-G. Gong, S. Hu, J. Ji, Q. Liu, J. Mei, V. Milyukov, M. Sazhin, C.-G. Shao, V. T. Toth, H.-B. Tu, Y. Wang, Y. Wang, H.-C. Yeh, M.-S. Zhan, Y. Zhang, V. Zharov, and Z.-B. Zhou, "Tianqin: a space-borne gravitational wave detector," *Classical and Quantum Gravity*, vol. 33, no. 3, p. 035010, jan 2016. [Online]. Available: https://dx.doi.org/10.1088/0264-9381/33/3/035010

[34] C. Shi, J. Bao, H.-T. Wang, J. dong Zhang, Y.-M. Hu, A. Sesana, E. Barausse, J. Mei, and J. Luo, "Science with the TianQin observatory: Preliminary results on testing the no-hair theorem with ringdown signals," *Physical Review D*, vol. 100, no. 4, aug 2019. [Online]. Available: https://doi.org/10.1103%2Fphysrevd.100.044036

[35] K. Yagi and N. Seto, "Detector configuration of decigo/bbo and identification of cosmological neutron-star binaries," *Physical Review D*, vol. 83, no. 4, Feb

2011. [Online]. Available: http://dx.doi.org/10.1103/PhysRevD.83.044011

[36] S. Isoyama, H. Nakano, and T. Nakamura, "Multiband gravitational-wave astronomy: Observing binary inspirals with a decihertz detector, B-DECIGO," *Progress of Theoretical and Experimental Physics*, vol. 2018, no. 7, 07 2018, https://academic.oup.com/ptep/article-pdf/2018/7/073E01/25332865/pty078.pdf, 073E01. [Online]. Available: https://doi.org/10.1093/ptep/pty078

[37] N. Jiang and K. Yagi, "Improved Analytic Modeling of Neutron Star Interiors," *Phys. Rev. D*, vol. 99, no. 12, p. 124029, 2019, 1904.05954.

[38] N. Jiang and K. Yagi, "Analytic I-Love-C relations for realistic neutron stars," *Phys. Rev. D*, vol. 101, no. 12, p. 124006, 2020, 2003.10498.

[39] N. Jiang and K. Yagi, "Probing modified gravitational-wave propagation through tidal measurements of binary neutron star mergers," *Phys. Rev. D*, vol. 103, no. 12, p. 124047, 2021, 2104.04442.

[40] Z. Lyu, N. Jiang, and K. Yagi, "Constraints on Einstein-dilation-Gauss-Bonnet gravity from black hole-neutron star gravitational wave events," *Phys. Rev. D*, vol. 105, no. 6, p. 064001, 2022, 2201.02543, [Erratum: Phys.Rev.D 106, 069901 (2022), Erratum: Phys.Rev.D 106, 069901 (2022)].

[41] J. Lattimer and M. Prakash, "Neutron star structure and the equation of state," *Astrophys.J.*, vol. 550, p. 426, 2001, astro-ph/0002232.

[42] J. M. Lattimer and M. Prakash, "Neutron star structure and the equation of state," *The Astrophysical Journal*, vol. 550, no. 1, p. 426, 2001. [Online]. Available: http://stacks.iop.org/0004-637X/550/i=1/a=426

[43] J. M. Lattimer and M. Prakash, "Neutron Star Observations: Prognosis for Equation of State Constraints," *Phys.Rept.*, vol. 442, pp. 109–165, 2007, astro-ph/0612440.

[44] F. Özel and P. Freire, "Masses, Radii, and the Equation of State of Neutron Stars," *Ann. Rev. Astron. Astrophys.*, vol. 54, pp. 401–440, 2016, 1603.02698.

[45] F. Ozel, G. Baym, and T. Guver, "Astrophysical Measurement of the Equation of State of Neutron Star Matter," *Phys.Rev.*, vol. D82, p. 101301, 2010, 1002.3153.

[46] A. W. Steiner, J. M. Lattimer, and E. F. Brown, "The Equation of State from Observed Masses and Radii of Neutron Stars," *Astrophys.J.*, vol. 722, pp. 33–54, 2010, 1005.0811.

[47] F. Ozel, D. Psaltis, T. Guver, G. Baym, C. Heinke, and S. Guillot, "The Dense Matter Equation of State from Neutron Star Radius and Mass Measurements," *Astrophys. J.*, vol. 820, no. 1, p. 28, 2016, 1505.05155.

[48] T. E. Riley, A. L. Watts, S. Bogdanov, P. S. Ray, R. M. Ludlam, S. Guillot, Z. Arzoumanian, C. L. Baker, A. V. Bilous, D. Chakrabarty, K. C. Gendreau,

A. K. Harding, W. C. G. Ho, J. M. Lattimer, S. M. Morsink, and T. E. Strohmayer, “A nicer view of psr j0030+0451: Millisecond pulsar parameter estimation,” *The Astrophysical Journal*, vol. 887, no. 1, p. L21, dec 2019. [Online]. Available: https://doi.org/10.3847%2F2041-8213%2Fab481c

[49] M. C. Miller, F. K. Lamb, A. J. Dittmann, S. Bogdanov, Z. Arzoumanian, K. C. Gendreau, S. Guillot, A. K. Harding, W. C. G. Ho, J. M. Lattimer, R. M. Ludlam, S. Mahmoodifar, S. M. Morsink, P. S. Ray, T. E. Strohmayer, K. S. Wood, T. Enoto, R. Foster, T. Okajima, G. Prigozhin, and Y. Soong, “Psr j0030+0451 mass and radius from nicer data and implications for the properties of neutron star matter,” *The Astrophysical Journal*, vol. 887, no. 1, p. L24, dec 2019. [Online]. Available: https://doi.org/10.3847%2F2041-8213%2Fab50c5

[50] S. Bogdanov, S. Guillot, P. S. Ray, M. T. Wolff, D. Chakrabarty, W. C. G. Ho, M. Kerr, F. K. Lamb, A. Lommen, R. M. Ludlam, R. Milburn, S. Montano, M. C. Miller, M. Bauböck, F. Özel, D. Psaltis, R. A. Remillard, T. E. Riley, J. F. Steiner, T. E. Strohmayer, A. L. Watts, K. S. Wood, J. Zeldes, T. Enoto, T. Okajima, J. W. Kellogg, C. Baker, C. B. Markwardt, Z. Arzoumanian, and K. C. Gendreau, “Constraining the neutron star mass–radius relation and dense matter equation of state with nicer. i. the millisecond pulsar x-ray data set,” *The Astrophysical Journal*, vol. 887, no. 1, p. L25, dec 2019. [Online]. Available: https://doi.org/10.3847%2F2041-8213%2Fab53eb

[51] S. Bogdanov, F. K. Lamb, S. Mahmoodifar, M. C. Miller, S. M. Morsink, T. E. Riley, T. E. Strohmayer, A. K. Tung, A. L. Watts, A. J. Dittmann, D. Chakrabarty, S. Guillot, Z. Arzoumanian, and K. C. Gendreau, “Constraining the neutron star mass–radius relation and dense matter equation of state with NICER. II. emission from hot spots on a rapidly rotating neutron star,” *The Astrophysical Journal*, vol. 887, no. 1, p. L26, dec 2019. [Online]. Available: https://doi.org/10.3847%2F2041-8213%2Fab5968

[52] S. Guillot, M. Kerr, P. S. Ray, S. Bogdanov, S. Ransom, J. S. Deneva, Z. Arzoumanian, P. Bult, D. Chakrabarty, K. C. Gendreau, W. C. G. Ho, G. K. Jaisawal, C. Malacaria, M. C. Miller, T. E. Strohmayer, M. T. Wolff, K. S. Wood, N. A. Webb, L. Guillemot, I. Cognard, and G. Theureau, “Nicer x-ray observations of seven nearby rotation-powered millisecond pulsars,” *The Astrophysical Journal*, vol. 887, no. 1, p. L27, dec 2019. [Online]. Available: https://doi.org/10.3847%2F2041-8213%2Fab511b

[53] G. Raaijmakers, T. E. Riley, A. L. Watts, S. K. Greif, S. M. Morsink, K. Hebeler, A. Schwenk, T. Hinderer, S. Nissanke, S. Guillot, Z. Arzoumanian, S. Bogdanov, D. Chakrabarty, K. C. Gendreau, W. C. G. Ho, J. M. Lattimer, R. M. Ludlam, and M. T. Wolff, “A nicer view of psr j0030+0451: Implications for the dense matter equation of state,” *The Astrophysical Journal*, vol. 887, no. 1, p. L22, dec 2019. [Online]. Available: https://doi.org/10.3847%2F2041-8213%2Fab451a

[54] J.-E. Christian and J. Schaffner-Bielich, "Twin stars and the stiffness of the nuclear equation of state: ruling out strong phase transitions below $1.7n_0$ with the new NICER radius measurements," *The Astrophysical Journal*, 2019, 1912.09809.

[55] J.-L. Jiang, S.-P. Tang, Y.-Z. Wang, Y.-Z. Fan, and D.-M. Wei, "PSR J0030+0451, GW170817 and the nuclear data: joint constraints on equation of state and bulk properties of neutron stars," *The Astrophysical Journal*, 2019, 1912.07467.

[56] G. Raaijmakers *et al.*, "Constraining the dense matter equation of state with joint analysis of NICER and LIGO/Virgo measurements," *The Astrophysical Journal*, 2019, 1912.11031.

[57] J. Zimmerman, Z. Carson, K. Schumacher, A. W. Steiner, and K. Yagi, "Measuring Nuclear Matter Parameters with NICER and LIGO/Virgo," *arXiv*, 2020, 2002.03210.

[58] T. Dietrich, M. W. Coughlin, P. T. H. Pang, M. Bulla, J. Heinzel, L. Issa, I. Tews, and S. Antier, "New Constraints on the Supranuclear Equation of State and the Hubble Constant from Nuclear Physics – Multi-Messenger Astronomy," *Science*, 2020, 2002.11355.

[59] P. B. Demorest, T. Pennucci, S. M. Ransom, M. S. E. Roberts, and J. W. T. Hessels, "A two-solar-mass neutron star measured using Shapiro delay," *Nature*,

vol. 467, pp. 1081–1083, Oct. 2010, 1010.5788.

[60] J. Antoniadis, P. C. Freire, N. Wex, T. M. Tauris, R. S. Lynch *et al.*, "A Massive Pulsar in a Compact Relativistic Binary," *Science*, vol. 340, p. 6131, 2013, 1304.6875.

[61] H. T. Cromartie, E. Fonseca, S. M. Ransom, P. B. Demorest, Z. Arzoumanian, H. Blumer, P. R. Brook, M. E. DeCesar, T. Dolch, J. A. Ellis, R. D. Ferdman, E. C. Ferrara, N. Garver-Daniels, P. A. Gentile, M. L. Jones, M. T. Lam, D. R. Lorimer, R. S. Lynch, M. A. McLaughlin, C. Ng, D. J. Nice, T. T. Pennucci, R. Spiewak, I. H. Stairs, K. Stovall, J. K. Swiggum, and W. W. Zhu, "Relativistic shapiro delay measurements of an extremely massive millisecond pulsar," *Nature Astronomy*, vol. 4, no. 1, pp. 72–76, 2020. [Online]. Available: https://doi.org/10.1038/s41550-019-0880-2

[62] B. P. Abbott *et al.*, "Properties of the binary neutron star merger GW170817," *Phys. Rev.*, vol. X9, no. 1, p. 011001, 2019, 1805.11579.

[63] B. P. Abbott *et al.*, "GW170817: Measurements of neutron star radii and equation of state," *Phys. Rev. Lett.*, vol. 121, no. 16, p. 161101, 2018, 1805.11581.

[64] T. Malik, N. Alam, M. Fortin, C. Providência, B. K. Agrawal, T. K. Jha, B. Kumar, and S. K. Patra, "GW170817: constraining the nuclear matter equation of state from the neutron star tidal deformability," *Phys. Rev.*, vol. C98, no. 3, p. 035804, 2018, 1805.11963.

[65] Z. Carson, A. W. Steiner, and K. Yagi, "Constraining nuclear matter parameters with GW170817," *Phys. Rev.*, vol. D99, no. 4, p. 043010, 2019, 1812.08910.

[66] M. Kramer, I. H. Stairs, R. N. Manchester, M. A. McLaughlin, A. G. Lyne, R. D. Ferdman, M. Burgay, D. R. Lorimer, A. Possenti, N. D'Amico, J. M. Sarkissian, G. B. Hobbs, J. E. Reynolds, P. C. C. Freire, and F. Camilo, "Tests of general relativity from timing the double pulsar," *Science*, vol. 314, no. 5796, pp. 97–102, 2006, http://science.sciencemag.org/content/314/5796/97.full.pdf. [Online]. Available: http://science.sciencemag.org/content/314/5796/97

[67] I. H. Stairs, "Testing general relativity with pulsar timing," *Living Rev.Rel.*, vol. 6, p. 5, 2003, astro-ph/0307536.

[68] B. P. Abbott *et al.*, "Tests of General Relativity with GW170817," *Physical Review Letters*, 2018, 1811.00364.

[69] B. F. Schutz, *A FIRST COURSE IN GENERAL RELATIVITY.* Cambridge, UK: Cambridge Univ. Pr., 1985.

[70] H. A. Buchdahl, "General-Relativistic Fluid Spheres. III. a Static Gaseous Model," *Astrophys. J.* , vol. 147, p. 310, Jan. 1967.

[71] R. C. Tolman, "Static solutions of einstein's field equations for spheres of fluid," *Phys. Rev.*, vol. 55, pp. 364–373, Feb 1939. [Online]. Available: https://link.aps.org/doi/10.1103/PhysRev.55.364

[72] A. M. Raghoonundun and D. W. Hobill, "Possible Physical Realizations of the Tolman VII solution," *Phys. Rev.*, vol. D92, no. 12, p. 124005, 2015, 1506.05813.

[73] M. D. P.S. Negi, "Relativistic supermassive stars," *Astrophysics and Space Science*, vol. 275, pp. 185–207, Feb 2001. [Online]. Available: https://link.springer.com/article/10.1023/A:1002707730439#citeas

[74] N. Neary, M. Ishak, and K. Lake, "The Tolman VII solution, trapped null orbits and W modes," *Phys. Rev.*, vol. D64, p. 084001, 2001, gr-qc/0104002.

[75] A. M. Raghoonundun and D. W. Hobill, "The Geometrical Structure of the Tolman VII solution," *arXiv*, 2016, 1601.06337.

[76] L. K. Tsui and P. T. Leung, "Probing the interior of neutron stars with gravitational waves," *Phys. Rev. Lett.*, vol. 95, p. 151101, Oct 2005. [Online]. Available: https://link.aps.org/doi/10.1103/PhysRevLett.95.151101

[77] L. K. Tsui and P. T. Leung, "Perturbative analysis of universality and individuality in gravitational waves from neutron stars," *The Astrophysical Journal*, vol. 631, no. 1, p. 495, 2005. [Online]. Available: http://stacks.iop.org/0004-637X/631/i=1/a=495

[78] L. K. Tsui, P. T. Leung, and J. Wu, "Determination of the internal structure of neutron stars from gravitational wave spectra," *Phys. Rev.*, vol. D74, p. 124025, 2006, gr-qc/0610099.

[79] R. L. Bowers and E. P. T. Liang, "Anisotropic Spheres in General Relativity," *Astrophys. J.*, vol. 188, pp. 657–665, 1974.

[80] K. Yagi and N. Yunes, "I-Love-Q Relations: From Compact Stars to Black Holes," *Class. Quant. Grav.*, vol. 33, no. 9, p. 095005, 2016, 1601.02171.

[81] K. Yagi, L. C. Stein, and N. Yunes, "Challenging the Presence of Scalar Charge and Dipolar Radiation in Binary Pulsars," *Phys. Rev.*, vol. D93, no. 2, p. 024010, 2016, 1510.02152.

[82] M. Kramer and N. Wex, "The double pulsar system: a unique laboratory for gravity," *Classical and Quantum Gravity*, vol. 26, no. 7, p. 073001, feb 2009. [Online]. Available: https://doi.org/10.1088%2F0264-9381%2F26%2F7%2F073001

[83] J. M. Lattimer and B. F. Schutz, "Constraining the equation of state with moment of inertia measurements," *The Astrophysical Journal*, vol. 629, no. 2, pp. 979–984, aug 2005. [Online]. Available: https://doi.org/10.1086%2F431543

[84] T. Hinderer, "Tidal love numbers of neutron stars," *The Astrophysical Journal*, vol. 677, no. 2, pp. 1216–1220, apr 2008. [Online]. Available: https://doi.org/10.1086%2F533487

[85] E. E. Flanagan and T. Hinderer, "Constraining neutron-star tidal love numbers with gravitational-wave detectors," *Phys. Rev. D*, vol. 77, p. 021502, Jan 2008. [Online]. Available: https://link.aps.org/doi/10.1103/PhysRevD.77.021502

[86] B. Abbott, R. Abbott, T. Abbott, F. Acernese, K. Ackley, C. Adams, T. Adams, P. Addesso, R. Adhikari, V. Adya, and et al., "Gw170817: Measurements of neutron star radii and equation of state," *Physical Review Letters*, vol. 121, no. 16, Oct 2018. [Online]. Available: http://dx.doi.org/10.1103/PhysRevLett.121.161101

[87] B. P. Abbott *et al.*, "GW170817: Measurements of neutron star radii and equation of state," *Phys. Rev. Lett.*, vol. 121, no. 16, p. 161101, 2018, 1805.11581.

[88] E. Annala, T. Gorda, A. Kurkela, and A. Vuorinen, "Gravitational-wave constraints on the neutron-star-matter Equation of State," *Phys. Rev. Lett.*, vol. 120, no. 17, p. 172703, 2018, 1711.02644.

[89] C. Raithel, F. Ozel, and D. Psaltis, "Tidal deformability from GW170817 as a direct probe of the neutron star radius," *Astrophys. J.*, vol. 857, no. 2, p. L23, 2018, 1803.07687.

[90] Y. Lim and J. W. Holt, "Neutron star tidal deformabilities constrained by nuclear theory and experiment," *Phys. Rev. Lett.*, vol. 121, no. 6, p. 062701, 2018, 1803.02803.

[91] A. Bauswein, O. Just, H.-T. Janka, and N. Stergioulas, "Neutron-star radius constraints from GW170817 and future detections," *Astrophys. J.*, vol. 850, no. 2, p. L34, 2017, 1710.06843.

[92] S. De, D. Finstad, J. M. Lattimer, D. A. Brown, E. Berger, and C. M. Biwer, "Tidal Deformabilities and Radii of Neutron Stars from the Observation of GW170817," *Phys. Rev. Lett.*, vol. 121, no. 9, p. 091102, 2018, 1804.08583, [Erratum: Phys. Rev. Lett.121,no.25,259902(2018)].

[93] E. R. Most, L. R. Weih, L. Rezzolla, and J. Schaffner-Bielich, "New constraints on radii and tidal deformabilities of neutron stars from GW170817," *Phys. Rev. Lett.*, vol. 120, no. 26, p. 261103, 2018, 1803.00549.

[94] E. Annala, T. Gorda, A. Kurkela, J. Nättilä, and A. Vuorinen, "Quark-matter cores in neutron stars," *Nature Physics*, 2019, 1903.09121.

[95] T. Malik, N. Alam, M. Fortin, C. Providência, B. K. Agrawal, T. K. Jha, B. Kumar, and S. K. Patra, "GW170817: constraining the nuclear matter equation of state from the neutron star tidal deformability," *Phys. Rev.*, vol. C98, no. 3, p. 035804, 2018, 1805.11963.

[96] Z. Carson, A. W. Steiner, and K. Yagi, "Constraining nuclear matter parameters with gw170817," *Phys. Rev. D*, vol. 99, p. 043010, Feb 2019. [Online]. Available: https://link.aps.org/doi/10.1103/PhysRevD.99.043010

[97] Z. Carson, A. W. Steiner, and K. Yagi, "Future Prospects for Constraining Nuclear Matter Parameters with Gravitational Waves," *Phys. Rev.*, vol. D100, no. 2, p. 023012, 2019, 1906.05978.

[98] C. A. Raithel and F. Ozel, “Measurement of the nuclear symmetry energy parameters from gravitational wave events,” *The Astrophysical Journal*, 2019, 1908.00018.

[99] K. Yagi and N. Yunes, “Approximate universal relations for neutron stars and quark stars,” *Physics Reports*, vol. 681, pp. 1 – 72, 2017. [Online]. Available: http://www.sciencedirect.com/science/article/pii/S0370157317300492

[100] D. D. Doneva and G. Pappas, “Universal Relations and Alternative Gravity Theories,” *Astrophys. Space Sci. Libr.*, vol. 457, pp. 737–806, 2018, 1709.08046.

[101] K. Yagi and N. Yunes, “I-love-q: Unexpected universal relations for neutron stars and quark stars,” *Science*, vol. 341, no. 6144, pp. 365–368, 2013. [Online]. Available: https://science.sciencemag.org/content/341/6144/365

[102] K. Yagi and N. Yunes, “I-Love-Q Relations in Neutron Stars and their Applications to Astrophysics, Gravitational Waves and Fundamental Physics,” *Phys. Rev.*, vol. D88, no. 2, p. 023009, 2013, 1303.1528.

[103] K. Yagi and N. Yunes, “Binary love relations,” *Classical and Quantum Gravity*, vol. 33, no. 13, p. 13LT01, Jun 2016. [Online]. Available: http://dx.doi.org/10.1088/0264-9381/33/13/13LT01

[104] K. Yagi and N. Yunes, “Approximate Universal Relations among Tidal Parameters for Neutron Star Binaries,” *Class. Quant. Grav.*, vol. 34, no. 1, p. 015006, 2017, 1608.06187.

[105] D. Chatterjee, A. H. K. R., G. Holder, D. E. Holz, S. Perkins, K. Yagi, and N. Yunes, "Cosmology with love: Measuring the hubble constant using neutron star universal relations," *Physical Review D*, vol. 104, no. 8, oct 2021. [Online]. Available: https://doi.org/10.1103%2Fphysrevd.104.083528

[106] Y. Xie, D. Chatterjee, G. Holder, D. E. Holz, S. Perkins, K. Yagi, and N. Yunes, "Breaking bad degeneracies with love relations: Improving gravitational-wave measurements through universal relations," *Physical Review D*, vol. 107, no. 4, feb 2023. [Online]. Available: https://doi.org/10.1103%2Fphysrevd.107.043010

[107] K. Yagi, L. C. Stein, G. Pappas, N. Yunes, and T. A. Apostolatos, "Why I-Love-Q: Explaining why universality emerges in compact objects," *Phys. Rev.*, vol. D90, no. 6, p. 063010, 2014, 1406.7587.

[108] Y.-H. Sham, T. K. Chan, L.-M. Lin, and P. T. Leung, "UNVEILING THE UNIVERSALITY OF i-LOVE-q RELATIONS," *The Astrophysical Journal*, vol. 798, no. 2, p. 121, jan 2015. [Online]. Available: https://doi.org/10.1088%2F0004-637x%2F798%2F2%2F121

[109] B. A. et al., "A gravitational-wave standard siren measurement of the hubble constant," *Nature*, vol. 551, no. 7678, p. 85–88, Oct 2017. [Online]. Available: http://dx.doi.org/10.1038/nature24471

[110] M. Fishbach *et al.*, "A standard siren measurement of the hubble constant from GW170817 without the electromagnetic counterpart," *The*

Astrophysical Journal, vol. 871, no. 1, p. L13, jan 2019. [Online]. Available: https://doi.org/10.3847/2041-8213/aaf96e

[111] H.-Y. Chen, M. Fishbach, and D. E. Holz, "A two per cent hubble constant measurement from standard sirens within five years," *Nature*, vol. 562, no. 7728, p. 545–547, Oct 2018. [Online]. Available: http://dx.doi.org/10.1038/s41586-018-0606-0

[112] E. Belgacem, Y. Dirian, S. Foffa, and M. Maggiore, "Modified gravitational-wave propagation and standard sirens," *Phys. Rev. D*, vol. 98, p. 023510, Jul 2018. [Online]. Available: https://link.aps.org/doi/10.1103/PhysRevD.98.023510

[113] E. Belgacem, Y. Dirian, S. Foffa, E. J. Howell, M. Maggiore, and T. Regimbau, "Cosmology and dark energy from joint gravitational wave-grb observations," *Journal of Cosmology and Astroparticle Physics*, vol. 2019, no. 08, p. 015–015, Aug 2019. [Online]. Available: http://dx.doi.org/10.1088/1475-7516/2019/08/015

[114] M. Lagos, M. Fishbach, P. Landry, and D. E. Holz, "Standard sirens with a running planck mass," *Physical Review D*, vol. 99, no. 8, Apr 2019. [Online]. Available: http://dx.doi.org/10.1103/PhysRevD.99.083504

[115] R. D'Agostino and R. C. Nunes, "Probing observational bounds on scalar-tensor theories from standard sirens," *Physical Review D*, vol. 100, no. 4, Aug 2019. [Online]. Available: http://dx.doi.org/10.1103/PhysRevD.100.044041

[116] A. Finke, S. Foffa, F. Iacovelli, M. Maggiore, and M. Mancarella, "Cosmology with ligo/virgo dark sirens: Hubble parameter and modified gravitational wave propagation," 2021," 2101.12660.

[117] S. Mukherjee, B. D. Wandelt, and J. Silk, "Testing the general theory of relativity using gravitational wave propagation from dark standard sirens," *Monthly Notices of the Royal Astronomical Society*, vol. 502, no. 1, pp. 1136–1144, 01 2021, https://academic.oup.com/mnras/article-pdf/502/1/1136/36171532/stab001.pdf. [Online]. Available: https://doi.org/10.1093/mnras/stab001

[118] B. P. Abbott, R. Abbott, T. D. Abbott, S. Abraham, F. Acernese, K. Ackley, C. Adams, R. X. Adhikari, V. B. Adya, C. Affeldt, and et al., "Gw190425: Observation of a compact binary coalescence with total mass $\sim 3.4\ m_{\odot}$," *The Astrophysical Journal*, vol. 892, no. 1, p. L3, Mar 2020. [Online]. Available: http://dx.doi.org/10.3847/2041-8213/ab75f5

[119] B. P. Abbott *et al.*, "Tests of general relativity with GW150914," *Phys. Rev. Lett.*, vol. 116, no. 22, p. 221101, 2016, 1602.03841, [Erratum: Phys.Rev.Lett. 121, 129902 (2018)].

[120] N. Yunes, K. Yagi, and F. Pretorius, "Theoretical Physics Implications of the Binary Black-Hole Mergers GW150914 and GW151226," *Phys. Rev.*, vol. D94, no. 8, p. 084002, 2016, 1603.08955.

[121] B. Abbott, R. Abbott, T. Abbott, S. Abraham, F. Acernese, K. Ackley, C. Adams, R. Adhikari, V. Adya, C. Affeldt, and et al., "Tests of general relativity with the binary black hole signals from the ligo-virgo catalog gwtc-1," *Physical Review D*, vol. 100, no. 10, Nov 2019. [Online]. Available: http://dx.doi.org/10.1103/PhysRevD.100.104036

[122] R. Abbott *et al.*, "Tests of general relativity with binary black holes from the second LIGO-Virgo gravitational-wave transient catalog," *Phys. Rev. D*, vol. 103, no. 12, p. 122002, 2021, 2010.14529.

[123] J. Zhao, L. Shao, Z. Cao, and B.-Q. Ma, "Reduced-order surrogate models for scalar-tensor gravity in the strong field regime and applications to binary pulsars and GW170817," *Phys. Rev. D*, vol. 100, no. 6, p. 064034, 2019, 1907.00780.

[124] R. Niu, X. Zhang, B. Wang, and W. Zhao, "Constraining scalar-tensor theories by neutron star-black hole gravitational wave events," 2021," 2105.13644.

[125] J. Zhang, Z. Lyu, J. Huang, M. C. Johnson, L. Sagunski, M. Sakellariadou, and H. Yang, "First constraints on nuclear coupling of axionlike particles from the binary neutron star gravitational wave event gw170817," 2021," 2105.13963.

[126] R. Nair, S. Perkins, H. O. Silva, and N. Yunes, "Fundamental Physics Implications for Higher-Curvature Theories from Binary Black Hole Signals in the LIGO-Virgo Catalog GWTC-1," *Phys. Rev. Lett.*, vol. 123, no. 19, p. 191101, 2019, 1905.00870.

[127] S. E. Perkins, R. Nair, H. O. Silva, and N. Yunes, "Improved gravitational-wave constraints on higher-order curvature theories of gravity," *Physical Review D*, vol. 104, no. 2, Jul 2021. [Online]. Available: http://dx.doi.org/10.1103/PhysRevD.104.024060

[128] M. Okounkova, L. C. Stein, J. Moxon, M. A. Scheel, and S. A. Teukolsky, "Numerical relativity simulation of GW150914 beyond general relativity," *Phys. Rev. D*, vol. 101, no. 10, p. 104016, 2020, 1911.02588.

[129] M. Okounkova, W. M. Farr, M. Isi, and L. C. Stein, "Constraining gravitational wave amplitude birefringence and chern-simons gravity with gwtc-2," 2021," 2101.11153.

[130] S. Nojiri, S. D. Odintsov, and M. Sasaki, "Gauss-Bonnet dark energy," *Phys. Rev. D*, vol. 71, p. 123509, 2005, hep-th/0504052.

[131] K. Yagi, "A New constraint on scalar Gauss-Bonnet gravity and a possible explanation for the excess of the orbital decay rate in a low-mass X-ray binary," *Phys. Rev.*, vol. D86, p. 081504, 2012, 1204.4524.

[132] G. Antoniou, A. Bakopoulos, and P. Kanti, "Black-Hole Solutions with Scalar Hair in Einstein-Scalar-Gauss-Bonnet Theories," *Phys. Rev. D*, vol. 97, no. 8, p. 084037, 2018, 1711.07431.

[133] G. Antoniou, A. Bakopoulos, and P. Kanti, "Evasion of no-hair theorems and novel black-hole solutions in gauss-bonnet theories," *Physical Review Letters*,

vol. 120, no. 13, Mar 2018. [Online]. Available: http://dx.doi.org/10.1103/PhysRevLett.120.131102

[134] K. Yagi, L. C. Stein, N. Yunes, and T. Tanaka, "Post-Newtonian, Quasi-Circular Binary Inspirals in Quadratic Modified Gravity," *Phys. Rev. D*, vol. 85, p. 064022, 2012, 1110.5950, [Erratum: Phys.Rev.D 93, 029902 (2016)].

[135] E. Barausse and K. Yagi, "Gravitation-Wave Emission in Shift-Symmetric Horndeski Theories," *Phys. Rev. Lett.*, vol. 115, no. 21, p. 211105, 2015, 1509.04539.

[136] P. Kanti, N. E. Mavromatos, J. Rizos, K. Tamvakis, and E. Winstanley, "Dilatonic black holes in higher curvature string gravity," *Phys. Rev. D*, vol. 54, pp. 5049–5058, 1996, hep-th/9511071.

[137] T. Torii, H. Yajima, and K.-i. Maeda, "Dilatonic black holes with Gauss-Bonnet term," *Phys. Rev. D*, vol. 55, pp. 739–753, 1997, gr-qc/9606034.

[138] K.-i. Maeda, N. Ohta, and Y. Sasagawa, "Black Hole Solutions in String Theory with Gauss-Bonnet Curvature Correction," *Phys. Rev.*, vol. D80, p. 104032, 2009, 0908.4151.

[139] M. Herrero-Valea, "The shape of scalar gauss-bonnet gravity," 2021," 2106.08344.

[140] S. D. Odintsov, V. K Oikonomou, and F. P. Fronimos, "Rectifying einstein-gauss-bonnet inflation in view of gw170817," 2020," 2003.13724.

[141] V. K. Oikonomou, “A refined einstein–gauss–bonnet inflationary theoretical framework,” *Classical and Quantum Gravity*, vol. 38, no. 19, p. 195025, Sep 2021. [Online]. Available: http://dx.doi.org/10.1088/1361-6382/ac2168

[142] D. D. Doneva and S. S. Yazadjiev, “New Gauss-Bonnet Black Holes with Curvature-Induced Scalarization in Extended Scalar-Tensor Theories,” *Phys. Rev. Lett.*, vol. 120, no. 13, p. 131103, 2018, 1711.01187.

[143] D. D. Doneva and S. S. Yazadjiev, “Neutron star solutions with curvature induced scalarization in the extended gauss-bonnet scalar-tensor theories,” *Journal of Cosmology and Astroparticle Physics*, vol. 2018, no. 04, p. 011–011, Apr 2018. [Online]. Available: http://dx.doi.org/10.1088/1475-7516/2018/04/011

[144] H. O. Silva, J. Sakstein, L. Gualtieri, T. P. Sotiriou, and E. Berti, “Spontaneous scalarization of black holes and compact stars from a Gauss-Bonnet coupling,” *Phys. Rev. Lett.*, vol. 120, no. 13, p. 131104, 2018, 1711.02080.

[145] H. O. Silva, C. F. Macedo, T. P. Sotiriou, L. Gualtieri, J. Sakstein, and E. Berti, “Stability of scalarized black hole solutions in scalar-Gauss-Bonnet gravity,” *Phys. Rev. D*, vol. 99, no. 6, p. 064011, 2019, 1812.05590.

[146] A. C. Searle, P. J. Sutton, and M. Tinto, “Bayesian detection of unmodeled bursts of gravitational waves,” *Classical and Quantum Gravity*,

vol. 26, no. 15, p. 155017, jul 2009. [Online]. Available: https://doi.org/10.1088%2F0264-9381%2F26%2F15%2F155017

[147] J. Veitch, V. Raymond, B. Farr, W. Farr, P. Graff, S. Vitale, B. Aylott, K. Blackburn, N. Christensen, M. Coughlin, W. Del Pozzo, F. Feroz, J. Gair, C.-J. Haster, V. Kalogera, T. Littenberg, I. Mandel, R. O'Shaughnessy, M. Pitkin, C. Rodriguez, C. Röver, T. Sidery, R. Smith, M. Van Der Sluys, A. Vecchio, W. Vousden, and L. Wade, "Parameter estimation for compact binaries with ground-based gravitational-wave observations using the lalinference software library," *Phys. Rev. D*, vol. 91, p. 042003, Feb 2015. [Online]. Available: https://link.aps.org/doi/10.1103/PhysRevD.91.042003

[148] D. Foreman-Mackey, D. W. Hogg, D. Lang, and J. Goodman, "emcee: The mcmc hammer," *Publications of the Astronomical Society of the Pacific*, vol. 125, no. 925, pp. 306–312, mar 2013. [Online]. Available: https://doi.org/10.1086%2F670067

[149] W. D. Vousden, W. M. Farr, and I. Mandel, "Dynamic temperature selection for parallel tempering in Markov chain Monte Carlo simulations," *Monthly Notices of the Royal Astronomical Society*, vol. 455, no. 2, pp. 1919–1937, 11 2015, https://academic.oup.com/mnras/article-pdf/455/2/1919/18514064/stv2422.pdf. [Online]. Available: https://doi.org/10.1093/mnras/stv2422

[150] J. Skilling, "Nested sampling for general Bayesian computation," *Bayesian Analysis*, vol. 1, no. 4, pp. 833 – 859, 2006. [Online]. Available: https://doi.org/10.1214/06-BA127

[151] J. S. Speagle, "dynesty: a dynamic nested sampling package for estimating bayesian posteriors and evidences," *Monthly Notices of the Royal Astronomical Society*, vol. 493, no. 3, pp. 3132–3158, feb 2020. [Online]. Available: https://doi.org/10.1093%2Fmnras%2Fstaa278

[152] D. George and E. Huerta, "Deep learning for real-time gravitational wave detection and parameter estimation: Results with advanced ligo data," *Physics Letters B*, vol. 778, pp. 64–70, 2018. [Online]. Available: https://www.sciencedirect.com/science/article/pii/S0370269317310390

[153] H. Gabbard, M. Williams, F. Hayes, and C. Messenger, "Matching matched filtering with deep networks for gravitational-wave astronomy," *Phys. Rev. Lett.*, vol. 120, p. 141103, Apr 2018. [Online]. Available: https://link.aps.org/doi/10.1103/PhysRevLett.120.141103

[154] T. Gebhard, N. Kilbertus, G. Parascandolo, I. Harry, and B. Schölkopf, "ConvWave: Searching for Gravitational Waves with Fully Convolutional Neural Nets," *Workshop on Deep Learning for Physical Sciences (DLPS 2017), NIPS 2017*, 12 2017. [Online]. Available: https://dl4physicalsciences.github.io/files/nips_dlps_2017_13.pdf

[155] M. Zevin, S. Coughlin, S. Bahaadini, E. Besler, N. Rohani, S. Allen, M. Cabero, K. Crowston, A. K. Katsaggelos, S. L. Larson, T. K. Lee, C. Lintott, T. B. Littenberg, A. Lundgren, C. Østerlund, J. R. Smith, L. Trouille, and V. Kalogera, "Gravity spy: integrating advanced ligo detector characterization, machine learning, and citizen science," *Classical and Quantum Gravity*, vol. 34, no. 6, p. 064003, feb 2017. [Online]. Available: https://dx.doi.org/10.1088/1361-6382/aa5cea

[156] P. Graff, F. Feroz, M. P. Hobson, and A. Lasenby, "BAMBI: blind accelerated multimodal bayesian inference," *Monthly Notices of the Royal Astronomical Society*, pp. no–no, jan 2012. [Online]. Available: https://doi.org/10.1111%2Fj.1365-2966.2011.20288.x

[157] A. J. Chua and M. Vallisneri, "Learning bayesian posteriors with neural networks for gravitational-wave inference," *Physical Review Letters*, vol. 124, no. 4, jan 2020. [Online]. Available: https://doi.org/10.1103%2Fphysrevlett.124.041102

[158] H. Gabbard, C. Messenger, I. S. Heng, F. Tonolini, and R. Murray-Smith, "Bayesian parameter estimation using conditional variational autoencoders for gravitational-wave astronomy," *Nature Physics*, vol. 18, no. 1, pp. 112–117, dec 2021. [Online]. Available: https://doi.org/10.1038%2Fs41567-021-01425-7

[159] H. Shen, E. A. Huerta, E. O'Shea, P. Kumar, and Z. Zhao, "Statistically-informed deep learning for gravitational wave parameter estimation," *Machine Learning: Science and Technology*, vol. 3, no. 1, p. 015007, nov 2021. [Online]. Available: https://doi.org/10.1088%2F2632-2153%2Fac3843

[160] S. R. Green, C. Simpson, and J. Gair, "Gravitational-wave parameter estimation with autoregressive neural network flows," *Physical Review D*, vol. 102, no. 10, nov 2020. [Online]. Available: https://doi.org/10.1103%2Fphysrevd.102.104057

[161] https://github.com/nj2nu/I-C_Love-C_6thorderSeriesExpansion_Coefficients.

[162] N. Jiang and K. Yagi, "Improved analytic modeling of neutron star interiors," *Phys. Rev. D*, vol. 99, p. 124029, Jun 2019. [Online]. Available: https://link.aps.org/doi/10.1103/PhysRevD.99.124029

[163] A. Maselli, V. Cardoso, V. Ferrari, L. Gualtieri, and P. Pani, "Equation-of-state-independent relations in neutron stars," *Physical Review D*, vol. 88, no. 2, jul 2013. [Online]. Available: https://doi.org/10.1103%2Fphysrevd.88.023007

[164] M. Urbanec, J. C. Miller, and Z. Stuchlí k, "Quadrupole moments of rotating neutron stars and strange stars," *Monthly Notices of the Royal Astronomical Society*, vol. 433, no. 3, pp. 1903–1909, jun 2013. [Online]. Available: https://doi.org/10.1093%2Fmnras%2Fstt858

[165] A. Nishizawa, K. Yagi, A. Taruya, and T. Tanaka, “Cosmology with space-based gravitational-wave detectors: Dark energy and primordial gravitational waves,” *Physical Review D*, vol. 85, no. 4, Feb 2012. [Online]. Available: http://dx.doi.org/10.1103/PhysRevD.85.044047

[166] A. Saffer and K. Yagi, “Tidal deformabilities of neutron stars in scalar-gauss-bonnet gravity and their applications to multimessenger tests of gravity,” *Physical Review D*, vol. 104, no. 12, Dec 2021. [Online]. Available: http://dx.doi.org/10.1103/PhysRevD.104.124052

[167] K. Yamada, T. Narikawa, and T. Tanaka, “Testing massive-field modifications of gravity via gravitational waves,” *PTEP*, vol. 2019, no. 10, p. 103E01, 2019, 1905.11859.

[168] H.-T. Wang, S.-P. Tang, P.-C. Li, M.-Z. Han, and Y.-Z. Fan, “Tight constraints on einstein-dilation-gauss-bonnet gravity from gw190412 and gw190814,” *Physical Review D*, vol. 104, no. 2, Jul 2021. [Online]. Available: http://dx.doi.org/10.1103/PhysRevD.104.024015

[169] S. Tahura and K. Yagi, “Parametrized post-einsteinian gravitational waveforms in various modified theories of gravity,” *Physical Review D*, vol. 98, no. 8, Oct 2018. [Online]. Available: http://dx.doi.org/10.1103/PhysRevD.98.084042

[170] A. Akmal, V. R. Pandharipande, and D. G. Ravenhall, “Equation of state of nucleon matter and neutron star structure,” *Phys. Rev.*

C, vol. 58, pp. 1804–1828, Sep 1998. [Online]. Available: https://link.aps.org/doi/10.1103/PhysRevC.58.1804

[171] Douchin, F. and Haensel, P., "A unified equation of state of dense matter and neutron star structure," *A&A*, vol. 380, no. 1, pp. 151–167, 2001. [Online]. Available: https://doi.org/10.1051/0004-6361:20011402

[172] R. B. Wiringa, V. Fiks, and A. Fabrocini, "Equation of state for dense nucleon matter," *Phys. Rev. C*, vol. 38, pp. 1010–1037, Aug 1988. [Online]. Available: https://link.aps.org/doi/10.1103/PhysRevC.38.1010

[173] L. Engvik, G. Bao, M. Hjorth-Jensen, E. Osnes, and E. Ostgaard, "Asymmetric nuclear matter and neutron star properties," *Astrophys. J.*, vol. 469, p. 794, 1996, nucl-th/9509016.

[174] H. Muther, M. Prakash, and T. Ainsworth, "The nuclear symmetry energy in relativistic brueckner-hartree-fock calculations," *Physics Letters B*, vol. 199, no. 4, pp. 469 – 474, 1987. [Online]. Available: http://www.sciencedirect.com/science/article/pii/037026938791611X

[175] J. M. Lattimer and F. D. Swesty, "A generalized equation of state for hot, dense matter," *Nuclear Physics A*, vol. 535, no. 2, pp. 331 – 376, 1991. [Online]. Available: http://www.sciencedirect.com/science/article/pii/037594749190452C

[176] H. Shen, H. Toki, K. Oyamatsu, and K. Sumiyoshi, “Relativistic equation of state of nuclear matter for supernova and neutron star,” *Nuclear Physics A*, vol. 637, no. 3, pp. 435 – 450, 1998. [Online]. Available: http://www.sciencedirect.com/science/article/pii/S037594749800236X

[177] H. Muller and B. D. Serot, “Relativistic mean-field theory and the high-density nuclear equation of state,” *Nuclear Physics A*, vol. 606, no. 3, pp. 508 – 537, 1996. [Online]. Available: http://www.sciencedirect.com/science/article/pii/037594749600187X

[178] K. Yagi and N. Yunes, “Approximate universal relations among tidal parameters for neutron star binaries,” *Classical and Quantum Gravity*, vol. 34, no. 1, p. 015006, 2017. [Online]. Available: http://stacks.iop.org/0264-9381/34/i=1/a=015006

[179] T. K. Chan, A. P. O. Chan, and P. T. Leung, “Universality and stationarity of the I-Love relation for self-bound stars,” *Phys. Rev.*, vol. D93, no. 2, p. 024033, 2016, 1511.08566.

[180] K. Yagi and N. Yunes, “I-Love-Q: Unexpected Universal Relations for Neutron Stars and Quark Stars,” *Science*, vol. 341, p. 365, 2013, 1302.4499.

[181] K. Yagi and N. Yunes, “I-Love-Q relations in neutron stars and their applications to astrophysics, gravitational waves, and fundamental physics,” *Phys. Rev. D* , vol. 88, no. 2, p. 023009, Jul. 2013, 1303.1528.

[182] K. Yagi and N. Yunes, “Approximate Universal Relations for Neutron Stars and Quark Stars,” *Phys. Rept.*, vol. 681, pp. 1–72, 2017, 1608.02582.

[183] J. B. Hartle, “Slowly Rotating Relativistic Stars. I. Equations of Structure,” *Astrophys. J.* , vol. 150, p. 1005, Dec 1967.

[184] C. Breu and L. Rezzolla, “Maximum mass, moment of inertia and compactness of relativistic stars,” *Mon. Not. Roy. Astron. Soc.*, vol. 459, no. 1, pp. 646–656, 2016, 1601.06083.

[185] K. V. Staykov, D. D. Doneva, and S. S. Yazadjiev, “Moment-of-inertia–compactness universal relations in scalar-tensor theories and $\mathcal{R}^2$ gravity,” *Phys. Rev.*, vol. D93, no. 8, p. 084010, 2016, 1602.00504.

[186] T. Damour and A. Nagar, “Relativistic tidal properties of neutron stars,” *Phys. Rev.*, vol. D80, p. 084035, 2009, 0906.0096.

[187] K. Boshkayev, H. Quevedo, and B. Zhami, “I -Love- Q relations for white dwarf stars,” *Mon. Not. Roy. Astron. Soc.*, vol. 464, pp. 4349–4359, Feb. 2017.

[188] K. Boshkayev and H. Quevedo, “Non-validity of I-Love-Q Relations for Hot White Dwarf Stars,” *Mon. Not. Roy. Astron. Soc.*, vol. 478, pp. 1893–1899, Aug. 2018, 1709.04593.

[189] A. Taylor, K. Yagi, and P. Arras, “I-Love-Q Relations for Realistic White Dwarfs,” *Mon. Not. Roy. Astron. Soc.*, vol. 492, no. 1, pp. 978–992, 2020, 1912.09557.

[190] D. Petroff, “Slowly rotating homogeneous stars and the Heun equation,” *Class. Quant. Grav.*, vol. 24, pp. 1055–1068, 2007, gr-qc/0701081.

[191] L. C. Stein, K. Yagi, and N. Yunes, “Three-Hair Relations for Rotating Stars: Nonrelativistic Limit,” *Astrophys. J.*, vol. 788, p. 15, 2014, 1312.4532.

[192] K. Yagi, K. Kyutoku, G. Pappas, N. Yunes, and T. A. Apostolatos, “Effective No-Hair Relations for Neutron Stars and Quark Stars: Relativistic Results,” *Phys. Rev.*, vol. D89, no. 12, p. 124013, 2014, 1403.6243.

[193] B. Majumder, K. Yagi, and N. Yunes, “Improved Universality in the Neutron Star Three-Hair Relations,” *Phys. Rev.*, vol. D92, no. 2, p. 024020, 2015, 1504.02506.

[194] K. Yagi, “Multipole Love Relations,” *Phys. Rev.*, vol. D89, no. 4, p. 043011, 2014, 1311.0872, [Erratum: Phys. Rev.D96,no.12,129904(2017); Erratum: Phys. Rev.D97,no.12,129901(2018)].

[195] C. Messenger and J. Read, “Measuring a cosmological distance-redshift relationship using only gravitational wave observations of binary neutron star coalescences,” *Physical Review Letters*, vol. 108, no. 9, Feb 2012. [Online]. Available: http://dx.doi.org/10.1103/PhysRevLett.108.091101

[196] A. Sesana, “Prospects for Multiband Gravitational-Wave Astronomy after GW150914,” *Phys. Rev. Lett.*, vol. 116, no. 23, p. 231102, 2016, 1602.06951.

[197] E. Barausse, N. Yunes, and K. Chamberlain, “Theory-Agnostic Constraints on Black-Hole Dipole Radiation with Multiband Gravitational-Wave Astrophysics,” *Phys. Rev. Lett.*, vol. 116, no. 24, p. 241104, 2016, 1603.04075.

[198] S. Isoyama, H. Nakano, and T. Nakamura, “Multiband gravitational-wave astronomy: Observing binary inspirals with a decihertz detector, b-decigo,” *Progress of Theoretical and Experimental Physics*, vol. 2018, no. 7, Jul 2018. [Online]. Available: http://dx.doi.org/10.1093/ptep/pty078

[199] Z. Carson and K. Yagi, “Multi-band gravitational wave tests of general relativity,” *Class. Quant. Grav.*, vol. 37, no. 2, p. 02LT01, 2020, 1905.13155.

[200] C. Cutler *et al.*, “What we can learn from multi-band observations of black hole binaries,” *arXiv*, 2019, 1903.04069.

[201] Z. Carson and K. Yagi, “Parametrized and inspiral-merger-ringdown consistency tests of gravity with multiband gravitational wave observations,” *Phys. Rev.*, vol. D101, no. 4, p. 044047, 2020, 1911.05258.

[202] A. Gupta, S. Datta, S. Kastha, S. Borhanian, K. G. Arun, and B. S. Sathyaprakash, “Multiparameter tests of general relativity using multiband gravitational-wave observations,” *Phys. Rev. Lett.*, vol. 125, no. 20, p. 201101, 2020, 2005.09607.

[203] S. Datta, A. Gupta, S. Kastha, K. G. Arun, and B. S. Sathyaprakash, "Tests of general relativity using multiband observations of intermediate mass binary black hole mergers," *Phys. Rev.*, vol. D103, no. 2, p. 024036, 2021, 2006.12137.

[204] S. Kawamura *et al.*, "The japanese space gravitational wave antenna - DECIGO," *Journal of Physics: Conference Series*, vol. 122, p. 012006, jul 2008. [Online]. Available: https://doi.org/10.1088/1742-6596/122/1/012006

[205] S. Kawamura *et al.*, "Current status of space gravitational wave antenna decigo and b-decigo," 2020," 2006.13545.

[206] B. F. Schutz, "Determining the Hubble Constant from Gravitational Wave Observations," *Nature*, vol. 323, pp. 310–311, 1986.

[207] B. P. Abbott *et al.*, "A gravitational-wave standard siren measurement of the Hubble constant," *Nature*, vol. 551, no. 7678, pp. 85–88, 2017, 1710.05835.

[208] M. Fishbach *et al.*, "A Standard Siren Measurement of the Hubble Constant from GW170817 without the Electromagnetic Counterpart," *Astrophys. J. Lett.*, vol. 871, no. 1, p. L13, 2019, 1807.05667.

[209] I. D. Saltas, I. Sawicki, L. Amendola, and M. Kunz, "Anisotropic Stress as a Signature of Nonstandard Propagation of Gravitational Waves," *Phys. Rev. Lett.*, vol. 113, no. 19, p. 191101, 2014, 1406.7139.

[210] A. Nishizawa, "Generalized framework for testing gravity with gravitational-wave propagation. I. Formulation," *Phys. Rev.*, vol. D97, no. 10, p. 104037, 2018, 1710.04825.

[211] S. Mastrogiovanni, D. A. Steer, and M. Barsuglia, "Probing modified gravity theories and cosmology using gravitational-waves and associated electromagnetic counterparts," *Phys. Rev. D*, vol. 102, p. 044009, Aug 2020. [Online]. Available: https://link.aps.org/doi/10.1103/PhysRevD.102.044009

[212] G. W. Horndeski, "Second-order scalar-tensor field equations in a four-dimensional space," *Int. J. Theor. Phys.*, vol. 10, pp. 363–384, 1974.

[213] T. Kobayashi, "Horndeski theory and beyond: a review," *Rept. Prog. Phys.*, vol. 82, no. 8, p. 086901, 2019, 1901.07183.

[214] B. P. Abbott *et al.*, "GW170817: Observation of Gravitational Waves from a Binary Neutron Star Inspiral," *Phys. Rev. Lett.*, vol. 119, no. 16, p. 161101, 2017, 1710.05832.

[215] D. Bettoni, J. M. Ezquiaga, K. Hinterbichler, and M. Zumalacárregui, "Speed of Gravitational Waves and the Fate of Scalar-Tensor Gravity," *Phys. Rev.*, vol. D95, no. 8, p. 084029, 2017, 1608.01982.

[216] R. Kimura and K. Yamamoto, "Constraints on general second-order scalar-tensor models from gravitational Cherenkov radiation," *JCAP*, vol. 1207, p. 050, 2012, 1112.4284.

[217] R. McManus, L. Lombriser, and J. Peñarrubia, “Finding Horndeski theories with Einstein gravity limits,” *JCAP*, vol. 1611, p. 006, 2016, 1606.03282.

[218] C. Brans and R. H. Dicke, “Mach’s principle and a relativistic theory of gravitation,” *Phys. Rev.*, vol. 124, pp. 925–935, Nov 1961. [Online]. Available: https://link.aps.org/doi/10.1103/PhysRev.124.925

[219] W. Hu and I. Sawicki, “Models of $f(r)$ cosmic acceleration that evade solar system tests,” *Phys. Rev. D*, vol. 76, p. 064004, Sep 2007. [Online]. Available: https://link.aps.org/doi/10.1103/PhysRevD.76.064004

[220] Y.-S. Song, W. Hu, and I. Sawicki, “Large scale structure off(r)gravity,” *Physical Review D*, vol. 75, no. 4, Feb 2007. [Online]. Available: http://dx.doi.org/10.1103/PhysRevD.75.044004

[221] E. Bellini and I. Sawicki, “Maximal freedom at minimum cost: linear large-scale structure in general modifications of gravity,” *Journal of Cosmology and Astroparticle Physics*, vol. 2014, no. 07, p. 050–050, Jul 2014. [Online]. Available: http://dx.doi.org/10.1088/1475-7516/2014/07/050

[222] F. Simpson, C. Heymans, D. Parkinson, C. Blake, M. Kilbinger, J. Benjamin, T. Erben, H. Hildebrandt, H. Hoekstra, T. D. Kitching, and et al., “Cfhtlens: testing the laws of gravity with tomographic weak lensing and redshift-space distortions,” *Monthly Notices of the Royal Astronomical*

Society, vol. 429, no. 3, p. 2249–2263, Dec 2012. [Online]. Available: http://dx.doi.org/10.1093/mnras/sts493

[223] L. Lombriser and A. Taylor, "Breaking a dark degeneracy with gravitational waves," *Journal of Cosmology and Astroparticle Physics*, vol. 2016, no. 03, pp. 031–031, mar 2016. [Online]. Available: https://doi.org/10.1088%2F1475-7516%2F2016%2F03%2F031

[224] B. Wang, Z. Zhu, A. Li, and W. Zhao, "Comprehensive analysis of the tidal effect in gravitational waves and implication for cosmology," *The Astrophysical Journal Supplement Series*, vol. 250, no. 1, p. 6, Aug 2020. [Online]. Available: http://dx.doi.org/10.3847/1538-4365/aba2f3

[225] T. Dietrich, A. Samajdar, S. Khan, N. K. Johnson-McDaniel, R. Dudi, and W. Tichy, "Improving the nrtidal model for binary neutron star systems," *Physical Review D*, vol. 100, no. 4, Aug 2019. [Online]. Available: http://dx.doi.org/10.1103/PhysRevD.100.044003

[226] T. Dietrich, S. Bernuzzi, and W. Tichy, "Closed-form tidal approximants for binary neutron star gravitational waveforms constructed from high-resolution numerical relativity simulations," *Phys. Rev. D*, vol. 96, p. 121501, Dec 2017. [Online]. Available: https://link.aps.org/doi/10.1103/PhysRevD.96.121501

[227] C. Cutler and E. E. Flanagan, "Gravitational waves from merging compact binaries: How accurately can one extract the binary's parameters from the

inspiral wave form?" *Phys. Rev.*, vol. D49, pp. 2658–2697, 1994, gr-qc/9402014.

[228] S. Husa, S. Khan, M. Hannam, M. Pürrer, F. Ohme, X. J. Forteza, and A. Bohé, "Frequency-domain gravitational waves from nonprecessing black-hole binaries. i. new numerical waveforms and anatomy of the signal," *Phys. Rev. D*, vol. 93, p. 044006, Feb 2016. [Online]. Available: https://link.aps.org/doi/10.1103/PhysRevD.93.044006

[229] S. Khan, S. Husa, M. Hannam, F. Ohme, M. Pürrer, X. J. Forteza, and A. Bohé, "Frequency-domain gravitational waves from nonprecessing black-hole binaries. ii. a phenomenological model for the advanced detector era," *Phys. Rev. D*, vol. 93, p. 044007, Feb 2016. [Online]. Available: https://link.aps.org/doi/10.1103/PhysRevD.93.044007

[230] S. Hild *et al.*, "Sensitivity studies for third-generation gravitational wave observatories," *Classical and Quantum Gravity*, vol. 28, no. 9, p. 094013, apr 2011. [Online]. Available: https://doi.org/10.1088/0264-9381/28/9/094013

[231] E. Berti, A. Buonanno, and C. M. Will, "Estimating spinning binary parameters and testing alternative theories of gravity with lisa," *Physical Review D*, vol. 71, no. 8, Apr 2005. [Online]. Available: http://dx.doi.org/10.1103/PhysRevD.71.084025

[232] Douchin, F. and Haensel, P., "A unified equation of state of dense matter and neutron star structure," *A&A*, vol. 380, no. 1, pp. 151–167, 2001. [Online].

Available: https://doi.org/10.1051/0004-6361:20011402

[233] H. Müther, M. Prakash, and T. Ainsworth, "The nuclear symmetry energy in relativistic brueckner-hartree-fock calculations," *Physics Letters B*, vol. 199, no. 4, pp. 469 – 474, 1987. [Online]. Available: http://www.sciencedirect.com/science/article/pii/037026938791611X

[234] H. Müller and B. D. Serot, "Relativistic mean-field theory and the high-density nuclear equation of state," *Nuclear Physics A*, vol. 606, no. 3, pp. 508 – 537, 1996. [Online]. Available: http://www.sciencedirect.com/science/article/pii/037594749600187X

[235] M. CHEVALLIER and D. POLARSKI, "Accelerating universes with scaling dark matter," *International Journal of Modern Physics D*, vol. 10, no. 02, pp. 213–223, 2001, https://doi.org/10.1142/S0218271801000822. [Online]. Available: https://doi.org/10.1142/S0218271801000822

[236] E. V. Linder, "Exploring the expansion history of the universe," *Phys. Rev. Lett.*, vol. 90, p. 091301, Mar 2003. [Online]. Available: https://link.aps.org/doi/10.1103/PhysRevLett.90.091301

[237] B. S. Sathyaprakash, B. F. Schutz, and C. Van Den Broeck, "Cosmography with the einstein telescope," *Classical and Quantum Gravity*, vol. 27, no. 21, p. 215006, Sep 2010. [Online]. Available: http://dx.doi.org/10.1088/0264-9381/27/21/215006

[238] K. W. Wong, E. D. Kovetz, C. Cutler, and E. Berti, "Expanding the lisa horizon from the ground," *Physical Review Letters*, vol. 121, no. 25, Dec 2018. [Online]. Available: http://dx.doi.org/10.1103/PhysRevLett.121.251102

[239] C. Cutler and J. Harms, "Big bang observer and the neutron-star-binary subtraction problem," *Physical Review D*, vol. 73, no. 4, Feb 2006. [Online]. Available: http://dx.doi.org/10.1103/PhysRevD.73.042001

[240] B. P. Abbott *et al.*, "Gwtc-1: A gravitational-wave transient catalog of compact binary mergers observed by ligo and virgo during the first and second observing runs," *Phys. Rev. X*, vol. 9, p. 031040, Sep 2019. [Online]. Available: https://link.aps.org/doi/10.1103/PhysRevX.9.031040

[241] K. Yagi and N. Yunes, "Binary Love Relations," *Class. Quant. Grav.*, vol. 33, no. 13, p. 13LT01, 2016, 1512.02639.

[242] K. Chatziioannou, C.-J. Haster, and A. Zimmerman, "Measuring the neutron star tidal deformability with equation-of-state-independent relations and gravitational waves," *Phys. Rev.*, vol. D97, no. 10, p. 104036, 2018, 1804.03221.

[243] W. Del Pozzo, "Inference of the cosmological parameters from gravitational waves: application to second generation interferometers," *Phys. Rev.*, vol. D86, p. 043011, 2012, 1108.1317.

[244] B. P. Abbott *et al.*, "A gravitational-wave measurement of the Hubble constant following the second observing run of Advanced LIGO and Virgo," *The Astrophysical Journal*, 2019, 1908.06060.

[245] S. R. Taylor, J. R. Gair, and I. Mandel, "Hubble without the Hubble: Cosmology using advanced gravitational-wave detectors alone," *Phys. Rev.*, vol. D85, p. 023535, 2012, 1108.5161.

[246] S. R. Taylor and J. R. Gair, "Cosmology with the lights off: standard sirens in the Einstein Telescope era," *Phys. Rev.*, vol. D86, p. 023502, 2012, 1204.6739.

[247] Z. Carson, B. C. Seymour, and K. Yagi, "Future prospects for probing scalar–tensor theories with gravitational waves from mixed binaries," *Classical and Quantum Gravity*, vol. 37, no. 6, p. 065008, Feb 2020. [Online]. Available: http://dx.doi.org/10.1088/1361-6382/ab6a1f

[248] R. Abbott, T. D. Abbott, S. Abraham, F. Acernese, K. Ackley, A. Adams, C. Adams, R. X. Adhikari, V. B. Adya, C. Affeldt, and et al., "Observation of gravitational waves from two neutron star–black hole coalescences," *The Astrophysical Journal Letters*, vol. 915, no. 1, p. L5, Jun 2021. [Online]. Available: http://dx.doi.org/10.3847/2041-8213/ac082e

[249] G. Pratten *et al.*, "Computationally efficient models for the dominant and subdominant harmonic modes of precessing binary black holes," *Phys. Rev. D*, vol. 103, no. 10, p. 104056, 2021, 2004.06503.

[250] G. Pratten, S. Husa, C. Garcia-Quiros, M. Colleoni, A. Ramos-Buades, H. Estelles, and R. Jaume, "Setting the cornerstone for a family of models for gravitational waves from compact binaries: The dominant harmonic for nonprecessing quasicircular black holes," *Phys. Rev. D*, vol. 102, no. 6, p. 064001, 2020, 2001.11412.

[251] C. García-Quirós, M. Colleoni, S. Husa, H. Estellés, G. Pratten, A. Ramos-Buades, M. Mateu-Lucena, and R. Jaume, "Multimode frequency-domain model for the gravitational wave signal from nonprecessing black-hole binaries," *Phys. Rev. D*, vol. 102, no. 6, p. 064002, 2020, 2001.10914.

[252] B. Abbott, R. Abbott, T. Abbott, S. Abraham, F. Acernese, K. Ackley, C. Adams, R. Adhikari, V. Adya, C. Affeldt, and et al., "Tests of general relativity with the binary black hole signals from the ligo-virgo catalog gwtc-1," *Physical Review D*, vol. 100, no. 10, Nov 2019. [Online]. Available: http://dx.doi.org/10.1103/PhysRevD.100.104036

[253] B. Shiralilou, T. Hinderer, S. Nissanke, N. Ortiz, and H. Witek, "Post-newtonian gravitational and scalar waves in scalar-gauss-bonnet gravity," 2021," 2105.13972.

[254] S. E. Perkins, R. Nair, H. O. Silva, and N. Yunes, "Improved gravitational-wave constraints on higher-order curvature theories of gravity,"

Physical Review D, vol. 104, no. 2, Jul 2021. [Online]. Available: http://dx.doi.org/10.1103/PhysRevD.104.024060

[255] N. Sennett, S. Marsat, and A. Buonanno, "Gravitational waveforms in scalar-tensor gravity at 2pn relative order," *Physical Review D*, vol. 94, no. 8, Oct 2016. [Online]. Available: http://dx.doi.org/10.1103/PhysRevD.94.084003

[256] W. E. East and J. L. Ripley, "Dynamics of spontaneous black hole scalarization and mergers in einstein-scalar-gauss-bonnet gravity," *Physical Review Letters*, vol. 127, no. 10, Sep 2021. [Online]. Available: http://dx.doi.org/10.1103/PhysRevLett.127.101102

[257] W. E. East and J. L. Ripley, "Evolution of einstein-scalar-gauss-bonnet gravity using a modified harmonic formulation," *Physical Review D*, vol. 103, no. 4, Feb 2021. [Online]. Available: http://dx.doi.org/10.1103/PhysRevD.103.044040

[258] E. Berti, K. Yagi, and N. Yunes, "Extreme Gravity Tests with Gravitational Waves from Compact Binary Coalescences: (I) Inspiral-Merger," *Gen. Rel. Grav.*, vol. 50, no. 4, p. 46, 2018, 1801.03208.

[259] M. Okounkova, "Numerical relativity simulation of GW150914 in Einstein dilaton Gauss-Bonnet gravity," *Phys. Rev. D*, vol. 102, no. 8, p. 084046, 2020, 2001.03571.

[260] H. Zhang, M. Zhou, C. Bambi, B. Kleihaus, J. Kunz, and E. Radu, "Testing einstein-dilaton-gauss-bonnet gravity with the reflection spectrum of accreting

black holes," *Physical Review D*, vol. 95, no. 10, May 2017. [Online]. Available: http://dx.doi.org/10.1103/PhysRevD.95.104043

[261] L. Amendola, C. Charmousis, and S. C. Davis, "Solar system constraints on gauss–bonnet mediated dark energy," *Journal of Cosmology and Astroparticle Physics*, vol. 2007, no. 10, p. 004–004, Oct 2007. [Online]. Available: http://dx.doi.org/10.1088/1475-7516/2007/10/004

[262] C. Cutler and E. E. Flanagan, "Gravitational waves from merging compact binaries: How accurately can one extract the binary's parameters from the inspiral waveform?" *Phys. Rev. D*, vol. 49, pp. 2658–2697, Mar 1994. [Online]. Available: https://link.aps.org/doi/10.1103/PhysRevD.49.2658

[263] A. Buonanno, B. R. Iyer, E. Ochsner, Y. Pan, and B. S. Sathyaprakash, "Comparison of post-newtonian templates for compact binary inspiral signals in gravitational-wave detectors," *Physical Review D*, vol. 80, no. 8, Oct 2009. [Online]. Available: http://dx.doi.org/10.1103/PhysRevD.80.084043

[264] R. Abbott, T. Abbott, S. Abraham, F. Acernese, K. Ackley, A. Adams, C. Adams, R. Adhikari, V. Adya, C. Affeldt, and et al., "Gwtc-2: Compact binary coalescences observed by ligo and virgo during the first half of the third observing run," *Physical Review X*, vol. 11, no. 2, Jun 2021. [Online]. Available: http://dx.doi.org/10.1103/PhysRevX.11.021053

[265] R. Abbott, T. D. Abbott, S. Abraham, F. Acernese, K. Ackley, C. Adams, R. X. Adhikari, V. B. Adya, C. Affeldt, M. Agathos, and et al., "Gw190814: Gravitational waves from the coalescence of a 23 solar mass black hole with a 2.6 solar mass compact object," *The Astrophysical Journal*, vol. 896, no. 2, p. L44, Jun 2020. [Online]. Available: http://dx.doi.org/10.3847/2041-8213/ab960f

[266] I. Tews, P. T. H. Pang, T. Dietrich, M. W. Coughlin, S. Antier, M. Bulla, J. Heinzel, and L. Issa, "On the nature of gw190814 and its impact on the understanding of supranuclear matter," *The Astrophysical Journal*, vol. 908, no. 1, p. L1, Feb 2021. [Online]. Available: http://dx.doi.org/10.3847/2041-8213/abdaae

[267] D.-S. Shao, S.-P. Tang, J.-L. Jiang, and Y.-Z. Fan, "Maximum mass cutoff in the neutron star mass distribution and the prospect of forming supramassive objects in the double neutron star mergers," *Physical Review D*, vol. 102, no. 6, Sep 2020. [Online]. Available: http://dx.doi.org/10.1103/PhysRevD.102.063006

[268] A. Nathanail, E. R. Most, and L. Rezzolla, "Gw170817 and gw190814: Tension on the maximum mass," *The Astrophysical Journal Letters*, vol. 908, no. 2, p. L28, Feb 2021. [Online]. Available: http://dx.doi.org/10.3847/2041-8213/abdfc6

[269] E. Thrane and C. Talbot, "An introduction to bayesian inference in gravitational-wave astronomy: Parameter estimation, model selection, and

hierarchical models," *Publications of the Astronomical Society of Australia*, vol. 36, 2019. [Online]. Available: http://dx.doi.org/10.1017/pasa.2019.2

[270] R. Smith, S. Borhanian, B. Sathyaprakash, F. Hernandez Vivanco, S. E. Field, P. Lasky, I. Mandel, S. Morisaki, D. Ottaway, B. J. Slagmolen, and et al., "Bayesian inference for gravitational waves from binary neutron star mergers in third generation observatories," *Physical Review Letters*, vol. 127, no. 8, Aug 2021. [Online]. Available: http://dx.doi.org/10.1103/PhysRevLett.127.081102

[271] R. Abbott, T. D. Abbott, S. Abraham, F. Acernese, K. Ackley, C. Adams, R. X. Adhikari, V. B. Adya, C. Affeldt, M. Agathos, and et al., "Open data from the first and second observing runs of advanced ligo and advanced virgo," *SoftwareX*, vol. 13, p. 100658, Jan 2021. [Online]. Available: http://dx.doi.org/10.1016/j.softx.2021.100658

[272] A. Nitz, I. Harry, D. Brown, C. M. Biwer, J. Willis, T. D. Canton, C. Capano, T. Dent, L. Pekowsky, A. R. Williamson, G. S. C. Davies, S. De, M. Cabero, B. Machenschalk, P. Kumar, D. Macleod, S. Reyes, dfinstad, F. Pannarale, T. Massinger, S. Kumar, M. Tápai, L. Singer, S. Khan, S. Fairhurst, A. Nielsen, S. Singh, shasvath, B. U. V. Gadre, and I. Dorrington, "gwastro/pycbc: Pycbc release 1.18.1," May 2021. [Online]. Available: https://doi.org/10.5281/zenodo.4849433

[273] C. M. Biwer, C. D. Capano, S. De, M. Cabero, D. A. Brown, A. H. Nitz, and V. Raymond, "Pycbc inference: A python-based parameter estimation toolkit for compact binary coalescence signals," *Publications of the Astronomical Society of the Pacific*, vol. 131, no. 996, p. 024503, Jan 2019. [Online]. Available: http://dx.doi.org/10.1088/1538-3873/aaef0b

[274] D. Foreman-Mackey, D. W. Hogg, D. Lang, and J. Goodman, "emcee: The mcmc hammer," *PASP*, vol. 125, pp. 306–312, 2013, 1202.3665.

[275] LIGO Scientific Collaboration, "LIGO Algorithm Library - LALSuite," free software (GPL), 2018.

[276] L. S. Finn, "Detection, measurement, and gravitational radiation," *Physical Review D*, vol. 46, no. 12, p. 5236–5249, Dec 1992. [Online]. Available: http://dx.doi.org/10.1103/PhysRevD.46.5236

[277] C. Cutler, "Angular resolution of the lisa gravitational wave detector," *Physical Review D*, vol. 57, no. 12, p. 7089–7102, Jun 1998. [Online]. Available: http://dx.doi.org/10.1103/PhysRevD.57.7089

[278] M. Vallisneri, "Use and abuse of the fisher information matrix in the assessment of gravitational-wave parameter-estimation prospects," *Physical Review D*, vol. 77, no. 4, Feb 2008. [Online]. Available: http://dx.doi.org/10.1103/PhysRevD.77.042001

[279] E. Berti, A. Buonanno, and C. M. Will, “Estimating spinning binary parameters and testing alternative theories of gravity with LISA,” *Phys. Rev. D*, vol. 71, p. 084025, 2005, gr-qc/0411129.

[280] S. Perkins and N. Yunes, “Are parametrized tests of general relativity with gravitational waves robust to unknown higher post-newtonian order effects?” 2022” 2201.02542.

[281] S. Alexander and N. Yunes, “Chern-Simons Modified General Relativity,” *Phys. Rept.*, vol. 480, pp. 1–55, 2009, 0907.2562.

[282] K. Yagi, N. Yunes, and T. Tanaka, “Gravitational Waves from Quasi-Circular Black Hole Binaries in Dynamical Chern-Simons Gravity,” *Phys. Rev. Lett.*, vol. 109, p. 251105, 2012, 1208.5102, [Erratum: Phys.Rev.Lett. 116, 169902 (2016), Erratum: Phys.Rev.Lett. 124, 029901 (2020)].

[283] D. P. Kingma and M. Welling, “Auto-encoding variational bayes,” 2022,” 1312.6114.

[284] D. J. Rezende, S. Mohamed, and D. Wierstra, “Stochastic backpropagation and approximate inference in deep generative models,” 2014,” 1401.4082.

[285] A. Nguyen, J. Clune, Y. Bengio, A. Dosovitskiy, and J. Yosinski, “Plug and play generative networks: Conditional iterative generation of images in latent space,” 2017,” 1612.00005.

[286] F. Tonolini, J. Radford, A. Turpin, D. Faccio, and R. Murray-Smith, "Variational inference for computational imaging inverse problems," 2020," 1904.06264.

[287] J. Walker, C. Doersch, A. Gupta, and M. Hebert, "An uncertain future: Forecasting from static images using variational autoencoders," 2016," 1606.07873.

[288] K. Sohn, H. Lee, and X. Yan, "Learning structured output representation using deep conditional generative models," in *Advances in Neural Information Processing Systems*, C. Cortes, N. Lawrence, D. Lee, M. Sugiyama, and R. Garnett, Eds., vol. 28. Curran Associates, Inc., 2015. [Online]. Available: https://proceedings.neurips.cc/paper_files/paper/2015/file/8d55a249e6baa5c06772297520da2051-Paper.pdf

[289] S. Khan, K. Chatziioannou, M. Hannam, and F. Ohme, "Phenomenological model for the gravitational-wave signal from precessing binary black holes with two-spin effects," *Physical Review D*, vol. 100, no. 2, jul 2019. [Online]. Available: https://doi.org/10.1103%2Fphysrevd.100.024059

[290] G. Ashton, M. Hübner, P. D. Lasky, C. Talbot, K. Ackley, S. Biscoveanu, Q. Chu, A. Divakarla, P. J. Easter, B. Goncharov, F. H. Vivanco, J. Harms, M. E. Lower, G. D. Meadors, D. Melchor, E. Payne, M. D. Pitkin, J. Powell, N. Sarin, R. J. E. Smith, and E. Thrane, "Bilby: A user-friendly bayesian inference library for gravitational-wave astronomy," *The Astrophysical Journal*

Supplement Series, vol. 241, no. 2, p. 27, apr 2019. [Online]. Available: https://dx.doi.org/10.3847/1538-4365/ab06fc

[291] D. J. Rezende and S. Mohamed, “Variational inference with normalizing flows,” 2016,” 1505.05770.

[292] D. P. Kingma, T. Salimans, R. Jozefowicz, X. Chen, I. Sutskever, and M. Welling, “Improving variational inference with inverse autoregressive flow,” 2017,” 1606.04934.

[293] G. Papamakarios, T. Pavlakou, and I. Murray, “Masked autoregressive flow for density estimation,” 2018,” 1705.07057.

[294] E. Poisson and C. M. Will, “Gravitational waves from inspiraling compact binaries: Parameter estimation using second-post-newtonian waveforms,” *Phys. Rev. D*, vol. 52, pp. 848–855, Jul 1995. [Online]. Available: https://link.aps.org/doi/10.1103/PhysRevD.52.848

[295] C. Cutler, “Angular resolution of the LISA gravitational wave detector,” *Phys. Rev.*, vol. D57, pp. 7089–7102, 1998, gr-qc/9703068.

[296] K. Yagi and T. Tanaka, “Constraining alternative theories of gravity by gravitational waves from precessing eccentric compact binaries with LISA,” *Phys. Rev.*, vol. D81, p. 064008, 2010, 0906.4269, [Erratum: Phys. Rev.D81,109902(2010)].

[297] K. Yagi and T. Tanaka, "DECIGO/BBO as a probe to constrain alternative theories of gravity," *Prog. Theor. Phys.*, vol. 123, pp. 1069–1078, 2010, 0908.3283.

[298] F.-L. Julié and E. Berti, "Post-Newtonian dynamics and black hole thermodynamics in Einstein-scalar-Gauss-Bonnet gravity," *Phys. Rev. D*, vol. 100, no. 10, p. 104061, 2019, 1909.05258.

[299] L. Bernard, L. Blanchet, and D. Trestini, "Gravitational waves in scalar-tensor theory to one-and-a-half post-newtonian order," *Journal of Cosmology and Astroparticle Physics*, vol. 2022, no. 08, p. 008, aug 2022. [Online]. Available: https://doi.org/10.1088%2F1475-7516%2F2022%2F08%2F008

[300] N. Yunes and F. Pretorius, "Fundamental theoretical bias in gravitational wave astrophysics and the parametrized post-einsteinian framework," *Physical Review D*, vol. 80, no. 12, Dec 2009. [Online]. Available: http://dx.doi.org/10.1103/PhysRevD.80.122003

[301] K. Chatziioannou, N. Yunes, and N. Cornish, "Model-independent test of general relativity: An extended post-einsteinian framework with complete polarization content," *Physical Review D*, vol. 86, no. 2, Jul 2012. [Online]. Available: http://dx.doi.org/10.1103/PhysRevD.86.022004